SOURCE CHARACTERIZATION AND GRAVITY DATA MODELING OF DELHI FOLD BELT, INDIA

A THESIS

Submitted in partial fulfilment of the
requirements for the award of the degree

of

DOCTOR OF PHILOSOPHY

in

EARTH SCIENCES

by

DIVYANSHU DWIVEDI

DEPARTMENT OF EARTH SCIENCES
INDIAN INSTITUTE OF TECHNOLOGY ROORKEE
ROORKEE - 247 667 (INDIA)
MAY, 2019

SOURCE CHARACTERIZATION AND GRAVITY DATA MODELING OF DELHI FOLD BELT, INDIA

Ph. D. THESIS

by

DIVYANSHU DWIVEDI

DEPARTMENT OF EARTH SCIENCES
INDIAN INSTITUTE OF TECHNOLOGY ROORKEE
ROORKEE - 247 667 (INDIA)
MAY, 2019


भारतीय प्रौद्योगिकी संस्थान रुड़की
INDIAN INSTITUTE OF TECHNOLOGY ROORKEE

INDIAN INSTITUTE OF TECHNOLOGY ROORKEE ROORKEE

CANDIDATE'S DECLARATION

I hereby certify that the work which is being presented in the thesis entitled **"SOURCE CHARACTERIZATION AND GRAVITY DATA MODELING OF DELHI FOLD BELT, INDIA"** in partial fulfilment of the requirements for the award of the Degree of Doctor of Philosophy and submitted in the Department of Earth Sciences of the Indian Institute of Technology Roorkee, Roorkee is an authentic record of my own work carried out during a period from July, 2014 to May, 2019 under the supervision of Dr. Ashutosh Chamoli, Assistant Professor, Department of Earth Sciences, Indian Institute of Technology Roorkee, Roorkee.

The matter presented in this thesis has not been submitted by me for the award of any other degree of this or any other Institution.

(DIVYANSHU DWIVEDI)

This is to certify that the above statement made by the candidate is correct to the best of my knowledge.

(Ashutosh Chamoli)
Supervisor

The Ph.D. Viva-Voce Examination of Divyanshu Dwivedi, Research Scholar, has been held on August 5, 2019.

Chairman, SRC **External Examiner**

This is to certify that the student has made all corrections in the thesis.

(Ashutosh Chamoli)
Supervisor
Dated: August 5, 2019

Head of the Department

DEDICATED TO
"MY BELOVED PARENTS"

ABSTRACT

The Delhi fold belt (DFB) represents the Proterozoic Aravalli-Delhi orogeny, which lies as a prominent NE-SW trending transverse structural heterogeneity at the leading edge of the Indian peninsula. Precambrian orogenic belts help in understanding the evolution of continents and play an important role to study the tectonic history of the cratonic regions. These behave as structural heterogeneities on the underthrusting Indian plate and likely control the earthquake ruptures of the Himalayan front.

The Proterozoic DFB in NW India shows a prominent NNE-SSW (~ 600 km) trending gravity high. Past studies are mainly carried out along the Nagaur-Jhalawar transect towards the south (~ 150 km) from the profile BB' of the study region. There is the abrupt absence of the Moho signature below the DFB in the seismic sections, which is although present below surrounding geological formations. Further, there is no detailed geophysical investigation addressing the DFB structure towards the north (beneath Delhi, Rajasthan and Haryana states). The interpretations in these studies are qualitative, and researchers have pointed lack of understanding in the crustal configuration of the DFB due to speculative results.

In view of scanty geophysical studies, I have carried out a detailed analysis of gravity dataset of the region to understand the crustal structure below the DFB. The study addresses whether the structures modeled in the southern region of the DFB along the Nagaur-Jhalawar transect in past studies are extending towards the north in the study region. The Bouguer gravity anomaly of the study region is modeled using radially averaged power spectrum, wavelength filtering, 3D structural inversion, wavelet source edge detector (WSED) method and depth from extreme points (DEXP) method to constrain the crustal structure of the DFB.

The radially averaged power spectrum of the Bouguer gravity anomaly is used to derive a priori model for an average depths of the layered interfaces, which are further used in modeling. The Bouguer gravity anomalies are separated based on the characteristics of the power spectrum to understand the deep and shallow structures. The 3D structural inversion is performed on the long-wavelength filtered gravity anomaly to derive the 3D lateral variations of the Moho interface. The derived Moho geometry is helpful in imaging the 2D density modeling. I have developed and propose a new methodology named WSED, which is efficient in deriving the source edge boundaries using gravity or magnetic data. The method uses wavelet theory to identify the directional properties of the edges. The method is found

advantageous in comparison to conventional techniques. The method is used to identify the geological boundaries in the DFB region. Among the multiscaling methods of source characterization, the DEXP method independently estimates the homogeneity degree and depth of the sources. The DEXP transformation is tested on the synthetic gravity and magnetic data generated due to isolated and extended sources. The method is further applied to the Bouguer gravity anomaly of the DFB region to delineate the shape and depth information of the sources.

In the thesis, I propose a detailed 2D crustal density model for the first time in the study region. The 3D structural inversion results show that the long-wavelength behavior of the Bouguer gravity anomaly can largely be explained with a prominent upwarp in the Moho interface. The DEXP results also corroborate this regional structure in the form of a horizontal cylinder. The misfit in the anomalies is attributed to the existence of high-density mantle-derived underplated material formed by extension during Proterozoic age. The lateral Moho variations indicate the absence of a northward extension of the DFB underneath the Indo-Gangetic alluvium and deflection of the Moho towards NW direction along the Delhi-Sargodha ridge axis. This likely indicates that the plume head got deflected westward sometime after indentation of the NW corner of the Indian plate and its counter-clockwise rotation after Eocene collision.

LIST OF PUBLICATIONS

Peer-reviewed Journal Publications:

1. **Dwivedi D.**, Chamoli A. and Pandey A.K. 2019. Crustal structure and lateral variations in Moho beneath the Delhi fold belt, NW India: Insight from Gravity data modeling and inversion. Physics of the Earth and Planetary Interiors (under review).

2. **Dwivedi D.** and Chamoli A. 2019. Interpretation of gravity data of Delhi fold belt region using edge detection and Euler deconvolution techniques (to be submitted).

3. **Dwivedi D.** and Chamoli A. 2019. Edge detection of potential field data using wavelet decomposition (to be submitted).

Papers in Conferences/Abstract Volume:

1. Chamoli A. and **Dwivedi D.** 2018. Evidence of underplating below Delhi Fold Belt using gravity data. Abstract (T23B-0371), presented at 2018 AGU Fall Meeting, Washington, D.C., 10-14 December.

2. Chamoli A. and **Dwivedi D.** 2018. Edge enhancement of Potential field data using relative wavelet space entropy. Abstract (NS11A-0573), presented at 2018 AGU Fall Meeting, Washington, D.C., 10-14 December.

3. **Dwivedi D.** and Chamoli A. 2018. Crustal configuration of Proterozoic Delhi fold belt using gravity data and its relation with the Himalayan seismicity. Abstract (SSS11-02), presented at 2018 Japan Geoscience Union Meeting, Makuhari Messe, Chiba, Japan, 20-24 May.

4. **Dwivedi D.** and Chamoli A. 2017. Estimation of source parameters using extreme points of the scaled potential field. 12th Biennial International Conference and Exposition on "Energy Through Synergy", Society of Petroleum Geophysicist, Jaipur, India, 17-19 November.

5. **Dwivedi D.** and Chamoli A. 2016. Enhancement of Gravity signatures of the Delhi-Haridwar ridge. Abstract (P6), presented at 1st Triennial Congress of FIGA, 53rd Annual Convention of IGU and 34th Annual Convention of AHI on "GEOSCIENCES FOR SUSTAINABILITY", IIT (ISM), Dhanbad, 8-10 November.

6. **Dwivedi D.** and Chamoli A. 2016. Source depth estimation using extreme points of the scaled gravity field. Abstract (P116), presented at National Geo-Research Scholars Meet 2016, WIHG, Dehradun, 1-4 June.


भारतीय प्रौद्योगिकी संस्थान रुड़की
INDIAN INSTITUTE OF TECHNOLOGY ROORKEE

ACKNOWLEDGEMENTS

Throughout the research, I was never short of words, but when I had to acknowledge the unrelenting and unconditional support of several people who contributed immensely to this research, I could not find the right words. I consider myself extremely lucky to have a wonderful bunch of people around me.

I am indebted to my supervisor, Dr. Ashutosh Chamoli, Assistant Professor, Department of Earth Sciences, Indian Institute of Technology Roorkee, who is the pivotal force behind the research. I learned a lot from him while writing research papers under his guidance. He is very kind to lend a helping hand whenever in need. His humility and genuine concern for his students is highly appreciable.

I must not forget to thank my research committee members, chairman of student research committee Prof. Sagarika Mukhopadhyay, Prof. Anand Joshi and Dr. Brijesh Kumar for their help and support from the beginning at different stages of my Ph..D work.

I sincerely acknowledge Prof. Sunil Bajpai, Head of Department for his support and providing an excellent work environment in the department.

I extend a special note of thank to Dr. Anand K. Pandey, Scientist, CSIR-NGRI, Hyderabad for giving his valuable time in scientific discussion on the geology of the region.

I also thank all the staff of the department, especially Mr. Kameshwar Dayal Saini, Mr. Nayar (retd.) and Mr. Sarvesh Sharma who have helped me in all possible ways for the lab and official work.

The financial support provided by the Ministry of Human Resources and Development (MHRD), New Delhi to complete the present study and IITR travel support to attend good international conferences are highly acknowledged.

I thank my friends in IIT Roorkee for being my family away from home. A special thanks to my friends Sumit, Rahul, Rabin, Sarvesh, Prabhakar, Kumod, Rajiv, Sajal, Rishi, Kaushal, Avinash, Neeraj, Sanjeev and Rakesh for encouraging me, making my life happier and enjoyable every time.

A special thanks to my elder brother Priyanshu Dwivedi, sister Priyanka Dwivedi and brother in law Dr. Diwaker Nath Shukla for their unconditional love and support. A thanks goes to little niece Divyanka for my source of happiness. Finally, heartfelt gratitude to my mother Kusum Dwivedi, father Ramesh Kumar Dwivedi. Words can never describe how happy and grateful I am to have you.

Roorkee (Divyanshu Dwivedi)
August 05, 2019


भारतीय प्रौद्योगिकी संस्थान रुड़की
INDIAN INSTITUTE OF TECHNOLOGY ROORKEE

TABLE OF CONTENTS

LIST OF FIGURES

LIST OF TABLES

List of notation used

Symbol	**Notation**
BGC	Banded Gneissic Complex
CWT	Continuous Wavelet Transform
DWT	Discrete Wavelet Transform
DFB	Delhi Fold Belt
DSR	Delhi-Sargodha Ridge
DSS	Deep Seismic Sounding
DEXP	Depth From Extreme Points
GBF	Great Boundary Fault
LWFA	Long-wavelength filtered anomaly
SWFA	Short-wavelength filtered anomaly
MB	Marwar Basin
MDSSF	Mahendragarh-Dehradun Subsurface Fault
MIS	Malani Igneous Suite
WSED	Wavelet Source Edge Detector

CHAPTER -1: INTRODUCTION

1.1 RESEARCH BACKGROUND AND PROBLEM

The Delhi fold belt (DFB) represents the Proterozoic Aravalli-Delhi orogeny, which lies as a prominent SW-NE trending transverse structural heterogeneity at the leading edge of the Indian peninsula. The DFB consists of rocks that were intensely folded, deformed, metamorphosed and deposited over an Archaean gneissic basement in the region. The crustal evolution of the DFB is dominated by the interaction of different crustal blocks via Wilson cycles. The Delhi orogeny is an event that evolved around 1100 Ma. The DFB is considered a zone of Proterozoic collision between Marwar craton and Bundelkhand craton (Sinha-Roy et al., 1995). The collision seems to be responsible for listric/major faults in the upper crust, which represents the boundaries of geological formations exposed in the study region. A major terrane boundary separating the region of the Marwar Basin (MB) and the DFB probably resulted during the Mesoproterozoic -Neoproterozoic collisional episode related to the Delhi orogeny (Rao et al., 2000). The Marwar terrane experienced widespread magmatic activity during the Neoproterozoic (around 750 Ma) forming the Malani igneous suite that represents the largest felsic magmatism in India (and the third-largest in the world). Thus, the crustal structure of the DFB is important in terms of tectonic activity. The leading edge of DFB exhibits a large and scattered distribution of smaller earthquake events. Figure 1.1 shows a simplified tectonic and geological map of north west Indian region and area of study.

Past geophysical studies are mainly carried out along the Nagaur-Jhalawar transect (profile CC’, Fig.1.1b) towards the south of the study region ~ 150 km from our profile BB'. The deep seismic sounding (DSS) experiment results (Tewari et al., 1997; Prasad et al., 1998; Rao et al., 2000; Krishna and Rao, 2011; Mandal et al., 2013) and gravity modeling (Mishra et al., 2000) give important information about the crustal structures and its complexities along the transect. The seismic sections reported the disturbing layered structure of the lower crust due to igneous intrusion (Tewari et al., 1997). The seismic section reported in poor reflectivity and showed an abrupt absence of the Moho signature below the DFB, which is although present in the surrounding region. Mishra et al. (2000) have modeled a thicker crust and high-density domal body (3040 kg/m^3) in the lower crust using gravity data with seismic constraints (Tewari et al., 1997) to represent the complex geological setting below the DFB. Rao et al., (2000) suggested a high-velocity thick crust in the Proterozoic orogeny of the region using seismic data. Krishna and Rao (2011) reprocessed and migrated near-offset reflection images, which mark several steeply dipping reflection on the western margin of south DFB interpreted as south Delhi thrust fault. Mandal et al. (2013) reprocessed the DSS profile dataset and reported the thick crust across the Proterozoic DFB. Their results show clear reflection at the Moho below Marwar basin and Sandmata complex, but no reflectivity is observed below the DFB, which they attribute to the low foldage and S/N ratio or the complex geological settings at the lower crust and Mantle boundary. There is no detailed geophysical investigation addressing the subsurface structure of the DFB towards the north (beneath Delhi, Rajasthan and Haryana states). The litho-tectonic units of the DFB are buried under the Quaternary sedimentary cover towards the north and are not expressed in the topography of the region (Fig. 1.1a). Selected studies also report the presence of a basement ridge structure as the Delhi-Haridwar ridge (DHR) below the outer Himalaya in the north and consider this as an extension of the DFB below the Indo-Gangetic plain.

The presence of ridge structure below the Indo-Gangetic plain and the outer Himalaya is proposed using the gravity data (Godin and Harris, 2014), low magnitude seismicity (Arora et al., 2012), and major electric conductive structure derived from magnetotelluric data (Arora et al., 1982; Arora and Mahashabde, 1987). Perhaps, there is no significant signature of the DHR in the basement contours derived by the aeromagnetic datasets (Karunakaran and Ranga Rao, 1976). The leading edge of DFB shows a large and scattered distribution of smaller earthquake events, which is being interpreted as related to Mahendragarh-Dehradun subsurface fault (MDSSF) buried under thick Gangetic alluvium (Shukla et al., 2007). Godin and Harris (2014) report the intriguing problem of understanding the depth extent of the structures due to lack of high-resolution geophysical datasets in the Indo-Gangetic plain, which conceals the peninsular structures. The seismicity is concentrated at the intersection of the MDSSF with the NW-SE trending Delhi-Sargodha ridge, which possibly represents the flexural bulge of the underthrusting Indian plate beneath the Himalaya (Molnar et al., 1973). The interpretations in these studies are qualitative and researchers have pointed lack of understanding in the crustal configuration of the DFB due to speculative inferences. The DFB shows a prominent NNE-SSW (~ 600 km) trending gravity high, but its northward structural extension lacks understanding (Fig. 1.1b). I study the gravity dataset of the region to address this problem by detail modeling of the crustal structure below the DFB.

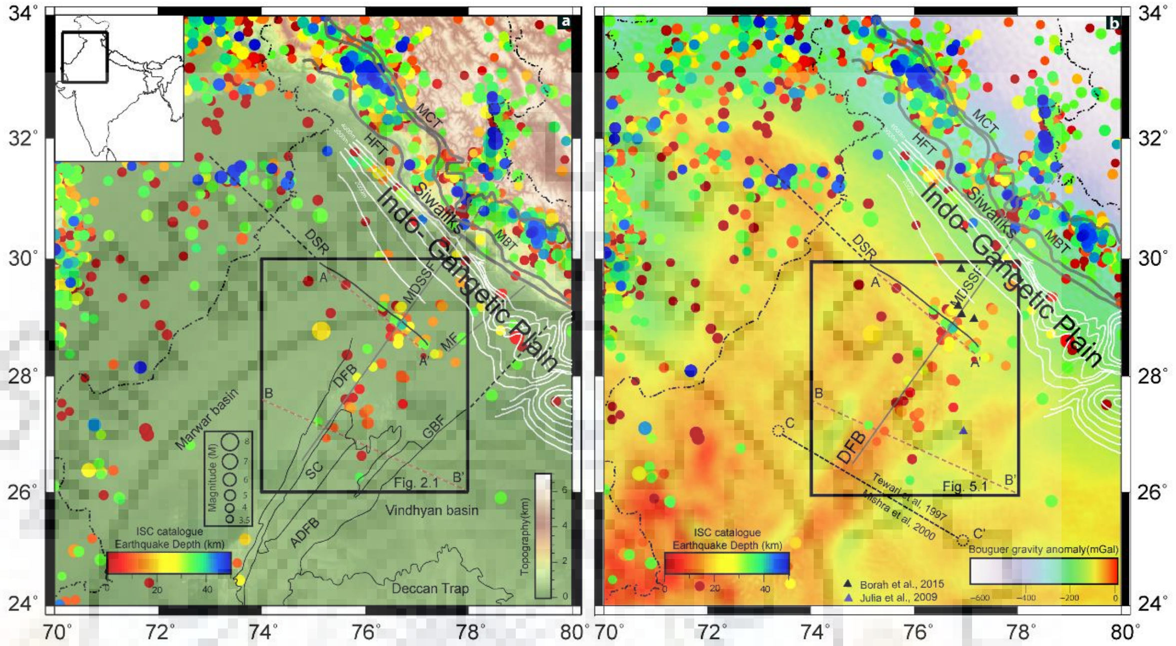

Figure 1.1: a) A simplified tectonic and geological map of NW India showing the Aravalli-Delhi fold belt (ADFB), the Great Boundary fault (GBF) along with the Mahendragarh-Dehradun subsurface fault (MDSSF) and the Moradabad fault (MF) as northward structures (after GSI, 2000; Roy and Jakhar, 2002). b) The Bouguer gravity anomaly (WGM-2012) in the study region. The contours of the basement depth below the Indo-Gangetic plain (after Karunakaran and Ranga Rao, 1976) and seismicity distribution are shown. The inset shows the study region with two gravity profiles AA' and BB,' CC'- Nagaur-Jhalawar transect. HFT- Himalayan Frontal Thrust, MBT- Main Boundary Thrust, MCT- Main Central Thrust, DFB- Delhi Fold Belt, SC- Sandmata Complex, DSR- Delhi-Sargodha Ridge.

1.2 OBJECTIVES

The thesis focuses on detail crustal density modeling of the Delhi fold belt region with structural constraints from the results of different techniques namely: i) Radially averaged power spectrum, ii) Wavelength filtering, iii) 3D structural inversion, iv) Source edge detection method, v) Depth from extreme points (DEXP) method.

The main objectives of the research work are:

1) Identification of lateral source boundaries using gravity data in the DFB region. Development of new efficient methodology for source edge detection.
2) Source characterization of gravity anomaly using the DEXP method- a multiscaling approach to potential field dataset.
3) Modeling and inversion of gravity data to delineate the crustal structure of the Delhi fold belt.

The lateral edges of the sources have a key role in the interpretation of potential field data and help in constraining the subsurface models for understanding the structural settings. Wavelet transform has inherent properties to efficiently extract the information at different scales and thus, applied to delineate the source boundaries. A priori models based on source characterization methods of potential field data reduces the inherent ambiguity (Fedi and Rapolla, 1999; Chamoli et al., 2011). These provide information about the source geometry and depth, which can further be used to constrain detail models. The DEXP is a multiscale method which gives information about the sources without any priori information (Fedi, 2007).

1.3 APPROACH OF THE PROBLEM

I analyzed the Bouguer gravity anomaly using different potential field techniques such as power spectrum, spectral filtering, edge detection, DEXP method and 3D-gravity structural inversion to constraint the crustal density structure of the DFB and surrounding regions of NW India. The approach is summarized as:

a) 2D radially averaged power spectrum is used to derive a priori layered model for further modeling.
b) The Bouguer gravity anomalies are separated based on the characteristics of the power spectrum to understand the deep and shallow structures.

c) The 3D structural inversion is performed on the long-wavelength filtered gravity anomaly to derive the 3D geometry of the Moho interface. The variation of the Moho is used in imaging the 2D density modeling.

d) I developed a wavelet source edge detector method and applied to the short wavelength filtered anomaly to identify the locations of geological boundaries.

e) I have written the MATLAB code of the DEXP method and applied to the Bouguer gravity anomaly of the region to understand the depth behavior and geometry of the sources.

f) The analysis mentioned above is used as a priori information to constrain the density model using the gravity data.

g) The forward modeling is carried out to understand the subsurface structures along two profiles AA' and BB'.

1.4 OVERVIEW OF METHODOLOGIES USED

I briefly give an account of the methodologies used in this study to constraint the gravity model.

1.4.1 Power spectrum analysis

Spector and Grant (1970) formulated the application of power spectrum analysis to aeromagnetic data. The method gives a useful way to estimate the average depths of the interfaces for a layered Earth model. As a matter of fact, it assumes a statistical distribution of homogenous sources (prism) under the hypothesis that the source parameters vary independently. The sources are randomly and uniformly distributed about their mean values. The power spectrum typically shows multisegmented linear curves, where each segment corresponds to the individual interface. The average depth to the interface can be obtained from the slope of log radially averaged power spectrum of gravity or magnetic dataset. The method has been applied in different applications of the gravity and magnetic dataset (Chakraborty and Agarwal, 1992; Chamoli et al., 2011; Kumar M.R. et al., 2013; Yadav et al., 2018).

1.4.2 Source lateral edge detection by wavelet methodology

Wavelet methodologies have shown significant contribution in different fields of earth sciences such as gravity and magnetic source characterization (Moreau and Gilbert, 1999; Martelet et al., 2001; Chamoli et al., 2011; Goyal and Tiwari, 2013), regional residual separation (Fedi and Quarta, 1998;), filtering applications (Ridsdill-Smith and Dentith, 1999; Leblanc and Morris, 2001), bathymetry data (Malamud and Turcotte, 2001), climatic signals (Yan and Jones 2008; Butler et al., 2013), tsunami warning (Telesca et al., 2004; Chamoli et al., 2010; Telesca et al., 2013, 2015) and image coding and compression (Mallat, 1989) etc. Wavelet transform decomposes the signal in time and frequency domain and provides the time-frequency localization of the signal. Wavelet analysis can be worked out in two modes: i) Continuous Wavelet Transform (CWT), ii) Discrete Wavelet Transform (DWT). The CWT is useful for analyzing the time-frequency behavior of the signal. The DWT is a special case of CWT, which is implemented in a multiresolution decomposition algorithm and give information on different frequency content at different levels of decomposition using a pyramidal algorithm.

I use wavelet theory for edge identification and enhancement of the potential field sources. A new wavelet source edge detector (WSED) method is proposed to identify the edges of the sources using two-dimensional potential field dataset. The approach delineates the edges of the sources in individual wavelet coefficient sets (horizontal, vertical and diagonal) and automatically generates the source boundaries from these independent signatures. The method is tested on the magnetic anomaly of the well-known Bishop model. The wavelet representation can differentiate directional properties in the dataset. The method provides useful information for the edges of the sources in independent directions (horizontal, vertical and diagonal). The detail mathematical formulation is discussed in chapter 3.

1.4.3 Source characterization method

Different methods based on the scaling behavior of the potential field are useful to estimate the source structural index and depth information. Main methods among there are: i) Euler deconvolution, ii) CWT method, iii) DEXP method, iv) Multiridge analysis method. The monoscale behavior can be characterized by estimating the source position and structural index (SI) using Euler deconvolution algorithm (e.g., Thompson, 1982; Reid et al., 1990) at a single level and are based on solving a set of linear equations. Other methods such as: i) CWT method (Moreau et al., 1997), ii) DEXP (Fedi et al., 2007), iii) Multiridge analysis (Fedi et al., 2009; Florio and Fedi 2014) use multiscale behavior for source characterization. The DEXP method is used to derive the source geometry (shape) and depth from the gravity data of the Delhi fold belt.

The DEXP characterizes the potential field sources using the multiscale properties of upward continuation field of any derivative order of the potential field data (Fedi, 2007). The scale is equivalent to the altitude of continuation and the method uses extreme points of the scaled potential field to derive the mean depth and shape (structural index) of the sources. These parameters are important for understanding the geometry of the subsurface sources of the anomaly and found useful in building a priori models. The method is stable for anomalies with low S/N (Fedi, 2007). The mathematical formulation of the methodology is discussed in detail in chapter4.

In the present study, the DEXP method is tested on the synthetically generated gravity and magnetic data due to isolated and extended sources and is further applied to the Bouguer gravity anomaly of the DFB region to delineate the source depth and shape.

1.5 THESIS LAYOUT

In the thesis, the crustal structure of the DFB is modeled using gravity anomaly.
Chapter 1 introduces the research problem of the thesis in light of the past research work and the approach used throughout the research work.

Chapter 2 describes the detailed geology and tectonics of the Delhi fold belt region and the geophysical dataset is used in the research work.

Chapter 3 illustrates the theory and application of the wavelet-based method to characterize the source edges and its various applications to the complex synthetic sources and the Bishop model.

Chapter 4 presents the theory and application of the depth from extreme points method.

Chapter 5 describes the application of different methods such as power spectrum analysis, filtering, scaling characteristics, WSED method and 3D structural inversion of the Moho to the gravity anomaly of the DFB region.

Chapter 6 presents the concluding remark and limitations of the research work.

CHAPTER- 2: GEOLOGICAL SETTINGS OF THE REGION AND DATA USED

2.1 REGIONAL GEOLOGY AND TECTONICS OF THE DELHI FOLD BELT

Proterozoic fold belts are the main depositories of information about early plate tectonic interactions and in attempting global correlations. Alluvial sediments of the Indo-Gangetic plain cover the northern portion of the region. The study region comprises parts of Rajasthan, Delhi and Haryana states of the India (Fig. 2.1). The main geological features in the region are i) DFB, ii) MDSSF, iii) Great Boundary Fault (GBF), iv) Delhi-Sargodha Ridge (DSR), v) Banded Gneissic Complexes (BGC), vi) Vindhyan Basin. The Late Archean to Proterozoic rocks in the region constitute of the metamorphic basement of Aravalli-Delhi supergroup overlain by Marwar and Vindhyan sedimentary sequence and Malani Igneous suite (MIS) [Fig. 2.1; Table 2.1].

Past geological studies recognize (Roy, 1988; Sinha-Roy, 1988) four tectonic and magmatic events viz., Archean Banded Gneissic Complex (3000 Ma), Aravalli orogeny (1800 Ma), Delhi orogeny (1100 Ma) and post-Delhi magmatic event (850-750 Ma). The BGC is divided into Sandmata, Mangalwar Complexes and Hindoli Group, which were metamorphosed in granulite facies during the Archean (Sinha-Roy, 1984; Sharma, 1988) and are tectonically separated by Delwara and Banas lineaments (Sinha-Roy et al. 1995, 1998). Synchanthavong and Desai (1977) proposed the eastward subduction of hypothetical Precambrian oceanic plate with the Aravalli and BGC as a proto-continent in the west, which resulted in the evolution of the DFB. Sharma (1995) suggested the formation of the Aravalli fold belt, the Delhi fold belt (both in a combination called Aravalli-Delhi fold belt) and magmatic activities due to crustal thickening by magma addition or underplating caused by decoupling of the mantle lithosphere and subduction. Earlier, Sharma (1988) and Sinha-Roy (1988) suggested two stages of ensialic rifting by ductile extension of hot sialic material, which led to the successive formation of the Aravalli and Delhi fold belts. The rift formation in the North Delhi fold belt was preceded by a Red Sea type rifting in the South Delhi fold belt. The North Delhi belt ended with the development of the Delhi basin into an oceanic trough by 1200 Ma. The Delhi supergroup was deposited over the BGC basement in a system of half grabens and horsts with 10 km thick volcano-sedimentary sequences and are separated by Kaliguman lineament

(Sinha-Roy, 1988). The sediments in the Marwar basin were deposited synchronously with the Neoproterozoic Vindhyans across Aravalli-Delhi complex (Sinha-Roy et al., 1995). The Great Boundary fault separates Hindoli Group from the Vindhyan sedimentary basin in the east. This is followed by generation of the magmatic basin, magmatic arc with the emplacement of Malani volcanic and Erinpura granite marking the termination of Aravalli-Delhi orogeny during Neoproterozoic (850-750 Ma) with the former represents a bimodal (basic-felsic) volcanic, and the later a plutonic suite in island arc and trench after the closure of the trough.

The modern seismicity records show that the intersection of the MDSSF and DSR is the most seismically active zone. A large and scattered distribution of smaller earthquake events in the DFB shows the occurrence of several lineaments buried under thick alluvium (Shukla et al., 2007). The MDSSF has reactivated as thrust with minor strike-slip components. The seismicity of the region may be due to the bending of the lithosphere prior to the under thrusting below the Himalayas (Molnar et al., 1973).

Some researchers have reported that the extension of the DFB behaves as structural heterogeneities on the underthrusting Indian plate and likely control the earthquake ruptures of the Himalayan front. The seismological studies relate these structures with the spatial variation of the seismicity in the region and presume their influence on the Himalayan seismicity by heterogeneous seismic coupling, which obstructs the incoming ruptures of the major earthquakes resulting in low seismicity above these structures (Arora et al., 2012). The seismicity of the Indo-Gangetic plain is low. Valdiya (1976) has first proposed the existence of the northward extension of different transverse structures including the DFB and arc normal convergence in the Himalaya. There are some studies by Oil and Natural Gas Corporation (ONGC), which give the depth of the basement using drilling (Sastri et al., 1971; Karunakar and Ranga Rao, 1976).

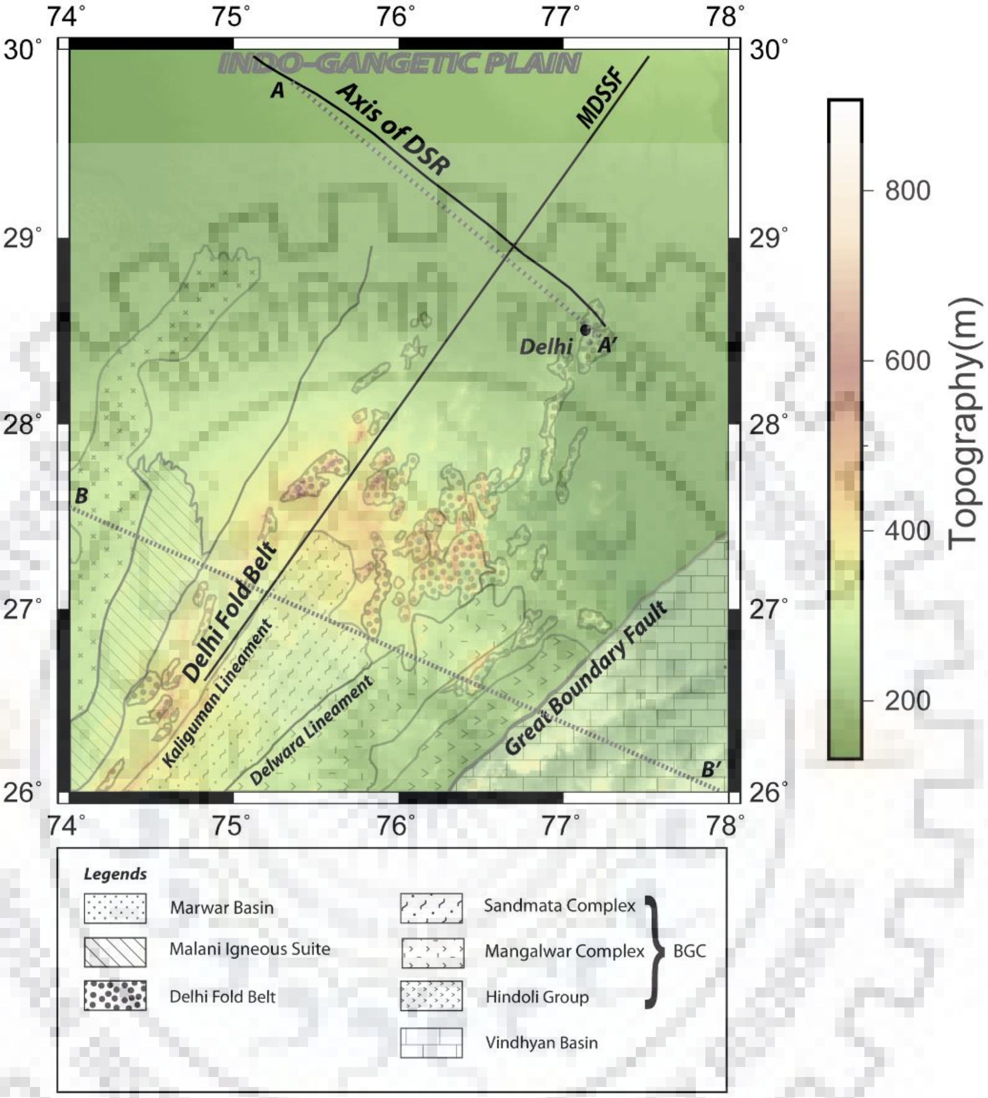

Figure 2.1: Geological and tectonic map of the study region (after Roy and Jakhar, 2002). The figure shows prominent geological structures: Delhi fold belt, the axis of DSR, MDSSF, Great boundary fault, Kaliguman and Delwara lineaments. The two profiles AA' and BB' are used in gravity modeling.

2.2 DATA USED

In the study region, the gravity datasets of the NW Indian region (long. 74° to 78°E and lat. 26° to 30°N) are used. The Bouguer gravity anomaly of the region is extracted from the gravity map series of India-2006, which is a compilation of the gravity datasets acquired by different government organizations like Oil India Limited, Oil and Natural Gas Corporation, Geological Survey of India, Survey of India and National Geophysical Research Institute with an average spacing of ~ 5 km. The earthquake events of magnitude > 3.5 are extracted from the International Seismological Centre online bulletin catalog (2016) for the period from 1900 to 2016 to correlate the seismicity of the region with the subsurface structures. The average density values of rock type in different formations are assigned from previous studies and presented in table 2.1 (Reddy and Ramakrishna, 1988; Ramakrishnan and Vaidyanadhan, 2010).

Table 2.1

The lithostratigraphic units with their characteristics rock type and density

Lithostratigraphic units with age (Ramakrishnan and Vaidyanadhan, 2010)	**Rock type (Ramakrishnan and Vaidyanadhan, 2010)**	**Average density values (kg/m^3)**
Marwar basin (Neoproterozoic: *~550-500 Ma*)	Clay, Dolomite, Evaporites, limestone, Sandstone	2670*
Malani Igneous Suite (Neoproterozoic: *~750-720 Ma*)	Granite, Rhyolite, Basalt, Gabbro	2700*
Delhi fold belt, (Mesoproterozoic: *~1600-900 Ma*)	Calc-schist, Marble, Granite, Gneiss, Marble, Quartzite	2710*
Vindhyan basin, (Mesoproterozoic: *~1600-650 Ma*)	Limestone, Shale, Sandstone,	2560**
Hindoli group, (Paleoproterozoic: *~1850 Ma*)	Felsic and mafic volcanics	2830**
Sandmata complex, (Paleoproterozoic: *~1800-1700 Ma*)	Charnockite bodies, Granulites, Migmatitic gneiss	2850**
Mangalwar complex, (Neoarchean: *~2900-2600 Ma*)	Granitic intrusions, Gneiss, Meta-volcanics, Schist	2820**

*The average density values assigned from Reddy and Ramakrishna (1988).

**The average density values of the rock types in formations from Ramakrishnan and Vaidyanadhan (2010).

CHAPTER - 3: SOURCE EDGE DETECTION USING WAVELET DECOMPOSITION

3.1 INTRODUCTION

In the previous chapter, we have discussed the geology, tectonics and type of geophysical data used in this study. The identification of horizontal edges of the sources play a key role in the interpretation of gravity and magnetic data and are useful in constraining the subsurface models for understanding the geological boundaries of the structural settings. The edge detection methods estimate the boundaries of sources and are useful in mapping the source boundaries in different applications such as mineral exploration, engineering and environmental problems, oil exploration and crustal studies (Fairhead et al., 2011; Sun et al., 2016). The gravity and magnetic anomalies are characterized by amplitude changes due to sources of different physical geometries, depths and density or magnetization properties. The present chapter explains a new method named wavelet source edge detector (WSED), which is proposed for identification of the edges of sources of the 2D potential field data using wavelet decomposition. The method is tested on synthetic gravity and magnetic datasets of complex source geometries and the well-known realistic Bishop magnetic model (Williams et al., 2002). The method is also applied to the gravity dataset of the DFB, which is discussed in chapter 5. The most interesting characteristics of the WSED is the directional information of the source boundaries, which are manifested in the automatically generated “edge plot.” We find this plot very useful for understanding the source boundaries. The identification of the horizontal boundaries of potential field sources is not simple because anomaly shape due to the shape of the source is not fully preserved (Fedi and Florio, 2001). Most common methods for source edge detection are based on derivative analysis, analytical signal, tilt angle and theta map. These methods are described in detail below:

a) Derivative methods

The derivative filter enhances short-wavelength anomalies produced by shallow and small sources. The vertical and horizontal derivatives of the dataset are used for edge detection to define the horizontal location of the source positions (Cordell and Grauch, 1985; Fedi and Florio, 2001; Srivastava et al., 2014; Arisoy and Dikmen, 2015; Dubey and Tiwari, 2016). Evjen (1936) has first proposed the use of vertical derivative to enhance the measured gravity and magnetic data. The zero contour values of the second vertical derivative identify the source boundaries of gravity or magnetic data (Blakely, 1995). The limitations of the derivative filters are seen in the presence of noises, poor data quality or anomalies due to the interference of shallow and deep sources (Hidalgo-Gato and Barbosa, 2015). The different form of horizontal derivatives (total horizontal derivative, total horizontal gradient of the tilt angle, balanced total horizontal derivative) are briefly introduced here.

i) Total horizontal derivative (THDR)

The total horizontal derivative technique was developed by Cordell and Grauch (1985). The highest amplitude values of THDR identify the edges of the anomaly sources. It is given as:

$$THDR = \sqrt{\left(\frac{\partial f}{\partial x}\right)^2 + \left(\frac{\partial f}{\partial y}\right)^2} \qquad (3.1)$$

Where f is the gravity or magnetic anomaly. $\frac{\partial f}{\partial x}$, $\frac{\partial f}{\partial y}$ are the data gradients in the x and y directions. The THDR has limitations in case of the deep structure due to low-density contrast and can not resolve the edge when structures are overlapped.

The tilt angle (TDR) is estimated by normalizing the vertical derivative with respect to the total horizontal derivative (Miller and Singh, 1994). In this method, the peak of the data is positioned over body center and zero values over the edge. It is defined as:

$$TDR = \tan^{-1}\left(\frac{\partial f / \partial z}{THDR}\right) \qquad (3.2)$$

Where $\frac{\partial f}{\partial z}$ is the data gradient in the z-direction. The tilt values lie between $-\pi/2$ to $+\pi/2$ and show a large range of amplitudes for anomalous sources at different depths. The sign of TDR value gives information about the positioning of the source.

ii) The total horizontal gradient of the tilt angle (TDHR)

Verduzco et al., (2004) introduced the total horizontal gradient of the tilt angle as:

$$TDHR = \sqrt{\left(\frac{\partial TDR}{\partial x}\right)^2 + \left(\frac{\partial TDR}{\partial y}\right)^2} \qquad (3.3)$$

The maxima values are used to identify the source edges. This method is theoretically independent of geomagnetic inclination for magnetic data.

iii) Analytical signal amplitude (ASA)

The analytical signal amplitude is defined by the square root of the sum of squares of directional derivatives of the potential field data (Nabighian 1972; Roest et al., 1992; Hsu et al., 1996; Copper, 2009; Srivastava and Agarwal, 2010; Yao et al., 2016). It creates the bell-shaped curve above the sources and maxima values represent the edges of the source (Nabighian, 1972). The ASA for a potential field anomaly (f) for the 3D case is given as:

$$ASA = \sqrt{\left(\frac{\partial f}{\partial x}\right)^2 + \left(\frac{\partial f}{\partial y}\right)^2 + \left(\frac{\partial f}{\partial z}\right)^2} \qquad (3.4)$$

The ASA enhances the smaller amplitude anomalies but has a poor resolution in case of deep sources and the presence of noise (Arisoy and Dikmen, 2015).

iv) The balanced analytical signal (ASB)

The balanced analytical signal uses the orthogonal Hilbert transforms in x and y direction and given as (Cooper, 2009):

$$ASB = \frac{|ASA|}{k + \sqrt{\left[(H_x(|ASA|))^2 + (H_y(|ASA|))^2 + |ASA|^2\right]}} \qquad (3.5)$$

Where H_x and H_y are the Hilbert transform of the analytical signal in both x and y direction respectively. The k is a constant which controls the amount of amplitude balancing applied and generally taken as one.

b) Tilt angle based methods

The tilt angle given by equation 3.2 is used to detect the presence of sources of potential field anomalies. The TDR determines the horizontal location for shallow sources, but overestimate the size in case of deep sources. The tilt filter is used to identify the presence of deep sources in comparison to derivative filters (Hidalgo-Gato and Barbosa, 2015). However, the tilt method has a limitation in the presence of low amplitude anomalies and high-level noises in the data (Santos et al., 2012). Different tilt angle based methods are suggested and briefly defined as:

i) The tilt angle of the horizontal gradient (TAHG)

The tilt angle of the horizontal gradient is an edge detector method which is based on the tilt angle of the total horizontal gradient and is given by (Ferreira et al., 2013):

$$TAHG = \tan^{-1}\left(\frac{\dfrac{\partial THDR}{\partial z}}{\sqrt{\left(\dfrac{\partial THDR}{\partial x}\right)^2 + \left(\dfrac{\partial THDR}{\partial y}\right)^2}}\right) \qquad (3.6)$$

ii) Tilt angle of the first order vertical derivative of the total horizontal gradient (THVH)

The THVH is an edge detector method and is given as (Zhang et al., 2014):

$$THVH = \tan^{-1}\left(\frac{\dfrac{\partial THV}{\partial z}}{\sqrt{\left(\dfrac{\partial THV}{\partial x}\right)^2 + \left(\dfrac{\partial THV}{\partial y}\right)^2}}\right) \qquad (3.7)$$

Where

$$THV = \frac{\partial THDR}{\partial z}$$

The THVH uses the third order derivative of the total field and is sensitive to noises.

c) Theta map (THETA)

The theta map is a phase-based filter for edge detection of causative sources and is a ratio between the total horizontal derivative normalized and analytical signal amplitude (Wijns et al., 2005):

$$THETA = \cos^{-1}\left(\frac{THDR}{ASA}\right) \qquad (3.8)$$

The THETA map detects edges independently to the amplitude and strike and is suggested for magnetic data at low latitudes.

3.2 WAVELET BASED SOURCE EDGE DETECTION

Wavelet transform handles the information of different scales in the dataset in an optimum way and thus, can be used to extract the selective information at different scales. Wavelet analysis is generally carried out in two forms i) CWT, ii) DWT.

3.2.1 Continuous wavelet transform

The CWT of a function f(t) is given as:

$$W_{\psi/f}(a,b)=\int_{-\infty}^{+\infty}\frac{1}{\sqrt{a}}\psi^{*}\left(\frac{t-b}{a}\right)f(t)\,dt \qquad a,b\in R,\ a>0 \qquad (3.9)$$

Where ψ^{*} is the complex conjugate of analyzing wavelet $\psi(t)$ known as kernel or mother wavelet, a is the dilation (scale) which is inversely proportional to frequency, b is the translation parameter and R is set of real numbers. The factor $1/\sqrt{a}$ is used to normalize the energy of function at various scales (Daubechies, 1992). The wavelet function translates and dilates over the series continuously and thus cover different frequency components.

3.2.2 Discrete wavelet transform

The DWT is a special case of CWT which represents the discrete analysis. For DWT, the parameters a, b of equation 3.9 are given as (Daubechies, 1992):

$$a=\alpha^{p} \text{ and } b=n\beta\alpha^{p}, \qquad n,p\in Z \quad \alpha>1,\beta>0 \qquad (3.10)$$

Where n and p control degree of dilation and translation respectively. If the signal is of length, $N=2^{j}$ then (j + 1), wavelet levels can be shown. The multiscale nature of DWT is useful to understand the behavior of signal at different frequencies or scales and extract information from different frequency bands (Mallat, 1989).

3.3 MULTIRESOLUTION ANALYSIS USING 2D DWT

Wavelet multiresolution decomposition provides useful information content about 2D data/images by defining a wavelet representation which is calculated using the pyramidal algorithm. The two-dimensional dataset of potential field can be decomposed into approximation and detail coefficients at different levels using 2D discrete wavelet transform. The approximation coefficients correspond to low spatial frequencies, and the scaledependent hierarchies of the detail coefficients correspond to high spatial frequencies (Mallat, 1989). The discrete wavelet transform decomposes the data in approximation coefficients (W) and detail coefficients [Horizontal (H), Vertical (V) and Diagonal (D)] using scaling function (ϕ) and wavelet function (ψ) respectively. The mathematical approach of the multiresolution decomposition is explained in Appendix A.

3.4 WAVELET SOURCE EDGE DETECTOR (WSED) METHOD

The distinct edges of any source give signatures in wavelet approximation coefficients as well as the detail coefficients. The horizontal, vertical and diagonal wavelet detail coefficients show high amplitudes corresponding to high spatial frequencies in y-axis, x-axis and both directions respectively. These coefficients are useful in identifying the source edges along these directions (Mallet, 1989).

3.4.1 2D DWT using Haar wavelet

In data processing, objects are best analyzed with matrices. If we are interested in $M \times L$ matrix c of the form $c = \{c(n,m) : 0 \le n \le M-1; 0 \le m \le L-1\}$. We generalize the 2D signal of the discrete along the rows and column of the signal.

3.4.2 Row and column-wise approximation and details

The generalization of the Haar wavelet to 2D signals shows separate application to the rows and columns of the signal. We have briefly summarized the mathematics of Haar wavelet along rows and columns here. The Row and column-wise- approximation and details theory can be seen in Walnut (2002).

The row-wise approximation matrix of c, $\mathbf{H}^{row}c$ to be of $M \times (L/2)$ matrix is defined as:

$$(\mathbf{H}^{row}c)(n,m) = \frac{1}{\sqrt{2}}c(n,2m) + \frac{1}{\sqrt{2}}c(n,2m+1) \tag{3.11}$$

The row-wise detail matrix of c, $\mathbf{G}^{row}c$ to be of $M \times (L/2)$ matrix is defined as:

$$(\mathbf{G}^{row}c)(n,m) = \frac{1}{\sqrt{2}}c(n,2m) - \frac{1}{\sqrt{2}}c(n,2m+1) \tag{3.12}$$

$\mathbf{H}^{row}c$ and $\mathbf{G}^{row}c$ are the matrices obtained by multiplying each row of c by the matrices H and G respectively.

The column-wise approximation matrix of c, $\mathbf{H}^{col}c$ to be of $(L/2) \times M$ matrix is defined as:

$$(\mathbf{H}^{col}c)(n,m) = \frac{1}{\sqrt{2}}c(2n,m) + \frac{1}{\sqrt{2}}c(2n+1,m) \tag{3.13}$$

The column-wise detail matrix of c, $\mathbf{G}^{col}c$ to be of $(L/2)\times M$ matrix is defined as:

$$(\mathbf{G}^{col}c)(n,m) = \frac{1}{\sqrt{2}}c(2n,m) - \frac{1}{\sqrt{2}}c(2n+1,m) \tag{3.14}$$

$\mathbf{H}^{col}c$ and $\mathbf{G}^{col}c$ are the matrices obtained by multiplying each column of c by the matrices H and G respectively.

3.4.3 Haar wavelet for matrices

The Haar wavelet for matrices is briefly summarized here. For simplicity, It is assumed that the matrices are in square form and number of rows and column of these matrices are the power of two means, c is always a $2^N \times 2^N$ matrix for some $N \in \mathbf{N}$. The details can be seen in Walnut (2002).

Given $J, N \in \mathbf{N}$ with $J < N$ and a matrix $c_0 = \{c(n,m)\}_{n,m=0}^{2^N-1}$ for $1 \le j \le J$, We define the $2^{N-j} \times 2^{N-j}$ matrices c_j, $d_j^{(1)}$, $d_j^{(2)}$ and $d_j^{(3)}$ as: (Walnut, 2002)

$$c_j = \mathbf{H}^{col}\,\mathbf{H}^{row}\,c_{j-1,} \tag{3.15}$$

$$d_j^{(1)} = \mathbf{G}^{col}\,\mathbf{H}^{row}\,c_{j-1,} \tag{3.16}$$

$$d_j^{(2)} = \mathbf{H}^{col}\,\mathbf{G}^{row}\,c_{j-1,} \tag{3.17}$$

$$d_j^{(3)} = \mathbf{G}^{col}\,\mathbf{G}^{row}\,c_{j-1,} \tag{3.18}$$

Where $\mathbf{H}^{col}, \mathbf{G}^{col}, \mathbf{H}^{row}, \mathbf{G}^{row}$ are the $2^{N-j-2} \times 2^{N-j-1}$ matrices. The DHT of c_0 is a collection of the matrices

$$\{d_j^{(1)}, d_j^{(2)}, d_j^{(3)}\}_{j=1}^{J} \cup \{c_J\}. \tag{3.19}$$

3.4.4 Horizontal, vertical and diagonal edges using Haar wavelet

Each element in a 2D matrix data has eight other neighboring elements, two in the horizontal direction, two in the vertical direction and four in the diagonal direction. If at a given position, the variation of the element is small in the vertical direction but large in the horizontal direction, then the element is a vertical edge point of the data. Similarly, if the variation of the element is small in the horizontal direction but large in the vertical direction, then the element is a horizontal edge point of the data. If the variation is large in both directions, then the element is a diagonal edge point of the data.

Since the Haar wavelet for matrices comprises to compute the averages and differences of the adjacent element in various combinations, we can find the edges in a data using the Haar wavelet coefficients.

If we consider a $2^{N-1}\times 2^{N-1}$ matrix $d_1^{(1)}$ derived form a matrix $c_0=\{c(n,m)\}_{n,m=0}^{2^N-1}$ for $0\le n,m\le 2^{N-1}$

As we know that $d_1^{(1)}=\mathbf{G}_{2^N}^{row}\,\mathbf{H}_{2^N}^{row}\,c_0$, then we have by (3.1.3) and (3.14)

$$d_1^1(n,m)=\frac{1}{\sqrt{2}}\mathbf{H}_{2^N}^{row}\,c_0(2n,m)-\frac{1}{\sqrt{2}}\mathbf{H}_{2^N}^{row}\,c_0(2n+1,m)\quad\text{(Walnut, 2002)}$$

$$=\frac{1}{2}(c_0(2n,2m)+c_0(2n,2m+1))-\frac{1}{2}(c_0(2n+1,2m)+c_0(2n+1,2m+1))$$

$$=\frac{1}{2}(c_0(2n,2m)-c_0(2n+1,2m))+\frac{1}{2}(c_0(2n,2m+1)-c_0(2n+1,2m+1))\qquad(3.20)$$

The following results are drawn:

a) If $(2n,2m)$ is a horizontal edge point of the data c_0, then the differences $c_0(2n,2m)-c_0(2n+1,2m)$ and $c_0(2n,2m+1)-c_0(2n+1,2m+1)$ will tend to be large value due to the large variation in the element in the vertical direction.

b) If $(2n,2m)$ is a vertical edge point, then the same differences will tend close to zero.

c) If $(2n,2m)$ is a diagonal edge point, then the element will tend to be similar in one of the diagonal directions or one of the differences tends to zero.

Since the matrix c_j can be thought of as containing the property of original matrix that is of a size 2^j or larger, the matrices $d_j^{(1)}$, $d_j^{(2)}$ and $d_j^{(3)}$ are called horizontal, vertical and diagonal edges respectively at scale 2^j.

I propose a methodology to extract these directional patterns for identification of the edges of sources in the potential field.

The methodology is summarized in the following steps:

1. 2D gravity or magnetic data is decomposed into approximation and detail coefficients (horizontal, vertical, diagonal) at level n (where n > 0) using the Haar wavelet.

2. The approximation coefficients identify all edges of the sources, whereas the detail coefficients are useful in extracting the edges in the form of different directional components.

3. The local maxima of the absolute values of the horizontal, vertical and diagonal detail coefficients are determined. Then, a threshold (~ 3%) on prominence of the local maxima is applied to identify different directional edges of the source. The prominence of a peak measures how much peak stands out due to its intrinsic height relative to other peaks. The magnitude of prominence is the property of a signal that is commonly used to filter extrema (Gilgen, 2006).

4. The local maxima of vertical and horizontal coefficients are aligned along the source boundaries corresponding to the orthogonal directions, whereas the local maxima of the diagonal coefficients are distinct and represent the vertices of the sources.

5. The algorithm compiles these edges of the sources and plots the integrated information in the form of the "edge plot" with directional information (horizontal, vertical and diagonal) by different colors (Blue, red and green).

The flow chart of the algorithm is shown in figure 3.1.

FLOW CHART OF EDGE PLOT

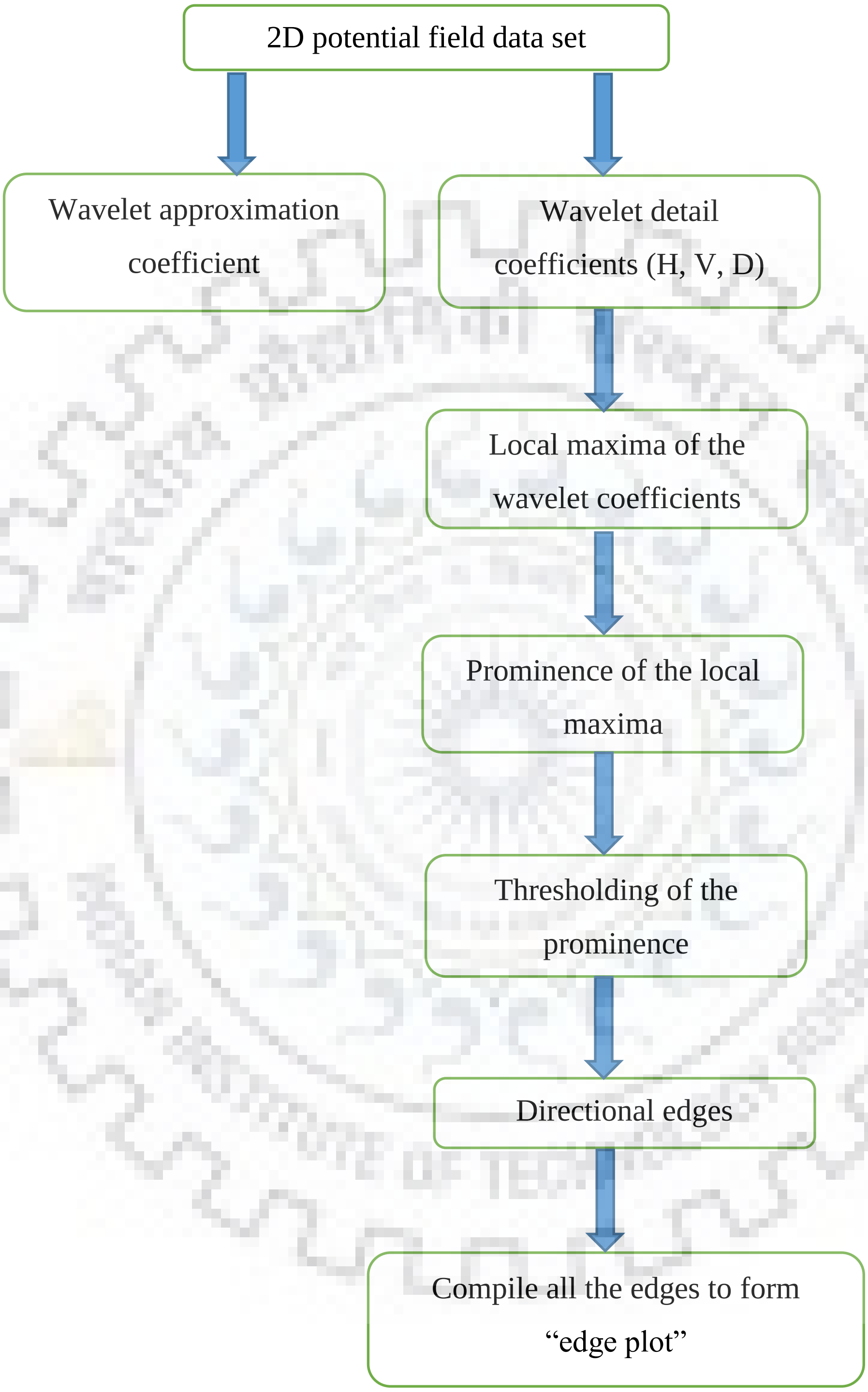

Figure 3.1: Flow chart to derive "edge plot" in the WSED.

The WSED method is applied to different synthetic and realistic cases. The wavelet horizontal detail coefficients (H) give high amplitude along y-axis (lateral edge) and low along x-axis, whereas the wavelet vertical detail coefficient (V) gives high amplitude along x-axis (lateral edge) and low along y-axis. The wavelet diagonal detail coefficients (D) give a high amplitude in both directions (diagonal edge) and thus determine the edges at the vertices. The magnitude of prominence is used to filter extrema. The different thresholding values are applied and checked based on the percentage of the maximum value of the prominence (P) to identify the edges of the sources. The threshold value (> 3% of P) is used in the study of synthetic, Bishop model and a real case of DFB. The edge-plots show useful information in the form of lateral and vertices of the source boundaries. The signatures in wavelet detail coefficients show distinct patterns for isolated and extended sources, which is clearly seen in the following cases. The isolated sources are characterized by a high amplitude of all the wavelet detail coefficients, whereas extended sources show prominent wavelet detail coefficient in the respective direction of extension of source.

3.5 APPLICATION OF WSED TO SYNTHETIC CASES

The methodology is applied to gravity and magnetic anomalies due to 3D synthetic source models to evaluate its efficiency. Three synthetic cases (G1, M1, and M2) of different geometries are generated using prismatic bodies located at different depths. The dataset is generated on 100000 x 100000 m grid with a spacing of 1000 m for gravity model and 6000 x 6000 m grid with a spacing of 15 m for the magnetic model both in x and y directions (Table 3.1). The magnetic prismatic bodies are generated with magnetic inclination and declination at 90° and 0°.

Table 3.1

The parameters of the synthetic cases of gravity (G1) and magnetic (M1, M2) models

Model	Prismatic source	Z top(m)	Length (m)	Width (m)	Extent (m)	M (A/m)	Density contrast (kg/m^3)
G1	A1	1000	16000	10000	7000	-	300
	A2	5000	25000	9000	5000	-	300
	A3	3000	20000	10000	9000	-	300
	A4	8000	12000	33000	8000	-	300
	A5	4000	28000	10000	9000	-	300
	A6	12000	14000	29000	8000	-	300
M1	B1	100	3000	500	1000	1	-
	B2	200	3000	500	1000	1	-
	B3	300	3000	500	1000	1	-
M2	P1	500	500	2500	700	0.4	-
	P2	500	2500	500	700	0.4	-
	P3	500	2200	2200	400	0.4	-
	P4	300	1000	1000	200	0.4	-
	P5	100	500	500	200	0.4	-

Figure 3.2 shows the 3D synthetic model (G1) consisting of six prisms (A1, A2, A3, A4, A5, A6) of the same dimensions at different depths and the corresponding gravity anomaly map. The dataset is decomposed into wavelet approximation and detail coefficients at first level using Haar wavelet (Fig. 3.3 a, b, c, d). I have calculated the wavelet approximation coefficients, which show prominent signatures of edges of all sources (Fig.3.3a). The calculated wavelet horizontal detail coefficients show the high amplitude of the coefficients in the vertical direction and zero amplitude in the horizontal direction, thus determine the lateral edges of the sources (Fig. 3.3b). The calculated wavelet vertical detail coefficients show high amplitude in the horizontal direction and zero amplitude in the vertical direction, thus determine the lateral edge of the sources (Fig. 3.3c). The calculated wavelet diagonal detail coefficients show high amplitude at the four vertices of the prisms (both directional edge points) and zero amplitude elsewhere, thus determine the diagonal edge of the sources (Fig. 3.3d). The figure 3.3e shows the “edge plot” derived after applying thresholding based on the prominence of the local maxima of wavelet coefficients.

Figure 3.4 shows 3D synthetic model (M1) consisting of three prisms (B1, B2, B3) of the same dimension at different depths and its total magnetic anomaly map. The dataset is decomposed into wavelet approximation and detail coefficients at first level (Fig. 3.5 a, b, c, d). The depth of the prisms increases in the order of B1, B2, and B3. The prominence of the local maxima of the wavelet coefficients and threshold gives “edge plot” of the synthetic prismatic sources (Fig. 3.5e).

The third case represents complex sources using five prisms (P1, P2, P3, P4, P5) [Fig. 3.6a]. This model (M2) is generated analogous to complex geological settings with edges of different spatial dimensions and depth extent. This example is used to test the methodology for the realistic conditions of interference of the total magnetic anomalies due to different sources (Fig. 3.6b). The calculated wavelet approximation and detail coefficients show directional characteristics as noted in the previous case (Fig. 3.7 a, b, c, d). The wavelet detail coefficients identify the interfering prism (P3, P4, and P5), which lies at different depths. The edge plot enhances the source edges (Fig. 3.7e). This case clearly shows the efficiency of the proposed method in complex scenarios of source boundaries.

The directional behavior of the wavelet detail coefficients is given in table 3.2, which indicate the identified edges.

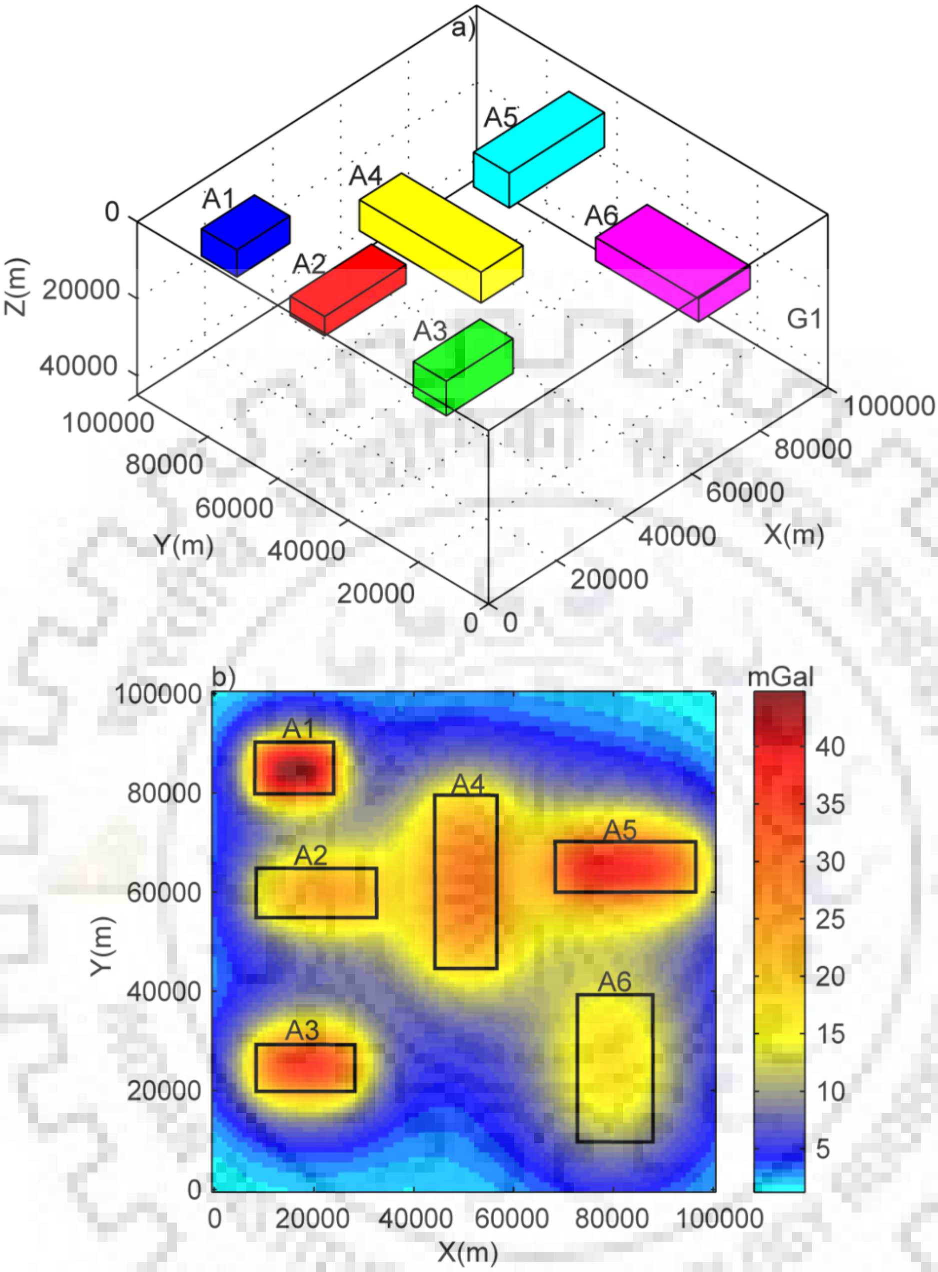

Figure 3.2: a) 3D synthetic model (G1) consisting of six prisms (see table 3.1 for source parameters), b) gravity anomaly due to model G1.

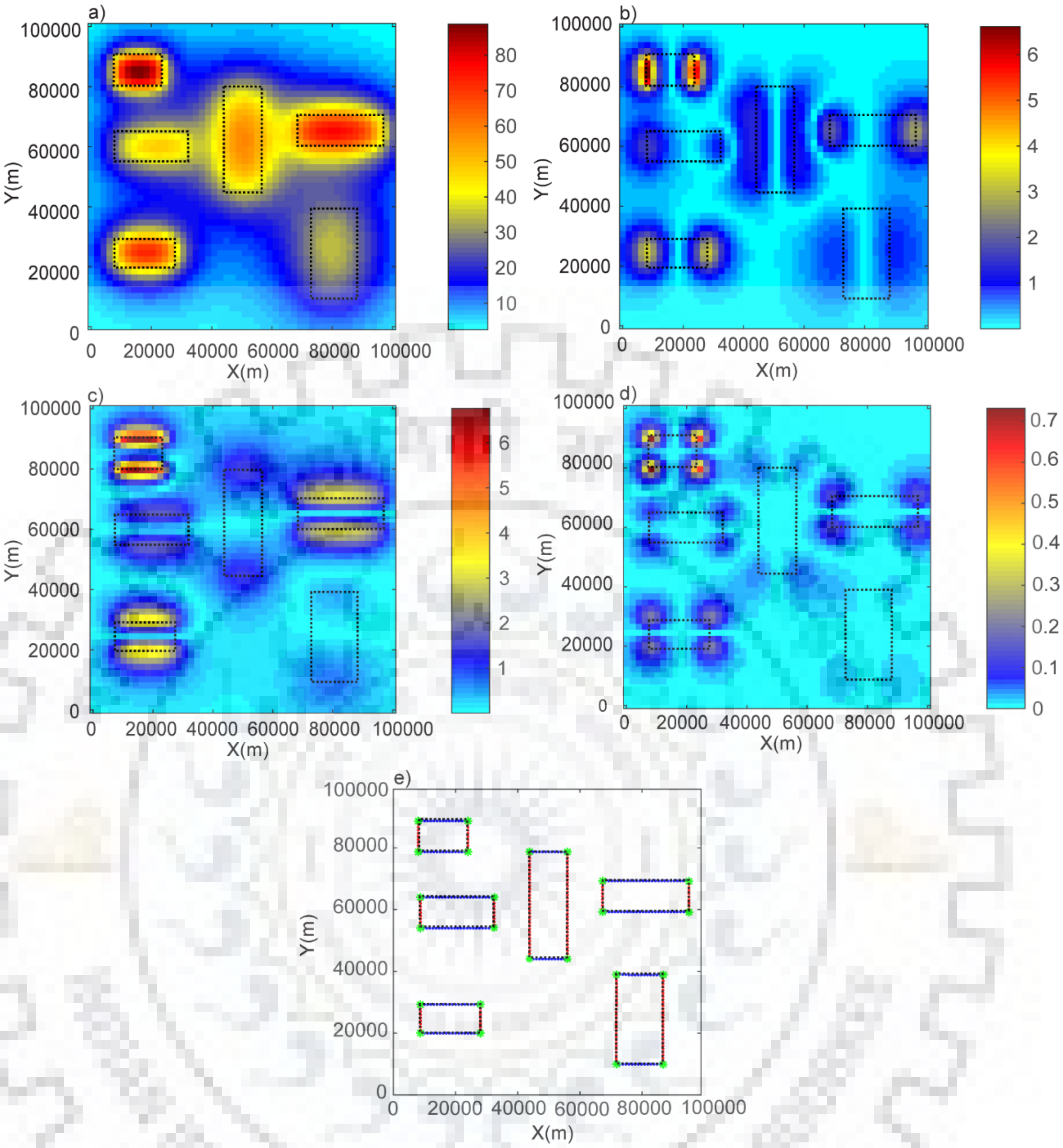

Figure 3.3: Wavelet decomposition of the gravity anomaly due to the synthetic model G1, a) wavelet approximation coefficients, b) wavelet horizontal detail coefficients, c) wavelet vertical detail coefficients, d) wavelet diagonal detail coefficients. Note the signatures in different wavelet coefficients corresponding to source boundaries shown by dotted lines. e) The source boundaries derived from horizontal, vertical and diagonal wavelet coefficients (represented by blue, red and green colors respectively) are compiled in the form of edge plot.

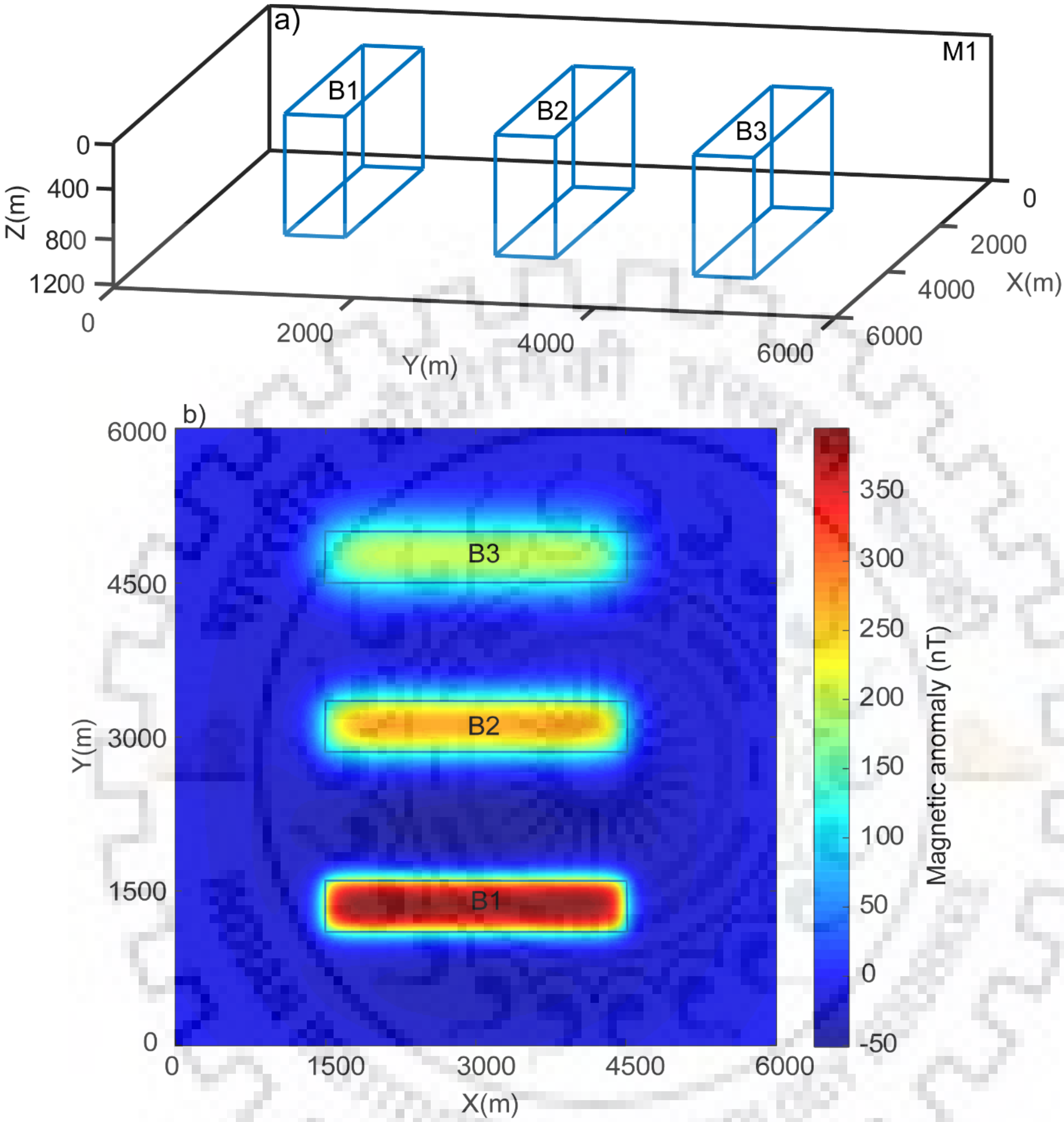

Figure 3.4: a) 3D synthetic model (M1) consisting of three prisms (see table 3.1 for source parameters), b) total magnetic anomaly due to model M1.

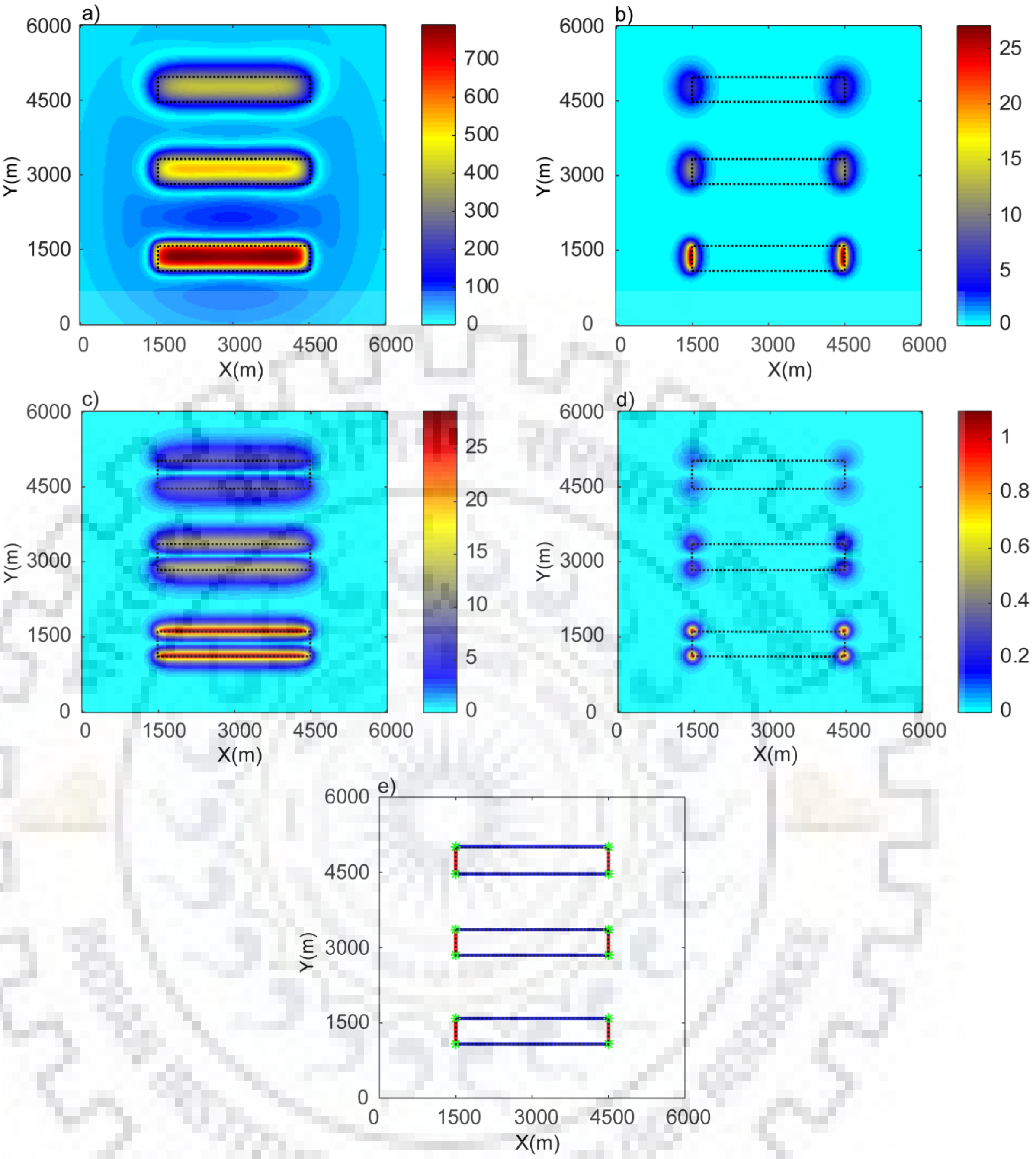

Figure 3.5: Wavelet decomposition at level one of the magnetic anomaly due to the synthetic model M1, a) wavelet approximation coefficients, b) wavelet horizontal detail coefficients, c) wavelet vertical detail coefficients, d) wavelet diagonal detail coefficients. Note the signatures in different wavelet coefficients corresponding to source boundaries shown by dotted lines. e) The edge plot.

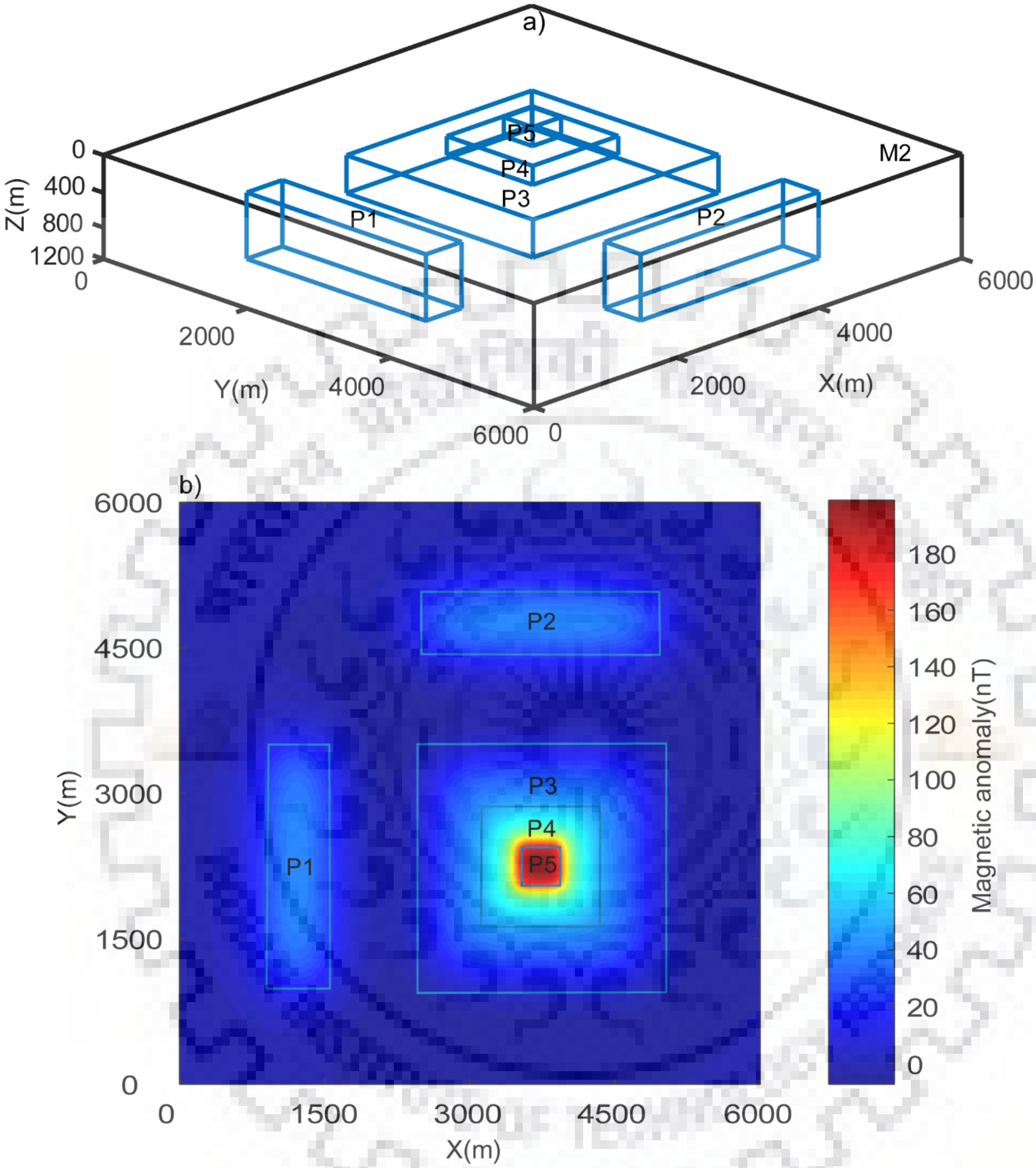

Figure 3.6: a) 3D synthetic model (M2) consisting of five prisms (see table 3.1 for source parameters), b) total magnetic anomaly due to model M2.

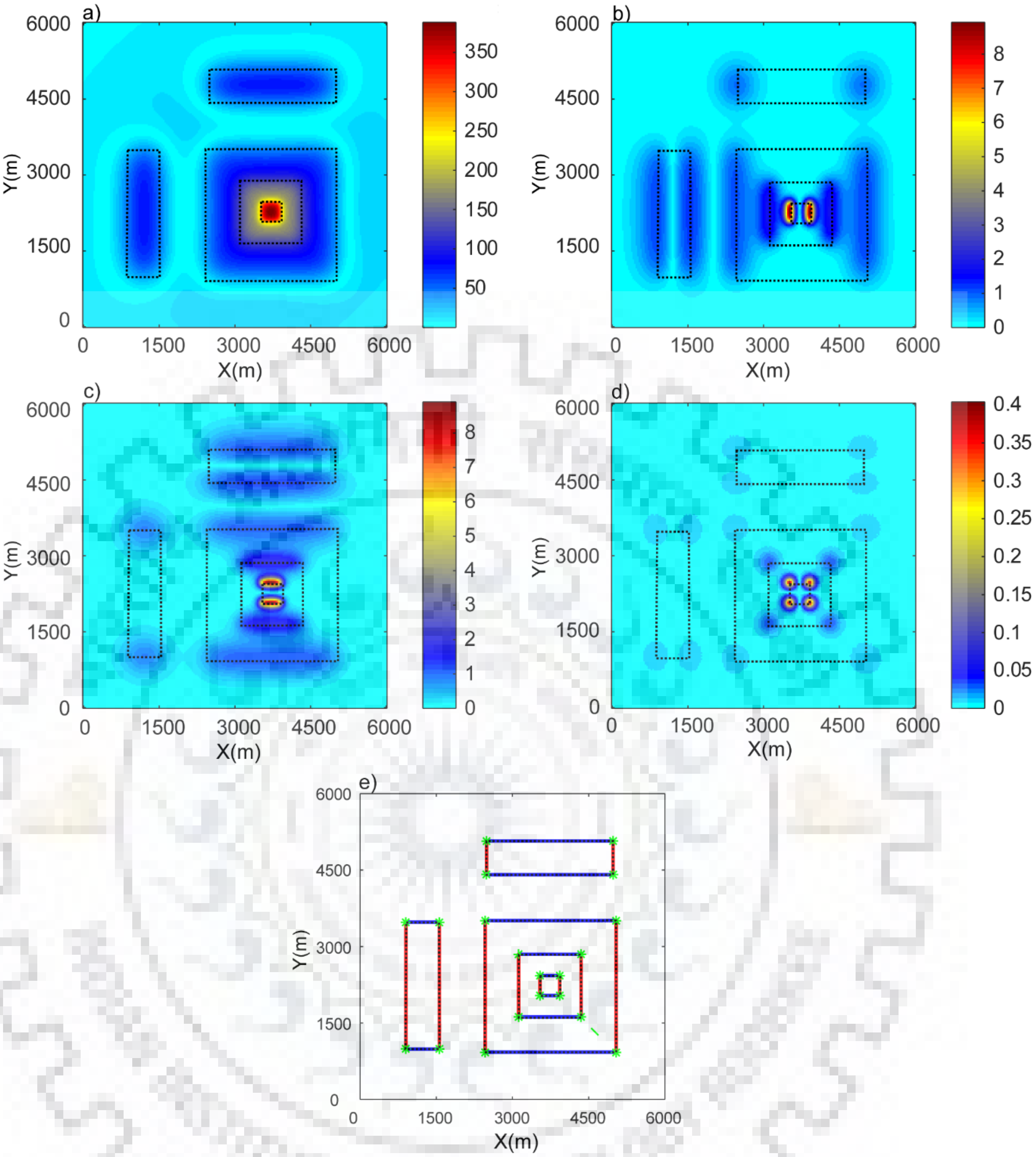

Figure 3.7: Wavelet decomposition at level one of the magnetic anomaly due to the synthetic model M2, a) wavelet approximation coefficients, b) wavelet horizontal detail coefficients, c) wavelet vertical detail coefficients, d) wavelet diagonal detail coefficients. Note the signatures in different wavelet coefficients corresponding to source boundaries shown by dotted lines. e) The edge plot.

Table 3.2

Directional variation of wavelet detail coefficients (H, V, and D) in edge plots

Model	Prismatic source	Detail Coefficients	Directional values			
			x-axis (amplitude)	y-axis (amplitude)	vertices (amplitude)	edge of the source
G1	A1	H	Zero	High	Zero	Lateral
		V	High	Zero	Zero	Lateral
		D	Zero	Zero	High	Diagonal
	A2	H	Zero	High	Zero	Lateral
		V	High	Zero	Zero	Lateral
		D	Zero	Zero	High	Diagonal
	A3	H	Zero	High	Zero	Lateral
		V	High	Zero	Zero	Lateral
		D	Zero	Zero	High	Diagonal
	A4	H	zero	High	Zero	Lateral
		V	High	zero	zero	Lateral
		D	zero	zero	High	Diagonal
	A5	H	zero	High	zero	Lateral
		V	High	zero	zero	Lateral
		D	zero	zero	High	Diagonal
	A6	H	zero	High	zero	Lateral
		V	High	zero	zero	Lateral
		D	zero	zero	High	Diagonal
M1	B1	H	zero	High	zero	Lateral
		V	High	zero	zero	Lateral
		D	zero	zero	High	Diagonal
	B2	H	zero	High	zero	Lateral
		V	High	zero	zero	Lateral
		D	zero	zero	High	Diagonal
	B3	H	zero	High	zero	Lateral
		V	High	zero	zero	Lateral

		D	zero	zero	High	Diagonal
M2	P1	H	zero	High	zero	Lateral
		V	High	zero	zero	Lateral
		D	zero	zero	High	Diagonal
	P2	H	zero	High	zero	Lateral
		V	High	zero	zero	Lateral
		D	zero	zero	High	Diagonal
	P3	H	zero	High	zero	Lateral
		V	High	zero	zero	Lateral
		D	zero	zero	High	Diagonal
	P4	H	zero	High	zero	Lateral
		V	High	zero	zero	Lateral
		D	zero	zero	High	Diagonal
	P5	H	zero	High	zero	Lateral
		V	High	zero	zero	Lateral
		D	zero	zero	High	Diagonal

3.6 COMPARISON WITH CONVENTIONAL METHODS

The common methods (THDR, TDR, TDHR, ASA, ASB, TAHG, THVH, THETA) are tested for the magnetic anomaly due to model M2 (Fig. 3.6). The results are compared with the WSED method (Fig. 3.7). The results of the conventional methods are discussed here and summarized in table 3.3.

a) The estimated total horizontal derivative (THDR) map of the magnetic anomaly is presented in figure 3.8a. The anomaly shows its maximum value at the source edge and the minimum value at the central part (P3, P4, P5). The actual edges due to source P1 and P2 are not clearly identified due to the decrease in the amplitude of the signal with increasing depth.

b) The computed tilt angle (TDR) map of the magnetic anomaly is shown in figure 3.8b. As expected, the minimum of the anomaly is positioned over the edge of sources (P1, P2, P3, P5) and equalizes the signal amplitude. It is difficult to distinguish edges from superimposed source especially for the source P4.

c) The calculated total horizontal gradient of the tilt angle (TDHR) of the magnetic anomaly is displayed in figure 3.8c. Same as THDR, the amplitude of the signal decreases with increasing depth of sources. The edge of the sources is determined by a sharp peak (P1, P2, P5). The interfering sources (P3, P4) do not identify the edges.

d) The analyzed analytical signal amplitude (ASA) of the magnetic anomaly is presented in figure 3.8d. The amplitude of the signal decreases as the depth of sources increases. The deeper source edges (P1, P2, and P3) are not clearly identified.

e) The balanced analytical signal (ASB) of the magnetic anomaly is shown in figure 3.8e. It is calculated with constant k=1. The ASB shows a better response in boundary identification of sources than THDR method. The ASB resolve source (P1, P2, P3, P4, P5) edges by determining the peak of the signal.

f) The computed TAHG method of magnetic anomaly is presented in figure 3.8f. The maximum value of the signal directly characterizes the edges of both shallow (P4, P5) and deep sources (P1, P2). The edge due to source P3 does not coincide with an actual edge.

g) The calculated THVH of the magnetic anomaly is displayed in figure 3.8g. The maximum value of the signal directly represents the edges of sources. The edge due to sources (P1, P2, P4, P5) is clearly identified except P3.

h) The THETA map demarcates the source edges by maximum values. However, the results are poor for deeper sources (P1, P2, P3), where the identified edges are not overlapping with the assumed ones.

ASB, TAHG and THVH are showing the exact mapping of the edges among all methods tested.

The WSED method demonstrates the following advantages over the conventional source edge detector methods.

a) It resolves the lateral and diagonal edges independently in the form of edge plot (Fig. 3.7e), whereas the conventional methods produce overall edges.

b) It is noteworthy to see the edge identification in the WSED edge plots for both shallow and deep sources in case of complex geometries (model M2) for which most of the conventional methods (TDR, TDHR, ASA, Theta) fail.

c) The WSED enhances the edges to be more visible and sharp compared to the derivatives based techniques.

Table 3.3

Edge identification using conventional methods for the model M2

Model	**Method**	**Amplitude of the anomaly**	**P1**	**P2**	**P3**	**P4**	**P5**
M2	THDR	Max	I, NC	I, NC	I, C	I, C	I, C
	TDR	Min	I, NC	I, NC	I, C	NI	I, C
	TDHR	Max	I, NC	I, NC	NI	NI	I, C
	ASA	Max	NI	NI	NI	I, C	I, C
	ASB	Max	I, NC	I, NC	I, NC	I, NC	I, C
	TAHG	Max	I, C	I, C	I, NC	I, C	I, C
	THVH	Max	I, C	I, C	I, NC	I, C	I, C
	THETA	Max	I, NC	I, NC	I, NC	NI	I, C

Note: i) I- source edges are *identified* with the applied method, ii) NI- source edges are *not identified*, iii) C- identified edges are *coinciding* with assumed one, iv) NC- identified edges are *not coinciding* with assumed one.

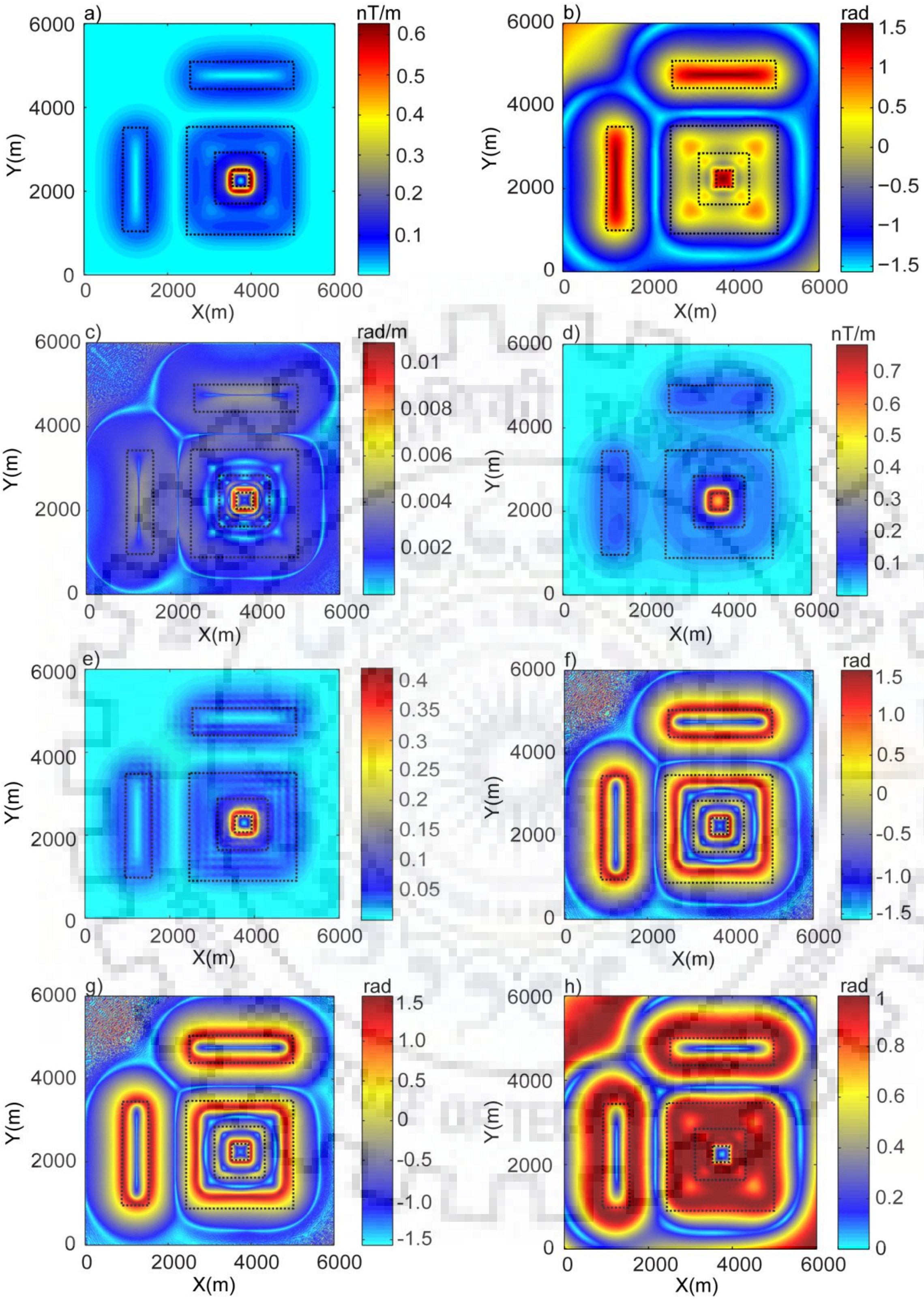

Figure 3.8: Comparison of different techniques to identify source edges for the Model M2. a) THDR, b) TDR, c) TDHR, d) ASA, e) ASB, f) TAHG, g) THVH, h) THETA.

3.7 ADDITION OF GAUSSIAN NOISE

The WSED method is tested on the total magnetic anomaly with the addition of one percent of the Gaussian noise to the maximum amplitude of model M2 (Fig. 3.6b). The corresponding total magnetic anomaly is presented in figure 3.9a. The calculated wavelet approximation coefficients are shown in figure 3.9b. The approximation coefficients identify all edges of the sources. The calculated wavelet horizontal and vertical detail coefficients identify the lateral edge of the source efficiently (Fig. 3.9c, d). The calculated diagonal detail coefficients show more virtual vertices than the actual one (Fig. 3.9e). The figure 3.9f shows the edge plot derived from horizontal, vertical and diagonal wavelet detail coefficients (blue, red and green) due to these prismatic sources. The WSED method is less susceptible to noise. It provides improved detail edges of separated and superimposed sources.

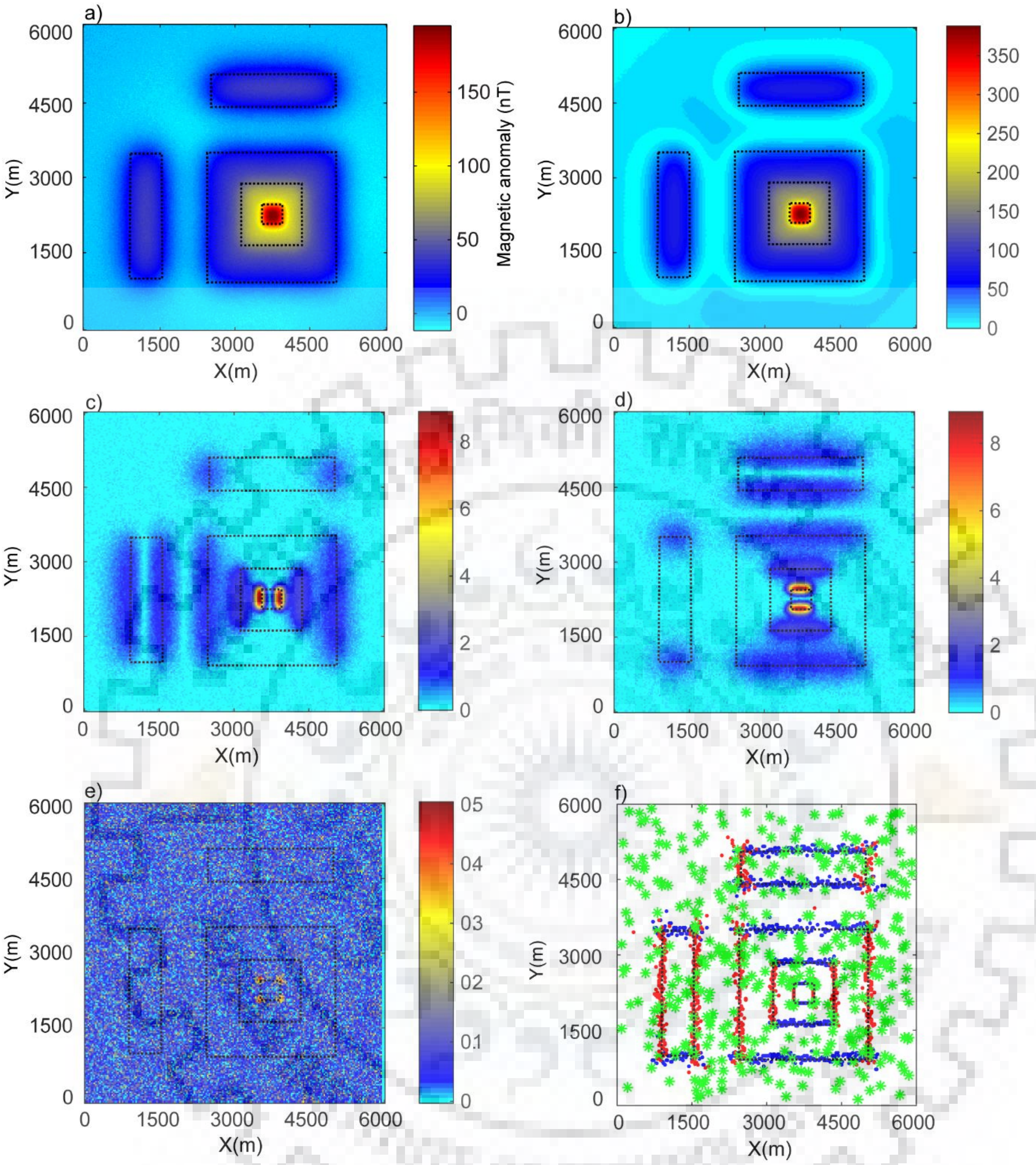

Figure 3.9: a) The total magnetic anomaly with Gaussian noise of one percent of the maximum amplitude, b) wavelet approximation coefficients, c) wavelet horizontal detail coefficients, d) wavelet vertical detail coefficients, e) wavelet diagonal detail coefficients, f) the edge plot.

3.8 BISHOP MODEL

The Bishop model is a 3D basement model for a portion of the volcanic tablelands area situated north of Bishop, California, U.S.A (Williams, 2002). The model is derived from scaling and shifting of the topographic data in depth such that the structures are below the surface with depths of approximately 100–9300 m. The Bishop model has been used in the past to test different source edge detection methods methodologies (Salem et al., 2008; Gerovska et al., 2010; Li X., 2016). Several magnetic field datasets are available corresponding to different models of varying inclination and a total geomagnetic field of 50,000 nT with the original spacing of the data 200 m in both directions. The Bishop 5x data set is used with the geomagnetic inclination of 90° and the base of the magnetic basement layer coinciding with the Moho discontinuity. The grid spacing is increased from 200 m to 400 m to avoid the memory problem of the MATLAB. Figure 3.10 shows the variation of basement depth, magnetic susceptibility values and magnetic anomaly due to the Bishop model. The basement depth variations represent realistic variations in the structural pattern of the sources. The magnetic susceptibility contrast represents four isolated sources, two large offset faults striking along EW direction, an echelon array of smaller-scale fault striking along NS direction. The total magnetic anomaly due to the combination of these sources poses a realistic, complex geological setting.

The WSED method is applied to the total magnetic anomaly (Fig. 3.10c) of the Bishop model and calculates the absolute values of approximation and detail coefficients (Fig. 3.11). The wavelet approximation coefficients show signatures of edges of all prominent sources. The wavelet detail coefficients identify different sources in different directions (x-axis, y-axis and diagonal). The sources can be easily separated between extended and isolated based on signatures in the three wavelet detail coefficients as discussed in the methodology. In the edge plot (Fig. 3.11e) of the Bishop model, the horizontal (blue dots) and vertical (red dots) wavelet detail coefficients identify the source boundary of the EW and NS trending structures. It is worth to note that the diagonal wavelet detail coefficients (green) also confirm these sources and further indicate the presence of two boundaries due to a) extended magnetic susceptibility contrast in EW direction and b) prominent basement structure in EW direction. The prominent signatures in the form of all the three wavelet detail coefficients confirm the presence of four isolated sources. The diagonal coefficients effectively mark the corners of these isolated sources. The clustering of the points in NW of the edge plot represent the signatures of the magnetic sources due to basement depth variations.

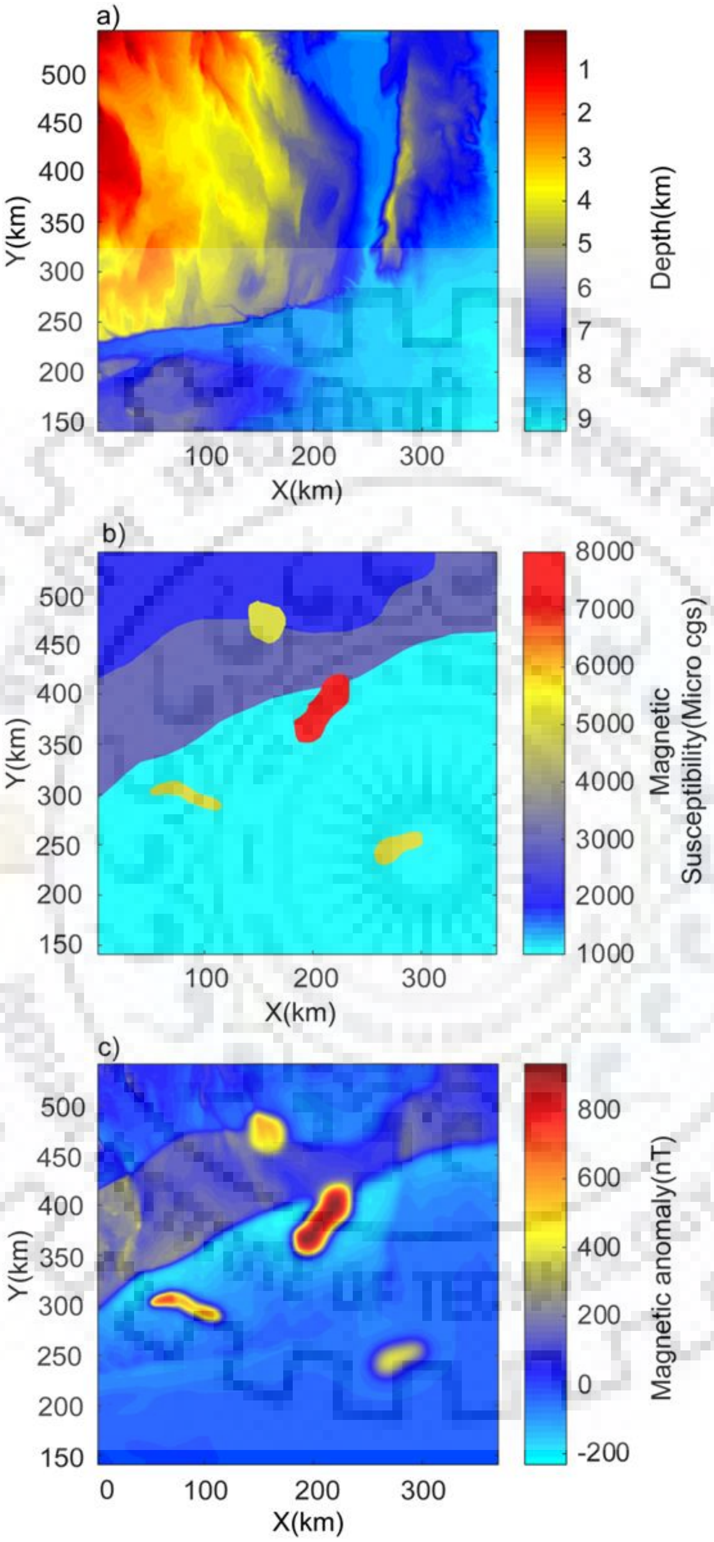

Figure 3.10: Bishop model, a) basement depth, b) basement magnetic susceptibility, c) total magnetic anomaly.

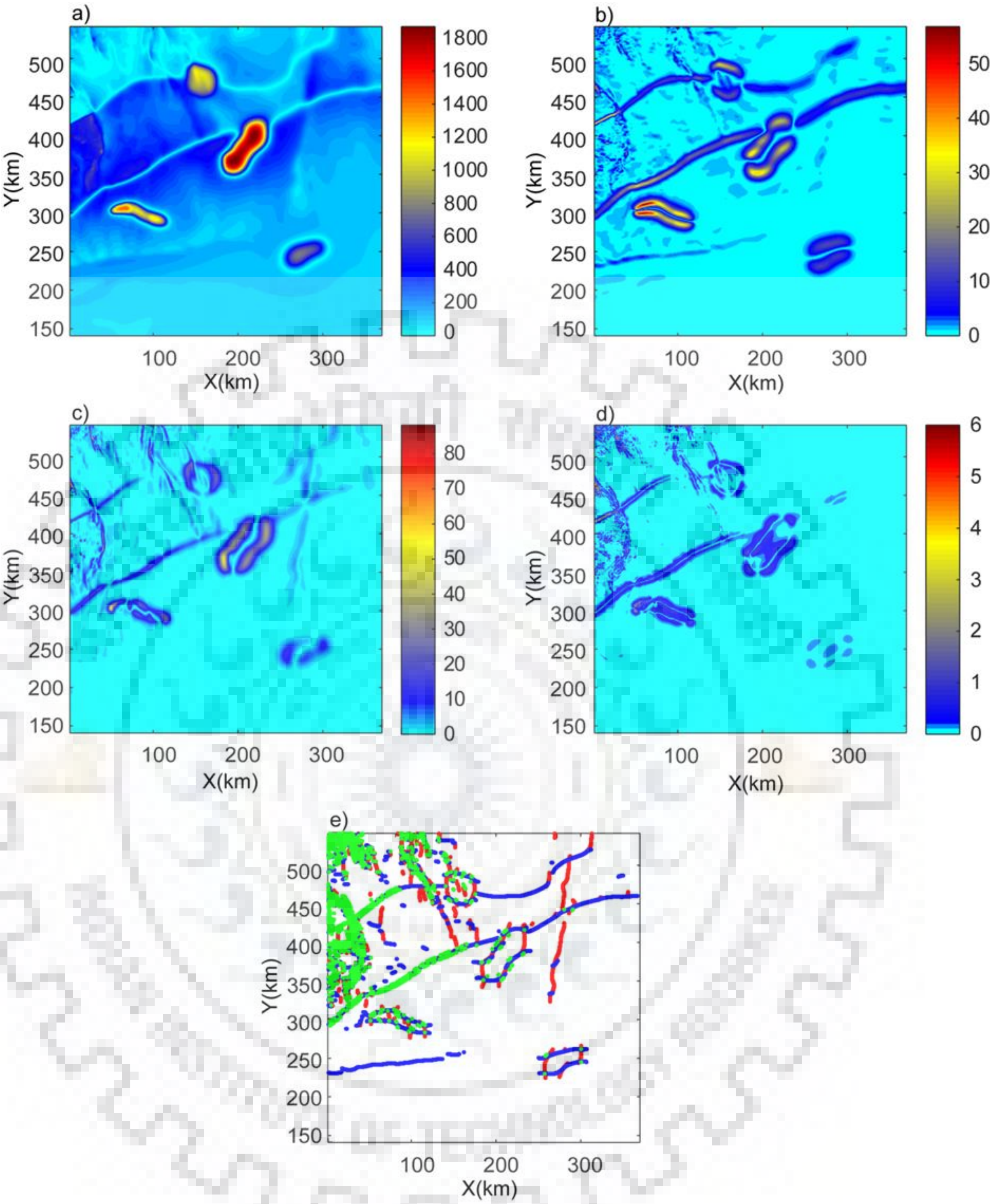

Figure 3.11: a) Wavelet approximation coefficients, b) wavelet horizontal detail coefficients, c) wavelet vertical detail coefficients, d) wavelet diagonal detail coefficients. Note the signatures in different wavelet coefficients corresponding to source boundaries shown by dotted lines. e) The edge plot.

3.9 RESULTS

Wavelet source edge detector method is proposed to identify the source edge boundaries of the potential field data. The wavelet approximation coefficients show signatures of edges of all prominent sources. The wavelet horizontal and vertical detail coefficients identify the edges of the sources in two orthogonal directions independently. The WSED method demarcates the corners of the sources in addition to the edge boundaries, which is a distinctive feature in comparison to other source identification techniques. The edge plot gives comprehensive information on these isolated and extended sources. The method is thoroughly tested on the complex source geometries with different source parameters of prismatic bodies and applied to two real cases. The method is evaluated by comparison with other conventional edge detection methods using synthetic data (Model M2). The WSED method enhances the edges of superimposed sources. The method works in a more prominent way to delineate the edges of magnetic sources of the Bishop model. The wavelet detail coefficients identify the four isolated magnetic sources, two extended sources in EW direction and one NS striking fault structure. The method is further applied to identify the geological boundaries of the filtered Bouguer gravity anomaly of the DFB, which is discussed in chapter 5.

CHAPTER - 4: DEPTH FROM EXTREME POINTS METHOD AND ITS APPLICATION

4.1 INTRODUCTION

In the previous chapter, we have seen the methodology and application of the WSED method in source edge detection. In addition to the edges, the shape and depth of the sources are important parameters which can act as a priori information for constraining the subsurface models and thus, are useful in the interpretation of gravity and magnetic datasets. The scaling methods can be used for source characterization as introduced in chapter 1. The present chapter describes the application of the DEXP method in determination of the source shape and depth. The DEXP method is applied on synthetic gravity and magnetic data due to isolated and extended sources as well as for the realistic case of Bouguer gravity anomaly of the DFB.

The Euler homogeneity relation can be written as (Thompson, 1982):

$$(x-x_0)\partial f/\partial x+(y-y_0)\partial f/\partial y+(z-z_0)\partial f/\partial z=-n(f+b) \tag{4.1}$$

Where f is a homogeneous function and n is the degree of homogeneity. The Euler deconvolution algorithms are based on solving the above equation for the unknown x_0, y_0, z_0, n and b for a set of observations (x, y, z), where (x_0, y_0, z_0) is the position of the source and b is the background effect.

There are two categories to determine the source geometry: a) Monoscale methods, and b) multiscale methods.

a) Monoscale methods are based on solving the Euler differential homogeneity equation with data at a single level of the measurements. In this category, the source depth and shape is estimated by Euler deconvolution algorithm.

b) Multiscale methods such as CWT and DEXP uses the scaling behavior at different altitudes of the datasets.

The CWT method uses Poisson wavelet to derive the structural index and depth of sources. The DEXP method transforms the data using the upward continuation of any order derivative of the anomaly.

4.2 DEPTH FROM EXTREME POINTS METHOD

The depth from extreme points method uses the multiscale properties of the upward continuation field of any derivative order of the potential field data to characterize the potential field sources (Fedi, 2007). The method is useful in deriving the mean depth of the sources using extreme points of the scaled potential field. The method gives information about the shape of the causative sources by calculating the structural index (SI).

The details of the theoretical development and methodology can be seen in Fedi (2007). However, I summarize the methodology briefly here.

The Newtonian potential field for nth order (f_n) can be written in terms of altitude of continuation (z) and depth of source (z_0):

$$f_n = \frac{1}{\left(z - z_0\right)^{n+1}} \tag{4.2}$$

The scaling function (τ_n) depends on the nth vertical derivative of potential field (f) and altitude (z) as:

$$\tau_n = \frac{\partial \log[f_n\left(z\right)]}{\partial \log\left(z\right)}$$

(4.3)

By substituting equation 4.2 in equation 4.3:

$$\tau_n = \frac{\partial \log[f_n\left(z\right)]}{\partial \log\left(z\right)} = -\frac{(n+1)z}{z - z_0} \tag{4.4}$$

At extreme points $z = -z_0$, the scaling function (τ_n) is:

$$\tau_n(z = -z_0) = \frac{\partial \log[f_n\left(z\right)]}{\partial \log\left(z\right)} = -\frac{(n+1)}{2} \tag{4.5}$$

The scaling coefficient (α_n) is given as (Fedi, 2007):

$$\alpha_n = -\tau_n = 0.5(n+1) \tag{4.6}$$

The DEXP transformed scale field is defined as (Fedi, 2007):

$$W_n = z^{\alpha_n} f_n \tag{4.7}$$

The scaling behavior of W_n gives information about source depth. The source parameters, structural index (S_n) and scaling coefficient (α_n), measure the rate of fall of fields and given by:

$$S_n = 2\alpha_n \tag{4.8}$$

The structural index (S_n) is calculated from the intercept of the plot of τ_n versus q from the following equation, which is derived after substituting $z = 1/q$ in the equation 4.4

$$\tau_n(q) = -\frac{(n+1)}{1-z_0 q} \tag{4.9}$$

The structural index (S_n) is estimated by:

$$\tau_n(q \to 0) = -2\alpha_n = -S_n \tag{4.10}$$

For $\tau_1 \quad (n=1)$,

$$\tau_1(z) = -\frac{2z}{z-z_0} \tag{4.11}$$

In the above expression, substituting $z = -z_0$

$$\tau_1(z) = -1 \tag{4.12}$$

The scaling function is a dimensional function of the altitude, which characterizes the scaling behavior of the homogeneous field (Fedi, 2007).

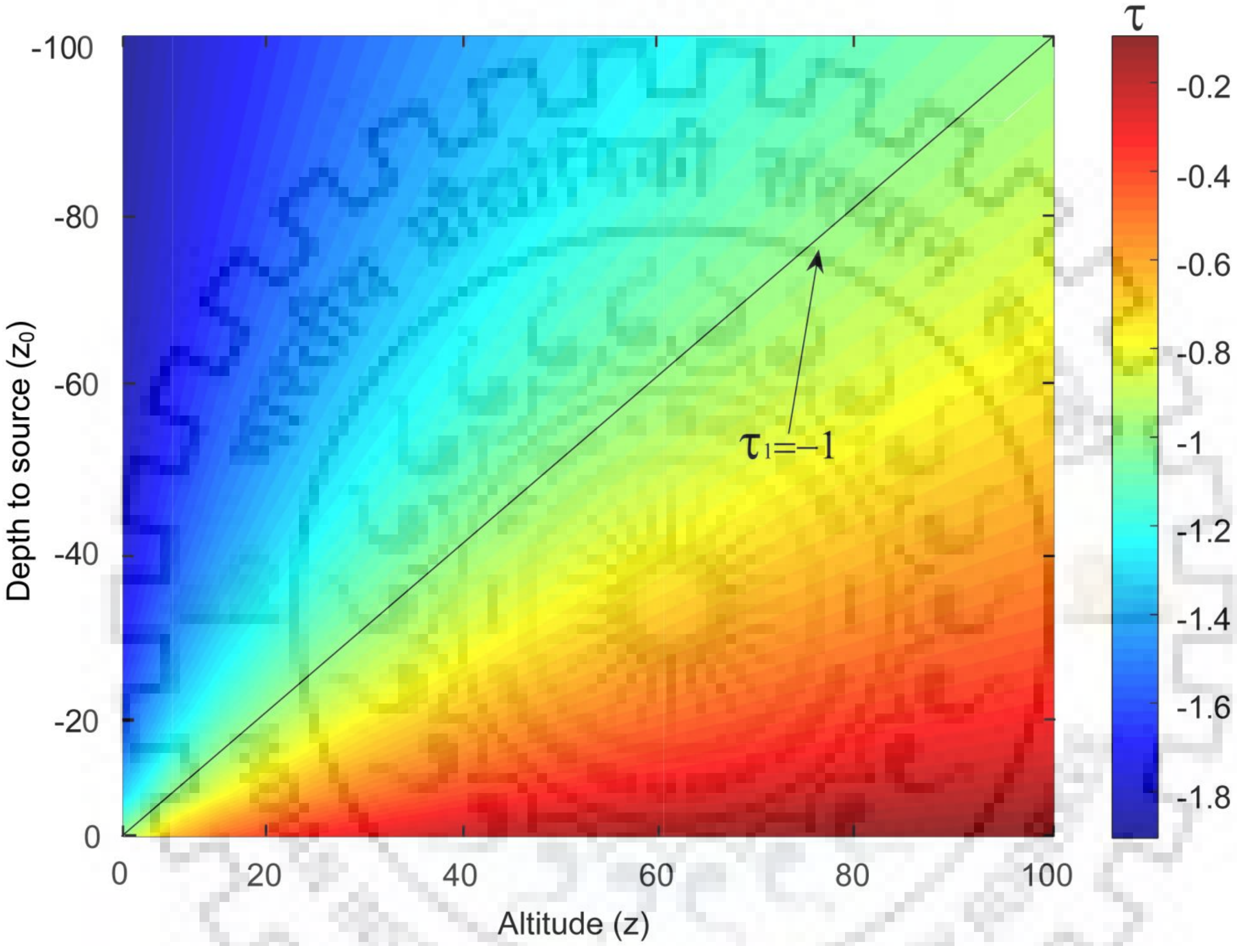

Figure 4.1: The scaling function τ_1 for the potential field (n=1)

The behavior of scaling function $\tau_1(z)$ is shown in figure 4.1. It is drawn as a function of both altitude (z) and depth of the source (z_0), which determines the DEXP transformed scale field at $z = -z_0$ (source depth). From equation 4.9, the plot of τ_n versus $q(1/z)$ determines the intercept along the y-axis. This intercept characterizes the structural index of the source.

I summarize the DEXP methodology in the following steps:

1. I create the 3D data volume of the potential field (f) using upward continuation to get the transformed scaled field (W) using equation 4.7.
2. The extreme points of the transformed scaled field are used in the estimation of the average depth of the sources.
3. The structural index (S_n) is calculated from the intercept of the plot of scaling function (τ_n) versus q using equation 4.9.

The high order DEXP transformation reduces the mutual interference effect of the sources and discriminates shallow and deep sources properly. It further gives useful information about the density contrasts of the sources. The high amplitude of the anomaly corresponding to the positive density contrast sources gives a high amplitude of DEXP transformed field. Similarly, the low amplitude of the anomaly corresponding to the negative density contrast sources gives the low amplitude of DEXP transformed field. The maxima (shown by white points) represents the average depth of the source.

Table 4.1

Sources and their scaling exponent (Fedi, 2007)

Source type	Source	$n=1$ α_n	$n=2$ α_n	$n=3$ α_n	n^{th} order α_n	n=1 S_n	n=2 S_n	n=3 S_n
A	Point mass or dipole, spheres	1	1.5	2	$\alpha_n = 0.5(n+1)$	2	3	4
B	Lines or masses, horizontal and vertical cylinder	0.5	1	1.5	$\alpha_n = 0.5n$	1	2	3
C	Semi-infinite plane, thin dike	0	0.5	1	$\alpha_n = 0.5(n-1)$ $n \geq 1$	0	1	2
D	Semi-infinite contact	-0.5	0	0.5	$\alpha_n = 0.5(n-2)$ $n \geq 2$	-1	0	1

Note: α_n and S_n are the scaling exponent and structural index respectively (see equation 4.8)

4.3 SYNTHETIC CASES

The DEXP method is tested on different synthetic gravity data. Although different source parameters are tested, three cases are presented here for clarity.

4.3.1 Sphere

The figure 4.2a illustrates the synthetically generated gravity anomaly due to a uniform sphere with density contrast 200 kg/m^3, radius 5 km and center at (125, 125, 15) km. The spatial interval is 1 km in both horizontal directions. The DEXP transformed scale field is calculated on upward continued gravity data upto 25 km altitude at an interval of 1 km. The figure 4.2b shows the DEXP transformed scaled field (W_1) with respect to z_0 axis (i.e. along the vertical axis related to the depth of the source) with an extreme point at $z = -z_0$. The extreme point (white mark) occurs at a depth 14.2 km, which gives an average depth of the sphere. I have calculated the structural index of the source, which is estimated by the plot of scaling function (τ) versus $q(1/z)$ (Fig. 4.2c). The intercept along y-axis occurs at 1.92 (~1.9), which represents the structural index of the sphere.

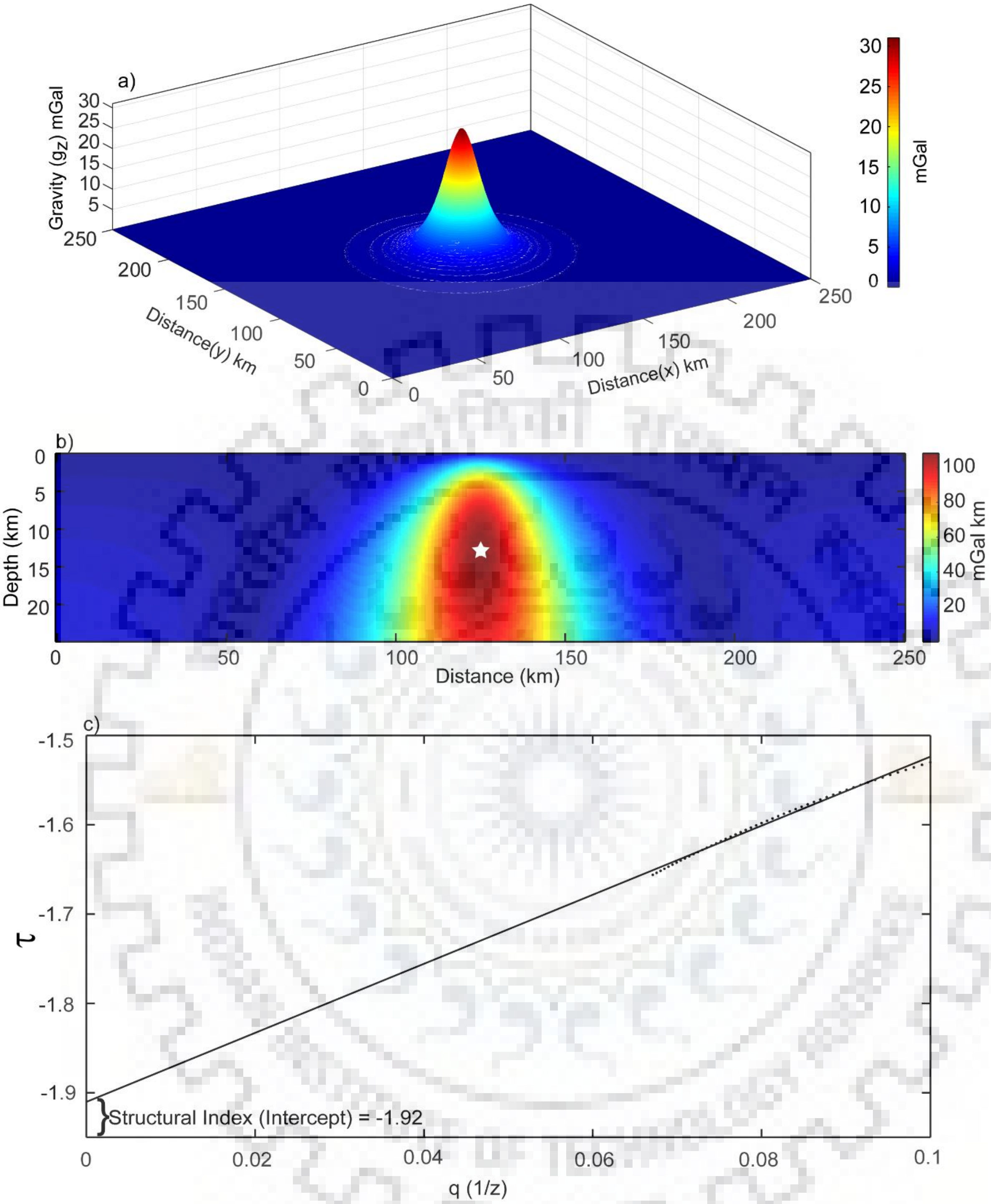

Figure 4.2: a) Synthetic gravity anomaly due to a uniform sphere, b) the DEXP transformed scale field, c) the plot of the scaling function (τ) versus q.

4.3.2 Elongated prism

The synthetic gravity anomaly due to an elongated prism is shown in figure 4.3a. The assumed dimensions of the prism are (10×20×11 km^3) with a 10 km depth to the top and density contrast 100 kg/m^3. The horizontal prism dimensions are (10×20 km^2) and the profile is perpendicular to the longest side. The spatial interval is 1 km in both horizontal directions. The DEXP transformed scale field is calculated on upward continued gravity data upto 25 km altitude at an interval of 1km. The scaled field (W_1) with an extreme point at $z = -z_0$ is shown in figure 4.3b. It has an extreme point (white mark) at depth 9.8 km, which gives an average depth of the elongated prism. Figure 4.3c shows the plot of scaling function (τ) versus $q(1/z)$ .The intercept occurs at 1.05 (~1.1), which represents the structural index of the elongated prism.

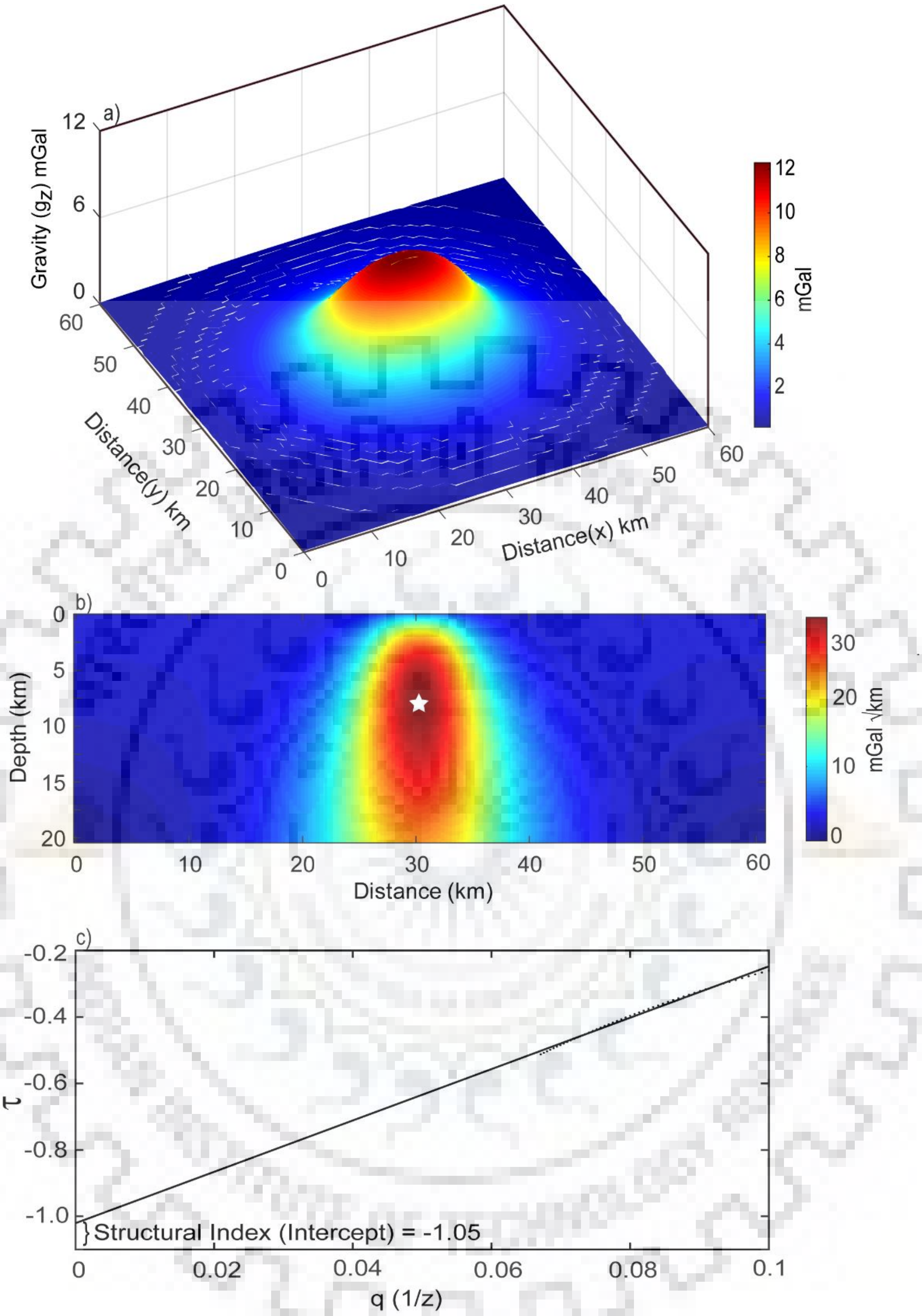

Figure 4.3: a) Synthetic gravity anomaly due to an elongated prism, b) the DEXP transformed scale field, c) the plot of the scaling function (τ) versus q.

4.3.3 Infinite horizontal cylinder

The synthetic gravity anomaly due to an infinite horizontal cylinder is shown in figure 4.4a. The cylinder has assumed a depth of 8 km, density contrast 200 kg/m^3 and centered at position (0, 0, 8) km. The spatial interval is 1 km in both horizontal directions. The DEXP transformed scale field is calculated on upward continued gravity data upto 40 km altitude at an interval of 1 km. The scaled field (W_{g1}) with an extreme point at $z = -z_0$ is shown in figure 4.4b. It has an extreme point (white mark) at depth 8.1 km, which gives an average depth of the horizontal cylinder. Figure 4.4c shows the plot of scaling function (τ) versus $q(1/z)$. The intercept along y-axis occurs at 1.03 (~ 1.0), which represents the source as a horizontal cylinder.

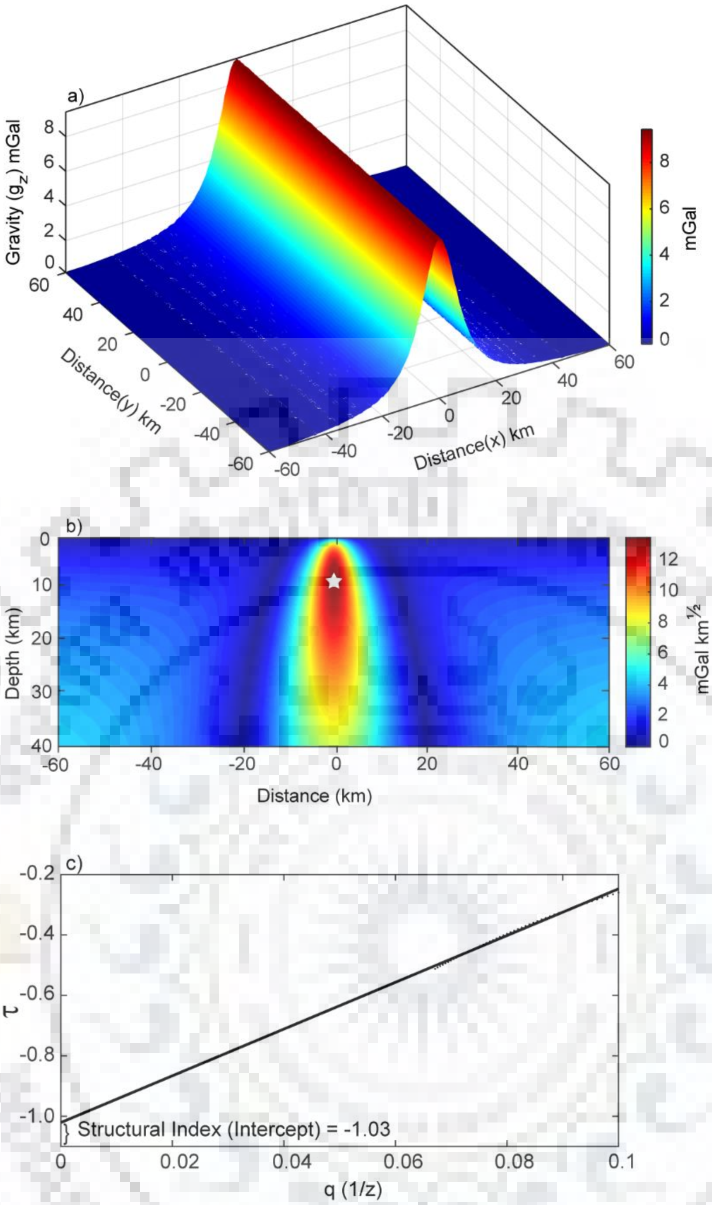

Figure 4.4: a) Synthetic gravity anomaly due to an infinite horizontal cylinder, b) the DEXP transformed scale field, c) the plot of the scaling function (τ) versus q.

4.4 RESULTS

The DEXP method has shown the following advantages:

a) The DEXP method identifies the mean depth, structural index and density/magnetic susceptibility contrast of the isolated and extended sources. The information about the contrast in geophysical properties can be useful for real cases.
b) The DEXP method is tested for synthetic cases (Sphere, elongated prism and horizontal cylinder) of different source parameter combinations. The testing shows the effectiveness of the methodology.

The application of the DEXP method to the Bouguer gravity anomaly of the DFB region is discussed in chapter 5.

CHAPTER -5: GRAVITY DATA ANALYSIS AND MODELING OF DELHI FOLD BELT

5.1 INTRODUCTION

In previous chapters, the theory of the WSED and DEXP method is introduced for source edges detection and characterization. In this chapter, different techniques are used to constrain the crustal structure. The WSED method is used to delineate the geological boundaries of the study region. The DEXP method is applied to the Bouguer gravity anomaly of three subregions of the DFB region to understand the source structures and its extensions. Parker (1973) introduced the 3D structural inversion for estimation of the lateral depth variations of any interface using gravity anomaly. The lateral depth variations of the Moho are derived here using the 3D structural inversion. The Bouguer gravity anomaly projected over the geology and tectonic map of the region is shown in figure 5.1. The SW-NE trending gravity high attains the positive over the Delhi fold belt while the flanking lows occur over the Malani igneous suite, Marwar basin and Hindoli group of the region. The Bouguer gravity anomaly is modeled along two profiles AA' and BB' to understand the depth, shape, and extension of the DFB and adjoining litho-tectonic units. The gravity modeling is carried out iteratively incorporating the constraints from the results of different techniques (Spectral analysis, 3D structural inversion, WSED, DEXP) which helped in optimizing the model. I propose a crustal model from the gravity data and previous geological and geophysical information to address the northward extension of the DFB and its implications in the crustal configuration at the leading edge of the Indian Peninsula.

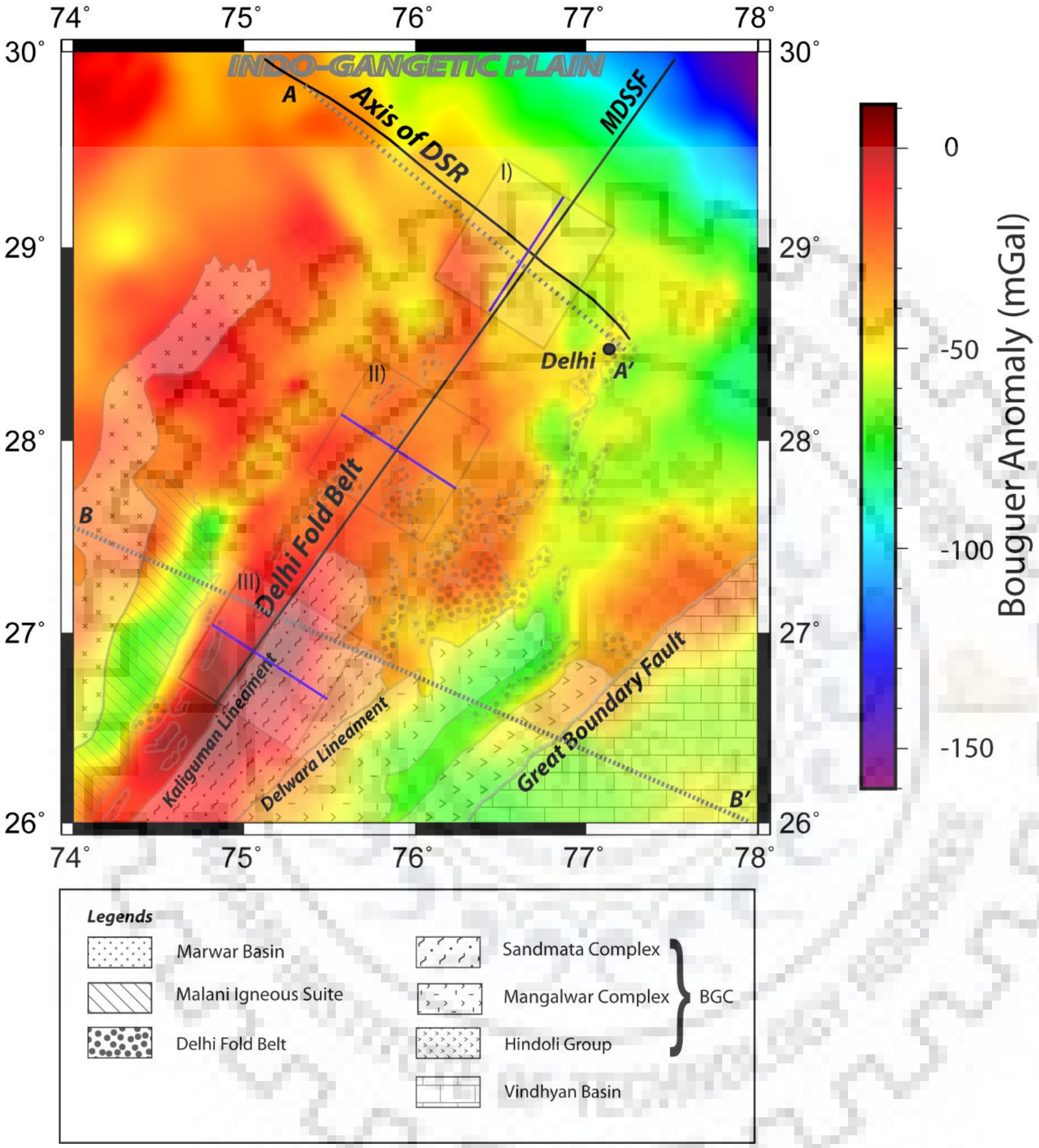

Figure 5.1: Bouguer gravity anomaly projected over the geological and tectonic map of the study region (after Roy and Jakhar, 2002). The subregions marked by boxes (I, II, III) are used in the DEXP analysis and results (Fig. 5.9) are along the shown central blue line. The two profiles AA' and BB' are used in gravity modeling.

5.2 GRAVITY DATA ANALYSIS

The gravity data is analyzed in spectral-domain using: a) power spectrum method and b) spectral filtering. These methods are useful in constraining a priori depth information about the layered interfaces and separation of the gravity anomalies due to sources at different depths.

5.2.1 Power spectrum and filtering of the gravity data

The transformation of potential field data to some auxiliary space (such as Fourier domain) gives information about the causative sources. Power spectrum analysis (Bhattacharyya, 1966; Dimri, 1992; Blakely, 1995) estimates the average depth of interfaces considering the log of power of the Bouguer gravity spectrum as a function of wavenumber/frequency assuming a random and uniform distribution of sources (Spector and Grant, 1970). The spectrum of gravity anomaly due to a layered source is separated into multiple segments in the frequency domain that can be interpreted in terms of the mean depth of interfaces.

The Power spectrum $P(k)$ is related to the mean depth (d) of interfaces as (Spector and Grant, 1970):

$$\ln P(k) = -2kd \tag{5.1}$$

Where k is the wavenumber. In the case of 2D datasets, the radially averaged power spectrum versus wavenumber k (where, $k^2 = k_x^2 + k_y^2$, k_x and k_y are wavenumbers in x and y directions) is used. The layered model shows linear segments in the power spectrum and the average depth of the interfaces can be calculated from the slope of the segments. The radially averaged power spectrum of the Bouguer gravity anomaly is calculated, which shows three linear segments (Fig. 5.2). The average depth of three interfaces are estimated as 35.3 km, 9.3 km and 2.9 km. These depth corresponds to the Moho, upper-lower crust boundary and basement respectively.

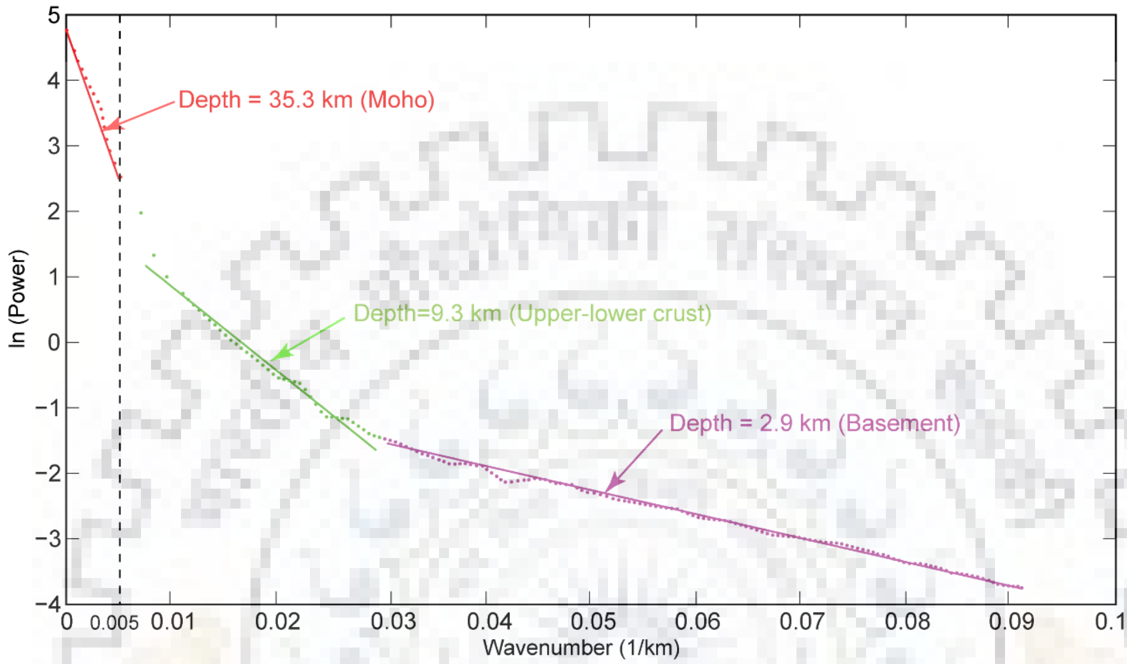

Figure 5.2: Radially averaged power spectrum of the gravity anomaly. Different linear segments give an average depth of the layered interfaces.

I separate the Bouguer gravity anomalies based on power spectrum characteristics using spectral filtering. I apply a low pass filter with a cut off wavelength of 200 km (equivalent to wavenumber 0.005 km^{-1}) based on the maximum wavenumber of the Moho segment in the power spectrum (Fig. 5.2). The filtering gives the long-wavelength filtered anomaly (LWFA; Fig. 5.3) and short-wavelength filtered anomaly (SWFA; Fig. 5.4). The LWSA shows a prominent SW-NE trending gravity high signature. This signature can be due to the large wavelength structures possible at Moho depth below the DFB and Sandmata complex (Fig. 5.3). This trend abruptly terminates near Delhi and deflect to follow the NW high gravity anomaly pattern of the Delhi-Sargodha ridge axis.

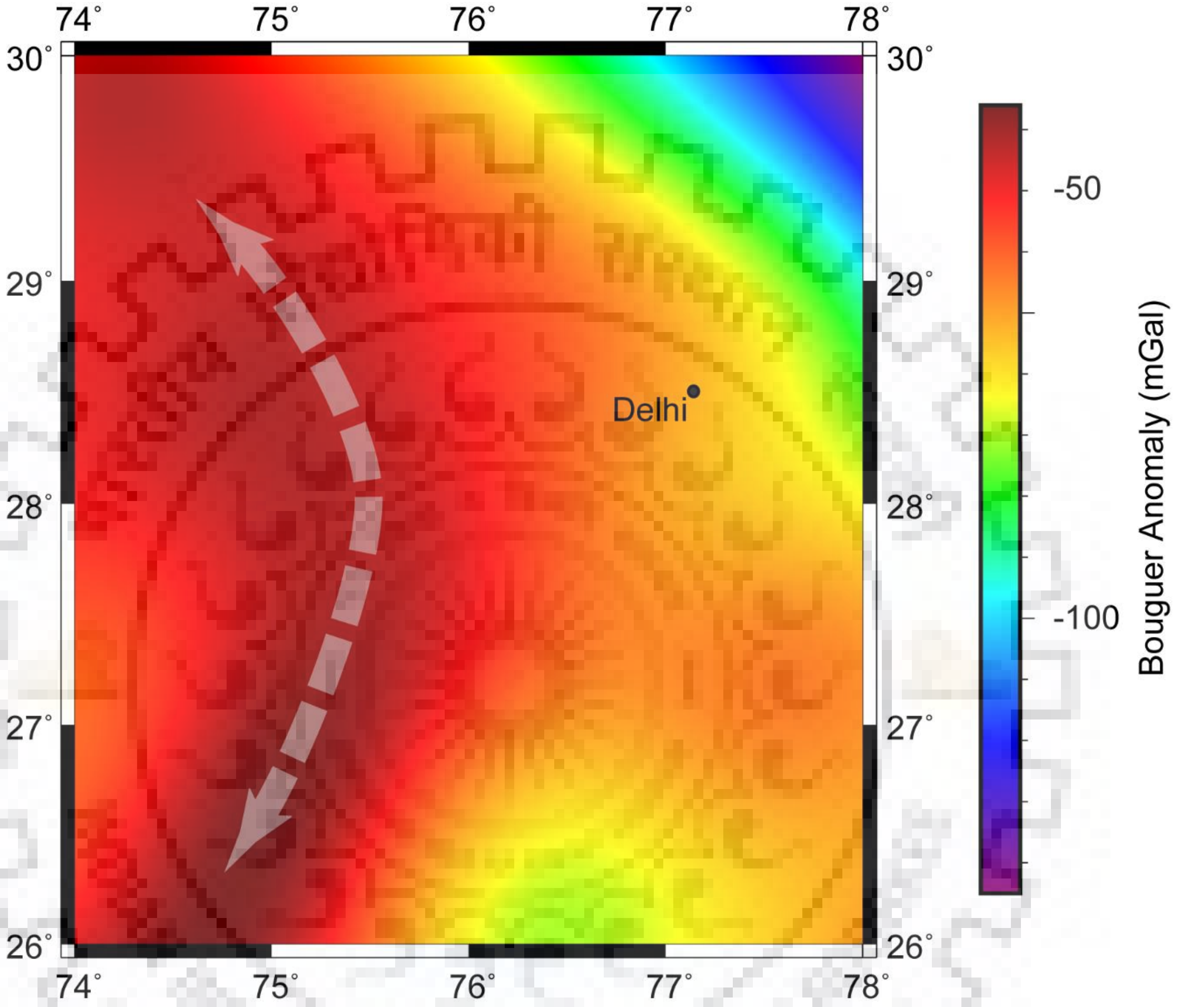

Figure 5.3: Long wavelength filtered gravity anomaly (> 200 km) of the study region. The arrow indicates deflection of prominent long wavelength anomaly from SW-NE to NW-SE direction parallel to Delhi-Sargodha ridge axis.

The SWFA has a strong negative anomaly corresponding to the low-density MIS and positive anomaly due to the high-density DFB and Sandmata complex above the Moho (Fig. 5.4). The SW-NE trend of positive anomaly smears towards the north and terminates near Delhi. There is a feeble signature of bending of the pattern in a SE-NW direction parallel to the DSR axis.

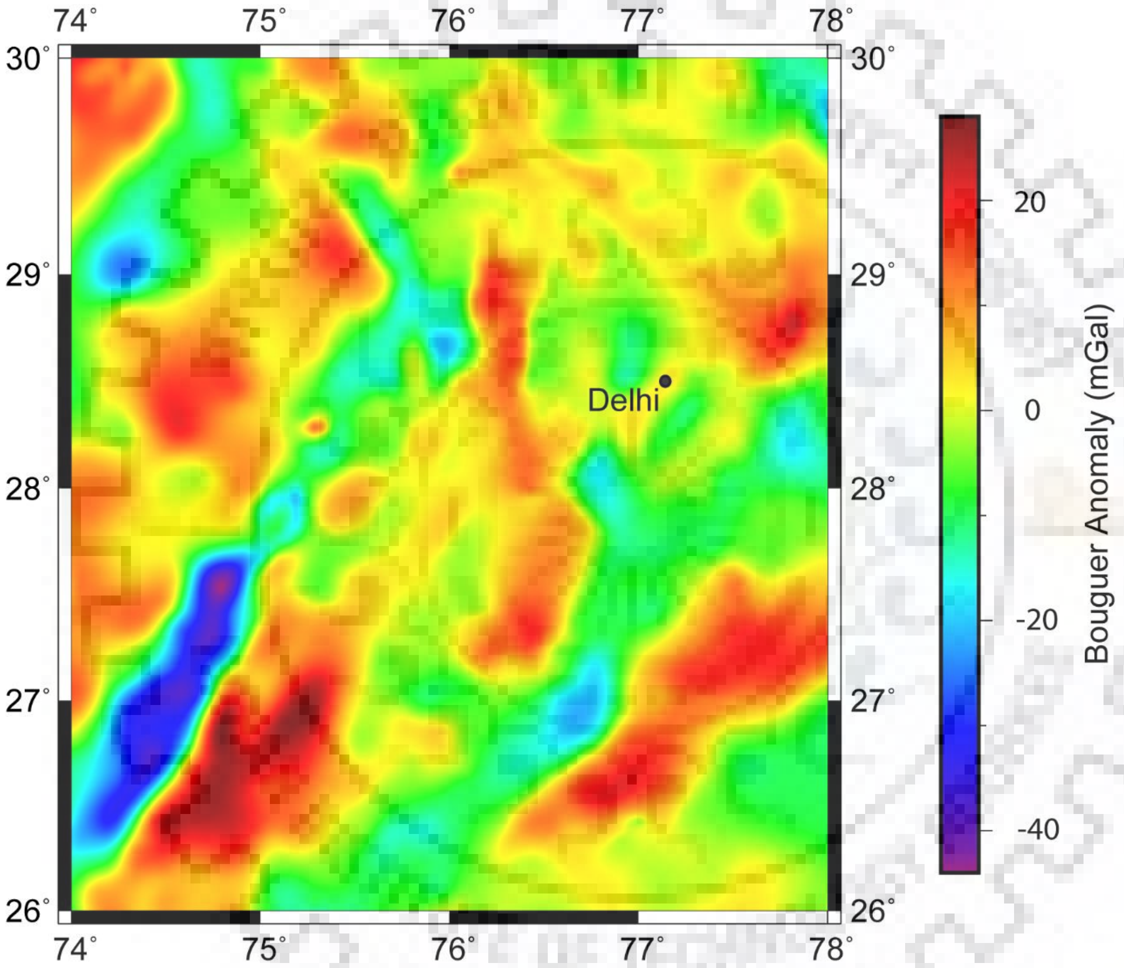

Figure 5.4: Short-wavelength filtered gravity anomaly (< 200 km) of the study region.

5.2.2 Gravity inversion and modeling

The inversion and forward modeling are essential steps to constrain the subsurface structures and their density variations. These structures occur in the form of both shallow and deep sources. I have done the 2D gravity modeling of the profiles, which is appropriate for complex tectonic structures as present study region. The study region has been tectonically active in the geological past. The gravity model correlates with some tectonic episode of the DFB and the surrounding region and its extension towards the north. The gravity inversion and modeling are carried out to derive density variations and geometry of subsurface structures incorporating information from published geological and geophysical studies in the region. The forward modeling is carried out along two profiles AA' and BB' (Fig. 5.1) to understand the extension of the subsurface structures.

I summarize the steps used for gravity inversion and modeling:

1) Inversion of the Moho interface using 3D structural inversion based on Parker algorithm.

2) A priori depth values in the models are based on the mean depth of different interfaces calculated by power spectrum analysis of the gravity data (Fig. 5.2), subsurface geometries from the past DSS study (Tewari et al., 1997), geological formations edge boundaries from WSED method, source information from the DEXP method and the Moho depth from the previous step.

3) A priori density values used in the modeling of different formations are based on the average value of rock types, velocity to density conversion using Nafe-Drake equation and estimates of previous studies (Reddy and Ramakrishna, 1988; Ramakrishnan and Vaidyanadhan, 2010).

4) Blockwise density inversion to invert a priori density values. Table 5.1 shows that the density values are a priori and assigned after inversion.

5) Iterative modeling of the gravity anomaly for a better fit.

These steps are further elaborated in the subsequent sections.

5.2.2.1 3D structural inversion:

Mapping of the 3D variation of the Moho is an important task from the gravity anomaly in imaging the subsurface structure. In this case, we should invert the filtered gravity anomaly in terms of the geometry of the interface. Several authors have presented different algorithm to compute the geometry of density interface related to the known gravity anomaly (Cordell and Henderson, 1968; Dyrelius and Vogel 1972; Bhaskara Rao and Rameshbabu, 1991). Some other algorithm (Oldenburg, 1974) is based on the rearrangement of the forward algorithm of Parker (1973). The Parker algorithm is based on the Fourier transform of the powers of the surface, causing the anomaly. The Parker-Oldenburg algorithm is used by many others to invert the filtered anomaly (Salem et al., 2013; Pedrera et al., 2017). Salem et al., (2013) inverted the regional gravity grid to map the depth of the Moho across the Red sea area and used in modeling of sedimentary thickness. Pedrera et al., (2017) constrained the geometry of high-density body located within the crust using 3D gravity inversion. I have done the 3D gravity structural inversion to study the effect of the Moho on the LWFA data using GMSYS-3D in Oasis Montaj. The Moho depth further helps in imaging of the subsurface structures along the profile AA' and BB' in the forward modeling.

Parker (1973) showed how a series of Fourier transforms can be used to compute the gravity anomaly due to uneven, non-uniform layer. The expression is defined as:

$$F[\Delta g] = -2\pi G\rho \exp(-kz_0)\sum_{n=1}^{\infty}\frac{k^{n-1}}{n!}F[h^n(x)] \tag{5.2}$$

Where $F[\Delta g]$ is the Fourier transform of the gravity anomaly.

k is the wave number.

ρ is the density across the interface.

G is the gravitational constant.

$h(x)$ is depth to the interface (positive downward).

z_0 is the mean depth of a horizontal interface.

Oldenburg (1974) rearranged the above equation to compute the depth to the undulating interface form the gravity anomaly profile by an iterative process. The equation is given as:

$$F[h(x)] = -\frac{F[\Delta g(x)]\exp(-kz_0)}{2\pi G\rho} - \sum_{n=2}^{\infty}\frac{k^{n-1}}{n!}F[h^n(x)] \tag{5.3}$$

The above expression 5.3 determines the topography of the interface density with an iterative inversion procedure. The process is convergent if $z_0 > 0$.

The 3D structural inversion is performed on the LWFA (Fig. 5.3) to derive the 3D geometry of the Moho interface. The following steps are used to calculate the inverted Moho depth:

1) I assumed a two-layered depth model with Moho interface at a priori constant depth of 40 km, which is based on results from the DSS profile across the DFB (Tewari et al., 1997) and receiver function study (Rai et al., 2006). The bottom boundary of the model is kept at 70 km. The densities are considered as 2670 and 3430 kg/m^3 for the two layers.

2) The LWFA is inverted to derive the optimized depth variation of the Moho interface by minimizing the gravity error (misfit).

3) The algorithm reached to convergence in 25 iterations.

The calculated anomaly is shown in figure 5.5 which has the same pattern and anomaly values as that of observed LWFA.

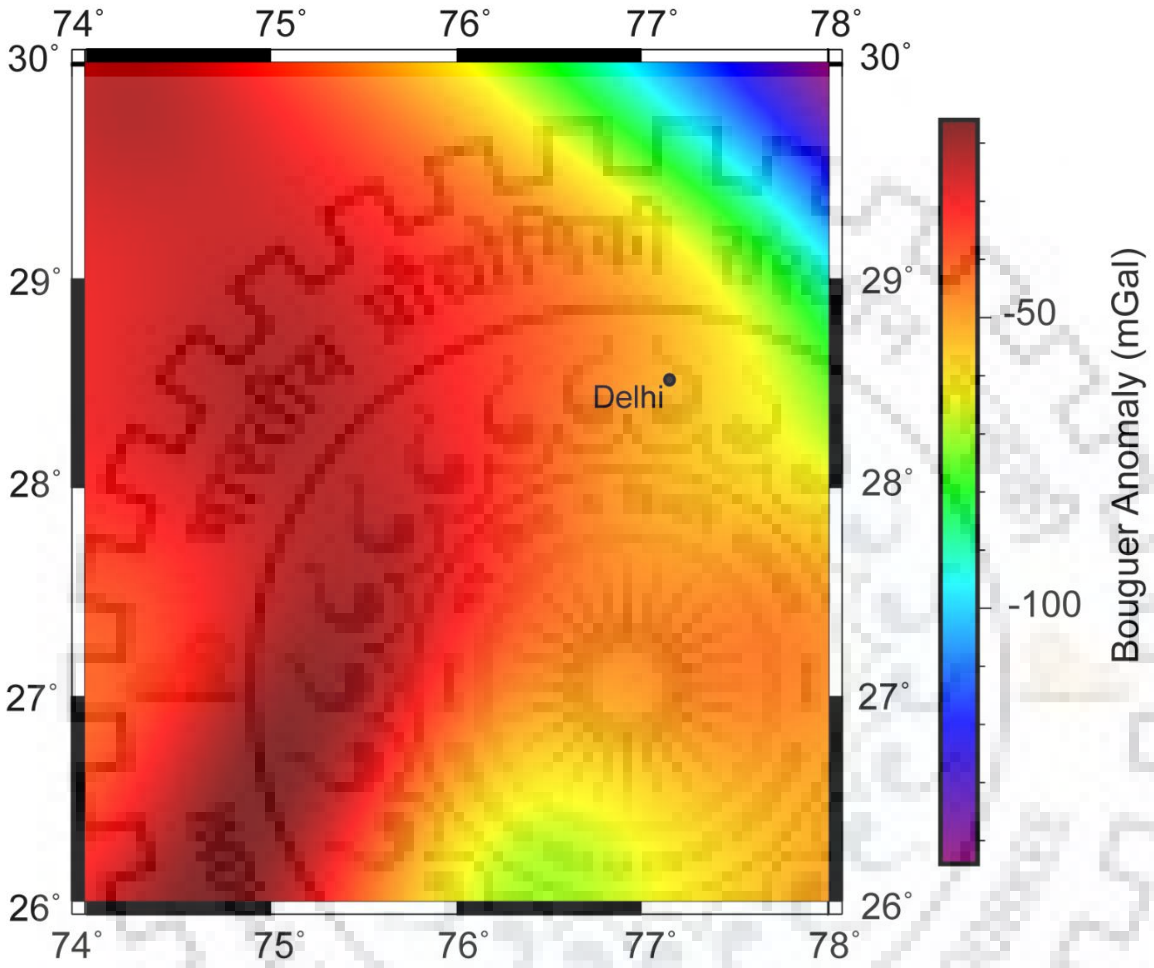

Figure 5.5: The calculated Bouguer gravity anomaly due to Moho density interface in the 3D gravity structural inversion.

The difference between observed and calculated gravity is called “gravity error” which is shown in figure 5.6. The low values of gravity error (between -0.2 to +0.15 mGal) indicate the effectiveness of the applied inversion.

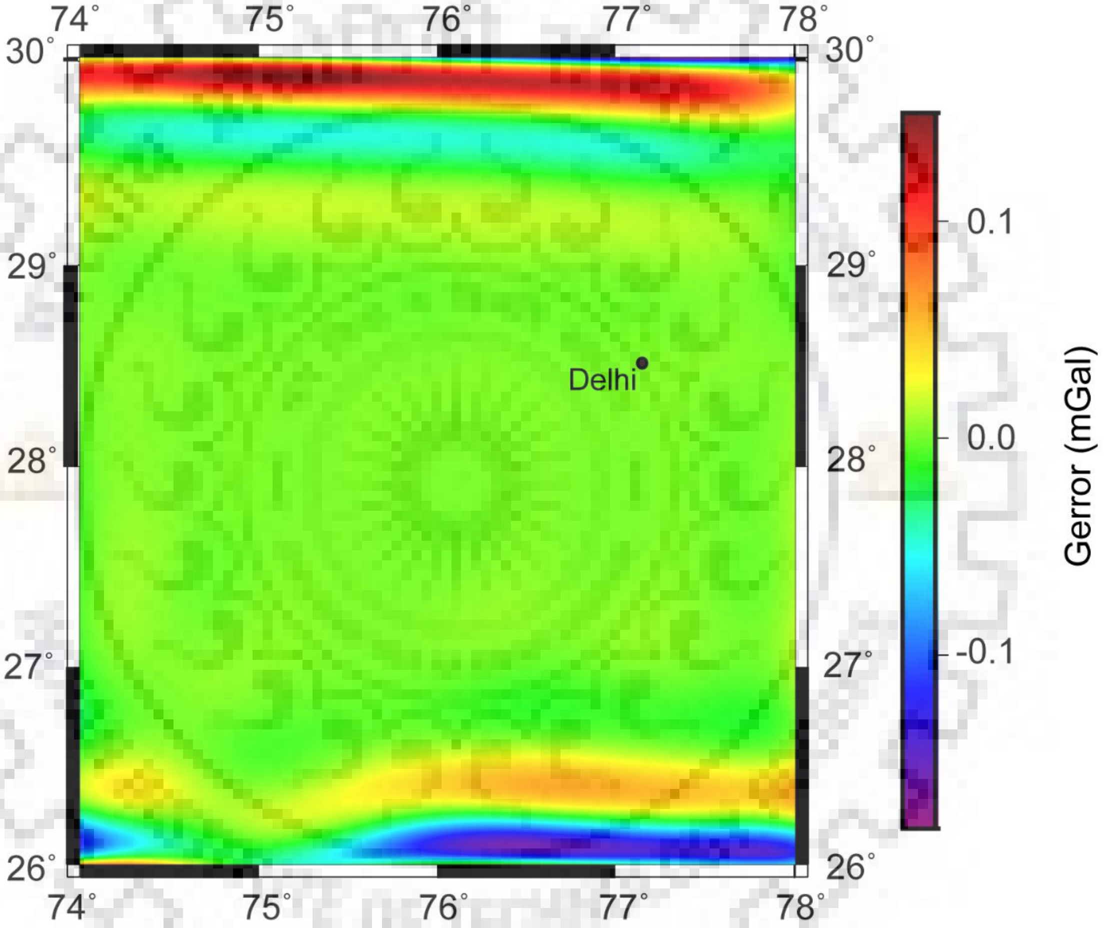

Figure 5.6: The gravity error derived from the 3D gravity structural inversion.

The inverted depth values of the Moho vary from 39 to 46 km (Fig. 5.7). The depth variation of the inverted Moho surface derived from the 3D structural inversion shows a prominent relief feature in the form of ~ 2 km upwarp beneath the DFB. This perturbation in the Moho does not continue northeastward towards the Indo-Gangetic plain but shows widening and a clear northwestward deflection towards the Delhi-Sargodha ridge. The Moho progressively steepens beyond the Delhi with general WNW-ESE strike trend. The Moho depth variations derived from 3D structural inversion are further used in 2D gravity modeling.

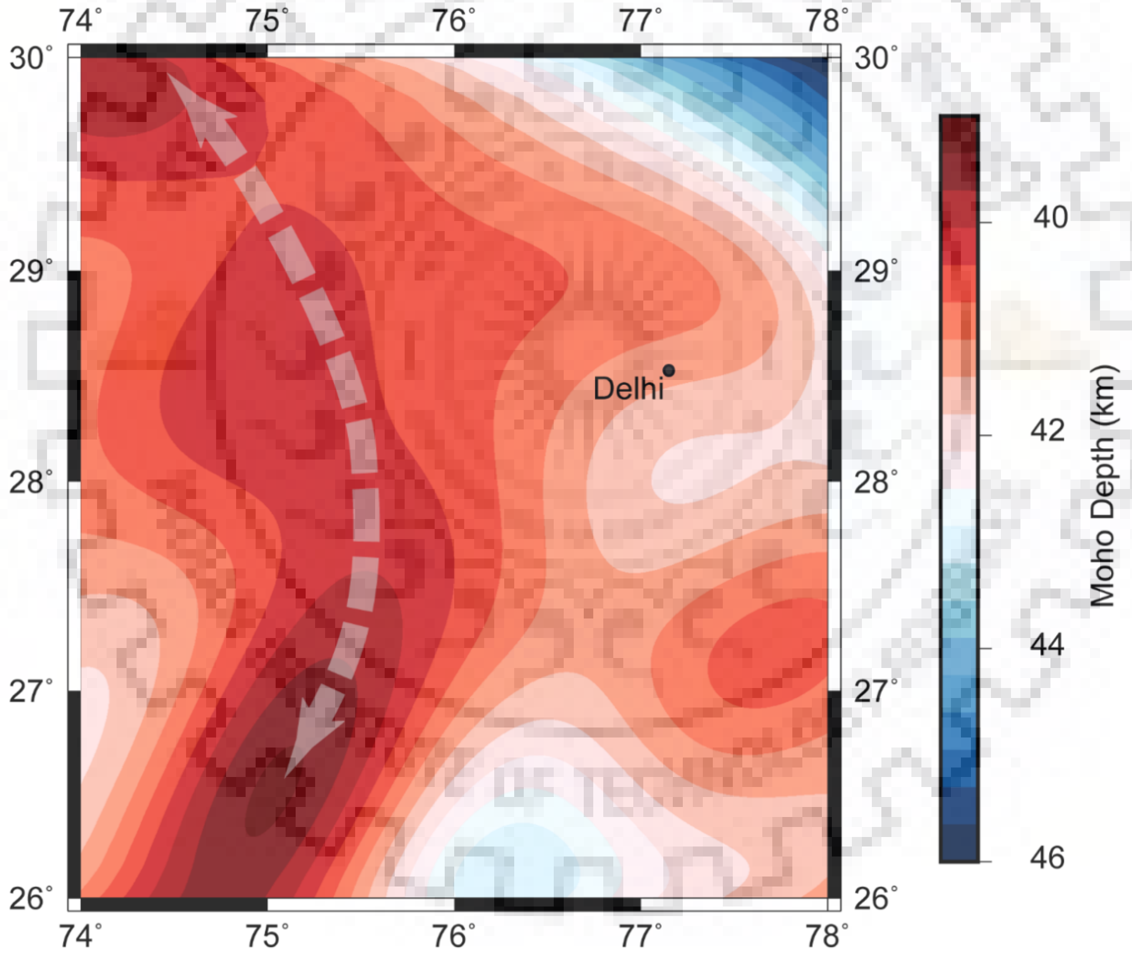

Figure 5.7: The depth variation of the Moho interface derived from 3D inversion of the low pass filtered Bouguer gravity anomaly (> 200 km).

5.3 APPLICATION OF THE WSED METHOD

In chapter 3, I propose the WSED methodology, which identifies the source edge boundary of the potential field data. The wavelet approximation and detail coefficients are calculated for the SWFA (Fig. 5.8a, b, c, d). These coefficients show prominent signatures along the geological boundaries. The wavelet approximation coefficients give edge information of the geological boundaries in a comprehensive manner (Fig. 5.8a). The wavelet detail coefficients identify geological formation boundaries in different directions (x-axis, y-axis and diagonal). The wavelet horizontal detail coefficients show high amplitude corresponding to high spatial frequencies in the y-axis (Fig. 5.8b). The wavelet vertical detail coefficients show high amplitude corresponding to high spatial frequencies in the x-axis (Fig. 5.8c). The wavelet diagonal detail coefficients show high amplitude at the vertices of both directions (Fig. 5.8d). The calculated edge plot of the SWFA shows the edges corresponding to the boundaries of extended sources from SW to NE direction (Fig. 5.8e). These signatures are the boundary between Malani igneous suite and Delhi fold belt, the Kaliguman lineament, the Delwara lineament, and the Great boundary fault respectively from west to east in the edge plot map. The prominent diagonal coefficients in some of the boundaries (DSR edges) indicate that the edge behaves in a 2D manner, as observed in the Bishop model. The details of interpreted boundaries are presented in table 5.1. The identified geological formation boundaries are further used to constrain the structures in gravity modeling.

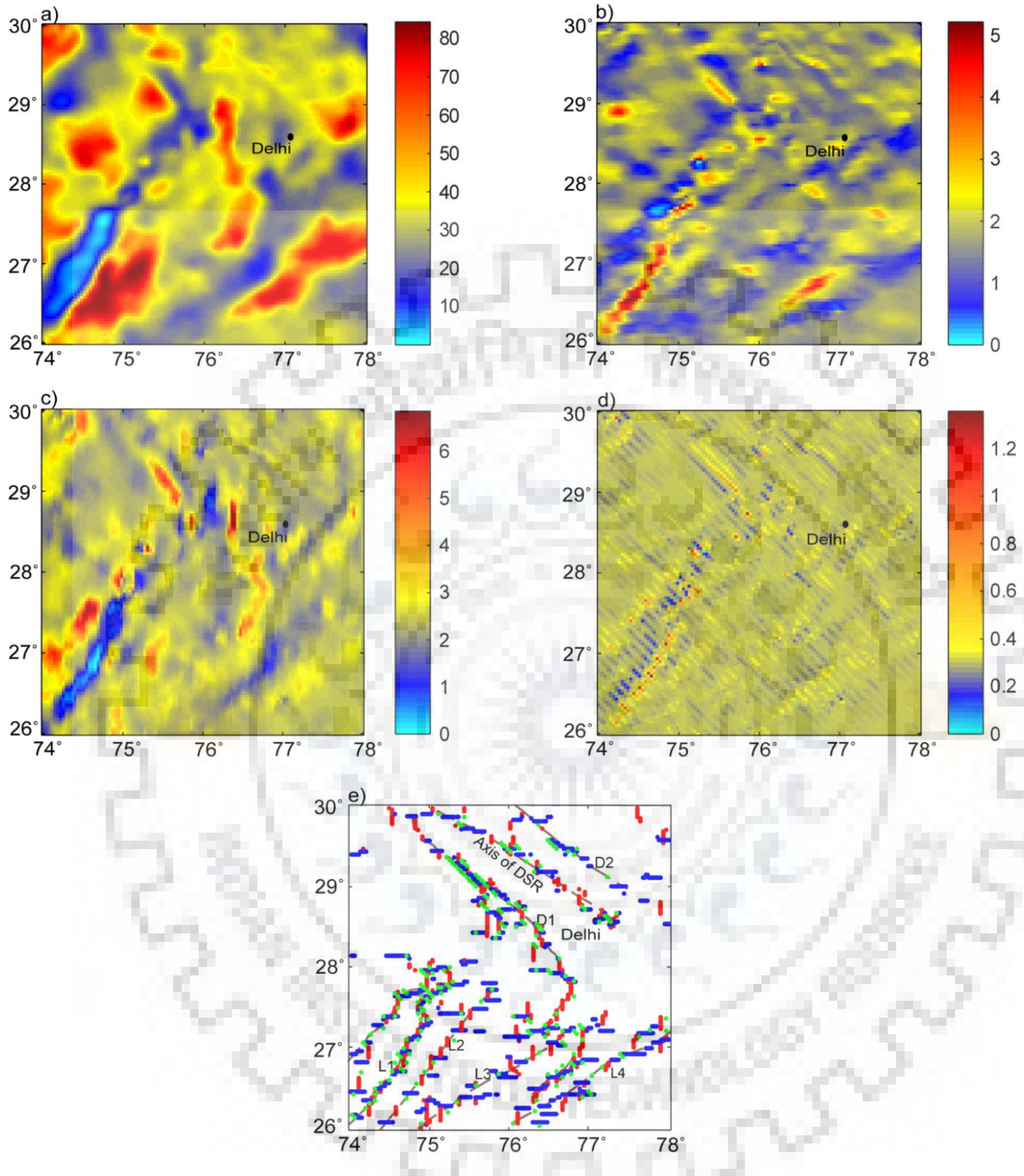

Figure 5.8: a) Wavelet approximation coefficients, b) wavelet horizontal detail coefficients, c) wavelet vertical detail coefficients, d) wavelet diagonal detail coefficients. Note the signatures in different wavelet coefficients corresponding to source boundaries shown by dotted lines. e) The edge plot.

Table 5.1

Interpreted geological formation boundaries using WSED method

S. No.	Identified boundary using WSED method	Interpreted geological boundary
1	L1	Between MIS and DFB boundary
2	L2	Kaliguman lineament
3	L3	Delwara lineament
4	L4	GBF
5	D1, D2	Edges of the DSR

5.4 APPLICATION OF THE DEPTH FROM EXTREME POINTS (DEXP) METHOD

The DEXP method is applied to three subregions (I, II and III) to derive source information. The subregions are considered perpendicular to the strike direction of the DSR (I), DFB and Sandmata complex (II, III) for the DEXP analysis (Fig. 5.1). The DEXP transformed scaled potential field is analyzed at different derivative orders and finally selected the results for n = 3 (second vertical derivative). The higher-order derivative reduces the mutual interference effect of both shallow and deep sources. The scaled field is calculated on upward continued data upto 40 km altitude at an interval of 1 km. The results of the DEXP analysis are:

a) Subregion-I: The DEXP transformed field shows two maxima points that occur at 8 km and 4 km (marked by white points in fig. 5.9a). The high positive contrasts around these points indicate the presence of two high-density sources.

b) Subregion-II: The DEXP transformed field shows one maxima points that occur at 29 km (marked by white points in fig. 5.9b). The high positive contrasts around the point indicate the presence of one high-density source.

c) Subregion-III: The DEXP transformed field shows one maxima points that occur at 31km (marked by white points in fig. 5.9c). The high positive contrasts around the point indicate the presence of one high-density source.

The structural index is calculated (equation 4.9, chapter 3) to derive the shape of the sources for three subregions (Fig. 5.9d, e, f). The calculated structural indices of all the sources of three subregions are equivalent to the class B of S3 = 3 sources (Table 3.1; Fedi 2007), which represents the shape of sources as an infinite horizontal cylinder.

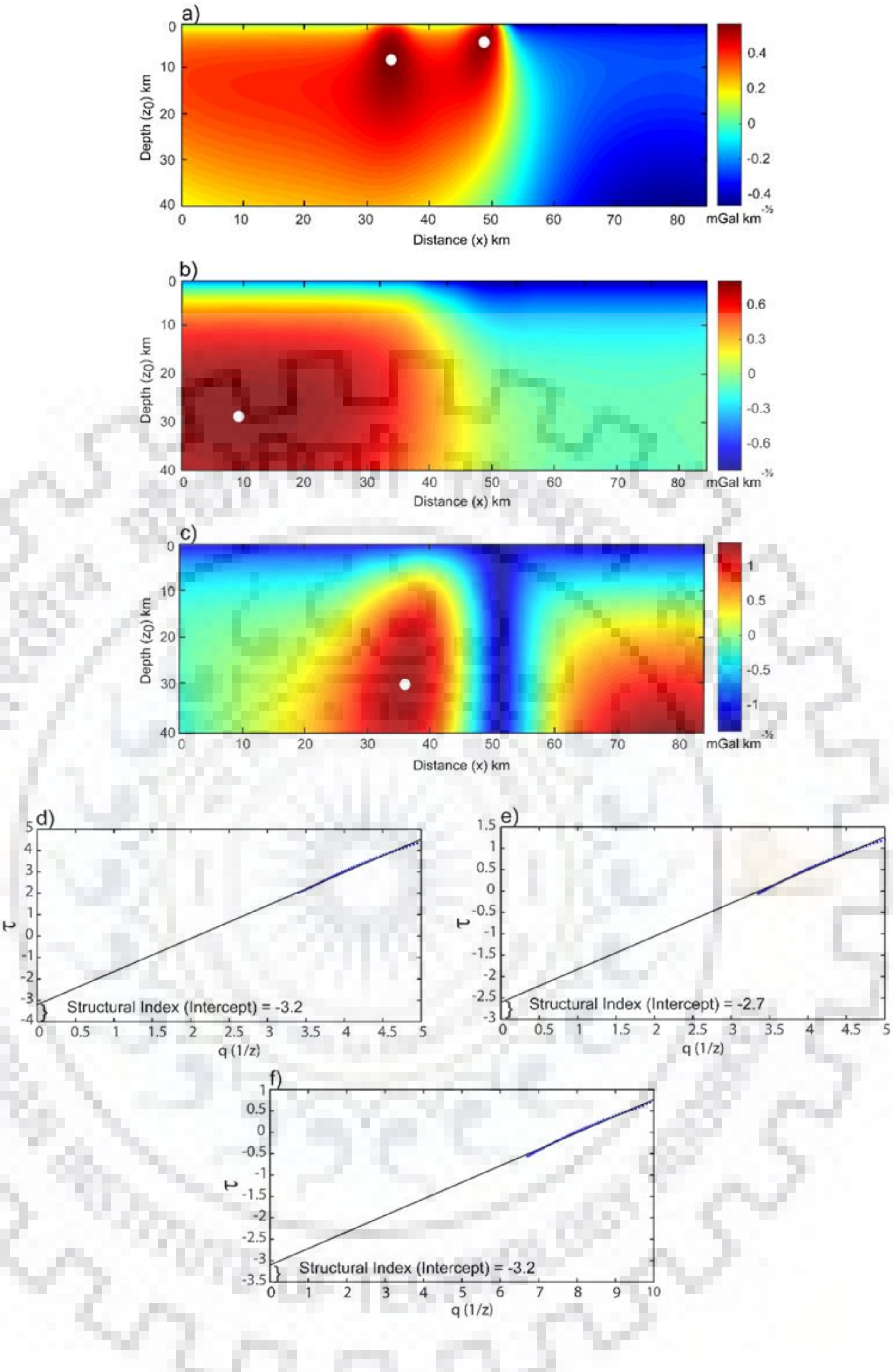

Figure 5.9: The plots of (a), (b) and (c) shows DEXP analysis of three subregions (I, II, III). The white marks represent extreme points of the DEXP transformed field. The plots of (d), (e) and (f) shows the variation of scaling function versus q(1/z) with structural index (intercept) 3.2, 2.7 and 3.2, which shows the sources as an infinite horizontal cylinder.

5.5 CRUSTAL MODELING (AA' and BB' profile)

The Bouguer gravity anomaly along two profiles AA' and BB' across DFB is modeled to understand the subsurface structure and their extension towards the north (Fig. 5.10). A three-layered crustal structure is considered based on the power spectrum analysis (Fig. 5.2). The depth of the Moho is based on the 3D structural inversion (Fig. 5.7). I estimated densities of different bodies based on conversions from seismic velocities and average rock density values. The details are presented in table 5.2. I have used the Nafe-Drake equation given by Brocher T.M. (2005), which were introduced graphically by Ludwig et al. (1970). This equation is useful for a wide variety of rock formations with P-wave velocities in between 1.5 and 8.5 km/sec and thus, suitable for the rock formations present in the DFB region having a P-wave velocity range from 4.6 to 8.4 km/sec (Tewari et al., 1997).

The results of different methods are used as constraints in the modeling step by step as discussed in section 5.2.2. I observe a significant amount of misfit between the gravity response of the upwarped Moho and the observed Bouguer gravity anomaly during modeling. This indicates the presence of a deeper high-density body, which is additionally modeled as mantle-derived underplated material (Fig. 5.10) and indicated in the previous seismic studies (Tewari et al., 1997; Fig. 5.10c). The underplated mafic layer with high density (~ 3100 kg/m^3) is the only possible source at such depth that can obscure the seismic wave propagation (Thybo and Nielsen, 2012) and can explain no seismic reflectivity observed at the Moho below DFB. The mafic body becomes narrower towards the north in AA' profile, which indicates the episode of underplating at the base of lower crust along the orogenic belt in geological past.

The geological models of the Aravalli-Delhi fold belt (ADFB) suggest different litho-tectonic units are juxtaposed along west dipping intracrustal faults along which lower crustal rocks exhumed to the shallower depth during BGC and DFB orogeny (Sharma, 2009). These thrusts/faults are also observed in the seismic profile (Tewari et al., 1997) and the same is incorporated in the forward modeling with the high density (2880- 2900 kg/m^3) lower crust in our model. The basement layer shows the high density (ρ = 2720 -2750 kg/m^3) rocks with the presence of faults across the basement. The gravity anomaly is modeled by exposed rock body (ρ = 2670 kg/m^3) in the SE side of the profile AA' (Fig. 5.10a). The top alluvial sedimentary layer (ρ = 2500 kg/m^3) is observed along the AA' profile (Fig. 5.1) and incorporated in the gravity model. In general, the basement and surface rocks of different formations represent high gravity anomaly except for MIS and exposed DFB rocks towards the west of Hindoli group BB' (Fig. 5.10b). The low density (2700 kg/m^3) is assigned to the rocks of MIS due to the basic-felsic nature. Both models (AA' and BB') correlate with the prominent deep tectonic structure, which shows the continuity towards the north with reduced thickness.

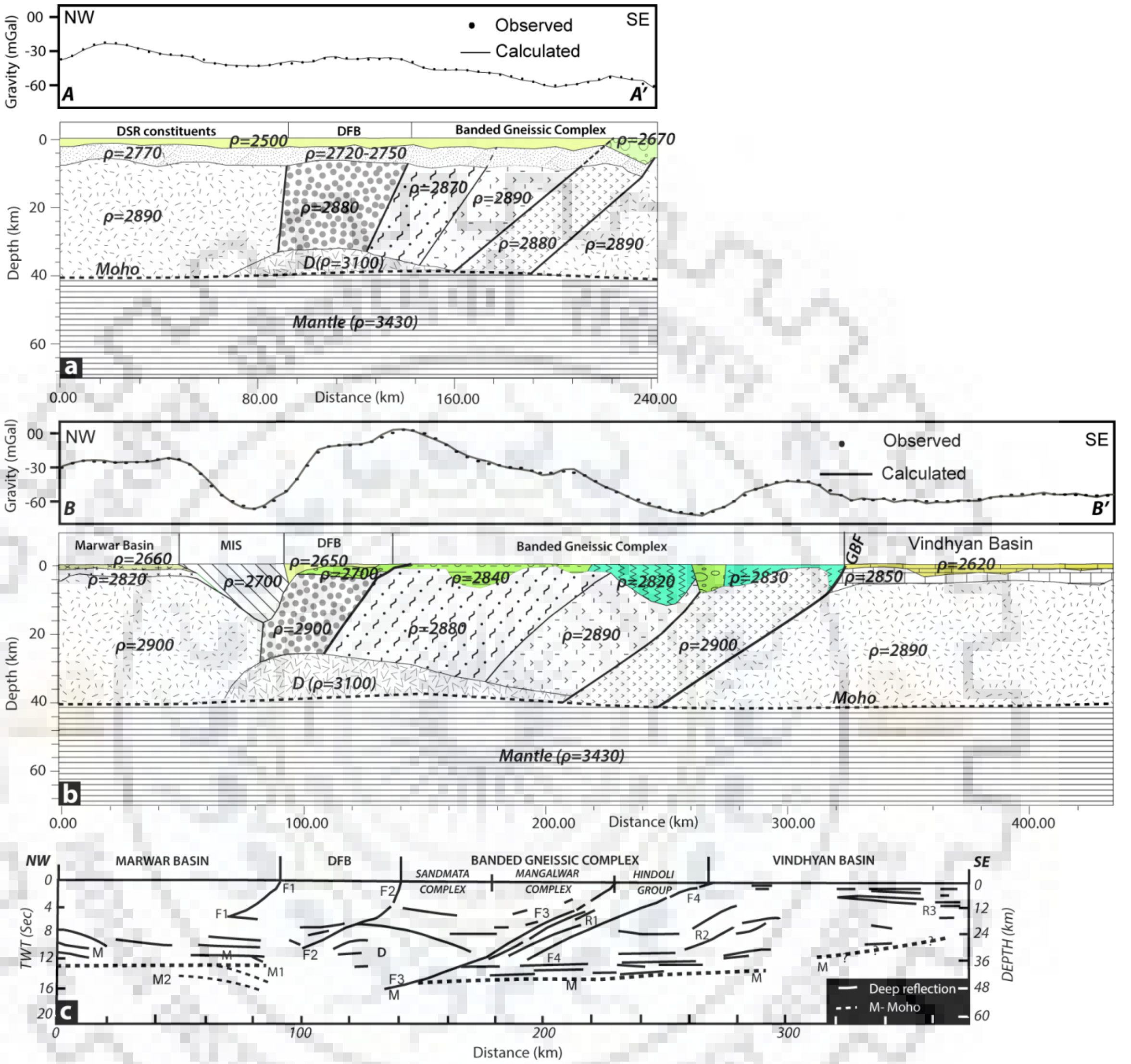

Figure 5.10: Gravity modeling across the Delhi fold belt incorporating constraints derived from power spectrum analysis, filtering, 3D inversion, WSED method, DEXP method. The Moho shows upwarp below DFB and Sandmata complex with the existence of underplated material constrained by DSS seismic model. a) along the profile AA': The depth model is an extension of Proterozoic DFB and Archean BGC towards the north with the underplated material at the Moho depth, b) along the profile BB'. The Great Boundary fault (GBF) divides the Vindhyan Basin in the east to the Hindoli Group of rocks in the west, c) The line drawing of the seismic section along the Nagaur- Jhalawar geotransect, which is located around 150 km towards south of our profile BB'. The section shows a thicker crust with a domal shaped body (D) in the lower crust and dipping reflections under the DFB and BGC. F1-F4 represents faults and R1, R2 and R3 are reflections (after Tewari et al., 1997).

5.6 RESULTS

The analysis of Bouguer gravity anomaly gives important constraints on the crustal structure of the DFB and its extensions. The LWFA indicate the signatures of deflection of the DFB towards NW-SE direction. The depth of the Moho derived from 3D structural inversion of gravity anomaly due to the Moho confirms the upwarping below DEB and Sandmata complex. The developed WSED method demarcates the geological formation boundaries. The application of the DEXP method highlights the distinct signature of a deep horizontal cylindrical source below the DFB and Sandmata complex. It also indicates two shallow horizontal cylindrical sources as the DSR constituents. The gravity modeling suggests the presence of a high-density domal underplated material below the DFB and Sandmata. This high-density material is likely related to the residual underplated mafic plume head, which is associated with some episode of the ADFB orogeny. These results are discussed in light of previous studies in chapter 6.

Table 5.2

The lithostratigraphic units with their characteristics rock type and density (kg/m^3) along the profiles

Lithostratigraphic units with age (NW-SE) (Ramakrishnan and Vaidyanadhan, 2010)	**Rock type (Ramakrishnan and Vaidyanadhan, 2010)**	**Velocity (m/s) (Tewari et al., 1997)**	**A priori density values (kg/m^3) in inversion**	**Inverted Density values (kg/m^3)**
Indo-Gangetic plain (Quaternary: < *~2.5 Ma*)	Alluvium and wind-blown sand		2500	2500
Marwar basin (Neoproterozoic: *~550-500 Ma*)	Clay, Dolomite, Evaporites, limestone, Sandstone		2670*	2660
Crystalline basement			2820	2820
Malani Igneous Suite (Neoproterozoic: *~750-720 Ma*)	Granite, Rhyolite, Basalt, Gabbro		2700*	2700
Delhi fold belt (Mesoproterozoic: *~1600-900 Ma*)	Calc-schist, Marble, Granite, Gneiss, Marble, Quartzite		2710*	2700
Vindhyan basin (Mesoproterozoic: *~1600-650 Ma*)	Limestone, Shale, Sandstone,	4600-5600	2480-2640*** 2600 (assigned)	2620
Crystalline basement		6600	2850***	2850
Hindoli group (Paleoproterozoic: *~1850 Ma*)	Felsic and mafic volcanics		2830**	2830
Sandmata complex (Paleoproterozoic: *~1800-1700 Ma*)	Charnockite bodies, Granulites, Migmatitic gneiss		2850**	2840
Mangalwar complex (Neoarchean: *~2900-2600 Ma*)	Granitic intrusions, Gneiss, Meta-volcanics, Schist		2820**	2820
Domal shaped body		7300	3100***	3100
Lower crust			2900	2900
Upper Mantle		8400	3440***	3440

*The average density values assigned from Reddy and Ramakrishna (1988).

**The average density values of the rock types in formations from Ramakrishnan and Vaidyanadhan (2010).

***The average density values converted from seismic velocities using the following Nafe-Drake equation (Brocher T.M., 2005).

$$\rho = 1.6612\,V_p - 0.4721\,V_p^2 + 0.0671\,V_p^3 - 0.0043\,V_p^4 + 0.000106\,V_p^5$$

where ρ, V_p are density (g/cm^3) and primary wave velocity (km/sec).

CHAPTER 6: DISCUSSION AND CONCLUSION

6.1 DISCUSSION

The Mesoproterozoic DFB extends from Gujarat (Deri-Ambaji) in the south towards the Indo-Gangetic alluvium in the north (Fig. 1.1a). The potential field methods (Fig. 1.1b) in conjunction with other geological and geophysical datasets provide a valuable tool to look into such complex tectonic setup (Mishra et al., 2000; Berrocal et al., 2004; Chamoli et al., 2011; Tiwari et al., 2015). I have applied different methods to the Bouguer gravity anomaly for understanding the subsurface structures and their extension. The power spectrum analysis shows three interfaces with a mean depth of 35.3 km, 9.3 km and 2.9 km corresponding to the Moho, upper-lower crust boundary (Chakraborty and Agarwal 1992) and alluvial basement depth, respectively (Fig. 5.2). The spectral analysis provides estimates of average depth to the sources with uncertainty in the order of 10%, especially in the case of deep-seated sources (Mishra and Pedersen, 1982). The estimated depth of the Moho is in agreement with the depth estimates derived for Nagaur-Jhalawar profile in the south using power spectrum analysis by Bansal and Dimri (1999). The mean alluvial basement depth occurs at 2.9 km, which is consistent with the depth estimates by ONGC in the Indo-Gangetic plain (Fig. 1.1; Sastri et al., 1971; Karunakaran and Ranga Rao, 1976).

The long-wavelength filtered anomaly shows a prominent SW-NE trending high gravity signature, which deflects towards the NW direction along the DSR axis (Fig. 5.3). The SW-NE trending high gravity anomaly is due to upwarping of the Moho below the DFB and the Sandmata complex. The depth of Moho using 3D gravity structural inversion varies from 39 km to 46 km (Fig. 5.7). The depth estimates are close to the inverted depth estimates using the receiver function studies at the stations NDA ~ 41 km, NPL ~ 41.5 km, DCE ~ 42 km, KUK ~ 44 km in NE and BRT~ 41 km in the south (Julia et al., 2009; Borah et al., 2015; Fig. 1.1b). Past seismological studies suggest the average depth of the Moho ~ 41 ± 2 km using modeling of multimode surface wave group velocity dispersion and their inversion (Mitra et al., 2011; Kumar et al., 2017) and ~ 46 km using receiver function analysis (Caldwell et al., 2013) below Indo- Gangetic plain. Mandal et al. (2013) reprocessed the DSS profile dataset and reported the variation of the crustal thickness between 38 and 50 km across the Proterozoic ADFB using common reflection surface stack method (CRS). Although his results show clear reflection at the Moho below Marwar basin and Sandmata complex, but no reflectivity is observed below the DFB probably due to low foldage and S/N ratio or the complex geological settings at the lower crust and Mantle boundary. It could also be due to the homogenization of the lower crust due to the igneous intrusion, which resulted in less acoustic impedance contrast at the Moho.

The DEXP method estimates the structural geometry and density contrast between source and surroundings. The DEXP transformed field of the subregion (I) across the DSR axis (Fig. 5.9a) show the presence of two structures (mean depths 8 and 4 km, infinite horizontal cylinder type) with positive density contrast, which infers as the Delhi-Sargodha ridge constituents. The DEXP transformed field of the subregions (II, III) across the DFB and Sandmata complex (Fig. 5.9b, c) confirms presence of a domal structure (mean depth ~ 30 km) having positive density contrast (dark red color) and further modeled as underplated plume material below the DFB and Sandmata complex (Fig. 5.10b). The depth and shape of the source are similar to the domal structure below the DFB and Sandmata complex observed in the DSS sections (Tewari et al., 1997).

The results of the 3D gravity structural inversion indicate a prominent upwarp (~ 2 km) at the Moho below the DFB and the Sandmata complex (Fig. 5.7, 5.10a, b), which is likely due to the past magmatic and underplating episodes. There is a lateral deflection in this upwarping pattern towards the Delhi-Sargodha ridge axis in NW-SE direction (Fig. 5.7). The gravity modeling along the two profiles (AA' and BB') suggests a high-density domal structure, which is likely derived from mantle during the Proterozoic age. The high amplitude of the gravity anomaly can only be modeled in the presence of high density underplated material, which is also observed in other tectonic settings such as tectonics of Mahanadi delta of eastern India (Behera et al., 2004), the Yellowstone-Snake river plain volcanic system (Denosaquo et al., 2009) and the Basque-Cantabrian Basin (Pedrera et al., 2017). A similar structure was also reported by DSS and gravity study in the south (Tewari et al., 1997; Mishra et al., 2000) and thus, indicate the continuation of this domal structure further north. This underplated material is modeled in the form of addition of mafic magma to the lower crust and uppermost mantle around the Moho rather than the older assumptions of ponding of magma just below the Moho (Thybo and Artemieva, 2013). The crustal model along profile AA' shows that different structures exposed in the southern region are covered below the sediments of the Indo-Gangetic plain in the north. It also shows that the prominent domal structure below the DFB in the south get depleted in the northern cross-section (AA'), which can be explained due to the large distance from the region of magmatic activity in the geological past. It is clear from the results of the Moho inversion (Fig. 5.7) that this domal structure deflects laterally towards NW direction. There is no significant signature of the presence of the DFB along the axis in further north towards the foothill of the Himalaya. The tectonic elements like MF and the GBF west of the DFB show clear glance in the contour of the basement, whereas the contours are smooth along the main axis of the DFB (Fig. 1.1). This supports no prominent basement structure towards the north of the DFB below the Indo-Gangetic plain. The region is seismically active zone with shallow small magnitude earthquakes in recent years (inset of Fig. 1.1; Das et al., 2018). The seismic events in the region are mostly distributed near the DFB and clustered at the intersection of the MDSSF and DSR. Some researchers proposed that the Delhi-Haridwar ridge (an extension of the DFB) act as a barrier and explain the low magnitude of the earthquakes surrounding the Delhi region (Arora et al., 2012). In general, I have not observed any prominent extension of the domal structure at Moho towards north beneath the Indo-Gangetic plain based on the gravity data, seismicity distribution and depth contours of the basement (Fig.1).

Based on the above observations, I conjecture that the NE trending DFB got deflected westward after NW corner indentation and anti-clockwise rotation of Indian plate post-Eocene collision (Voo et al., 1999). With continued convergence, the DFB structural element exhumed progressively to a shallower level through flexure buckling of Indian plate in the form of Delhi-Sargodha Ridge (DSR; Fig. 5.9), without producing any marked disruptive transverse signature (Fig. 5.4). This also explains the absence of any transverse ridge-like structure, north of DFB, beneath the Indo-Gangetic alluvium unlike other tectonic elements in the leading edge of central Indian peninsula to the east of DFB (Fig. 1.1). The clustering of shallow micro seismicity at the leading edge of DFB and DSR probably represent the edge effect of two orthogonal transverse structural elements. Further, if the above assertion is true then the theories related to the extension of DFB underneath Himalaya (Delhi-Haridwar ridge and MDSSF) and their related seismo-tectonic implications as a structural barrier (Arora et al., 2012) does not hold. The recent paleoseismic studies in the Himalayan front (Kumar et al., 2006) mapped co-seismic surface rupture on either side of the supposed DFB trend in Himalaya, which also support the absence of any transverse structural barrier.

6.2 CONCLUSION

The spectral and multiscaling behavior of the Bouguer gravity anomaly of the DFB region is examined to derive the source geometry, boundaries and depth information. The power spectrum analysis gives three interfaces with a mean depth of 35.3 km, 9.3 km and 2.9 km corresponding to the Moho, upper-lower crust boundary and alluvial basement depth respectively. The filtered Bouguer gravity anomalies indicate the prominent signatures of the DFB extension towards the north. I propose a new wavelet source edge detector (WSED) method, which shows promising results to identify the complete source boundaries in the form of the “edge plot”. The method uses the wavelet theory to identify the directional properties of the edges. The method is found valuable when compared with conventional techniques. The application of the DEXP method highlights the distinct signature of a deep horizontal cylindrical source at a mean depth of 30 km below the DFB and Sandmata complex. It also indicates two shallow horizontal cylindrical sources as the DSR constituents at the depths of 8 and 4 km respectively in the north side of the region.

The trends of filtered gravity anomalies and the depth variations of the Moho from 3D inversion indicate deflection of the Moho towards NW direction along the DSR axis. The depth of Moho using 3D gravity structural inversion varies from 39 km to 46 km in the region. The geometry of the Moho confirms the upwarping (~ 2 km) and presence of a high density domal underplated material below the DFB and Sandmata complex. The deflection of the domal structure indicates the absence of a northward extension of the DFB underneath the Indo-Gangetic alluvium. A detail 2D crustal density model is proposed along two profiles AA' and BB' (Fig. 5.10) using the constraints from the results of different techniques applied on the Bouguer gravity anomaly.

The model reveals that the mantle-derived underplated plume material got deflected westward sometime after indentation of the NW corner of the Indian plate and its counter-clockwise rotation after Eocene collision. With continued convergence, this Himalaya parallel DFB element got involved in crustal flexure producing the DSR. This assertion has far-reaching seismotectonic implication.

6.3 FUTURE WORK

Some of the future scope of the thesis are:

a) The developed WSED method gives the position of source boundaries at present. The depth determination of edge boundaries of the sources using wavelet approach can further be attempted.

b) 3D gravity modeling can be carried out in the future. It is noteworthy that there is a need of high-resolution geophysical datasets in the study region for detail investigations.

APPENDIX A

MULTIRESOLUTION ANALYSIS USING DWT

The DWT uses multiresolution analysis to represent a signal in terms of its spatial frequency components (Mallat, 1989). It represents a signal using approximation $(\mathbf{V}_j)$ and detail $(\mathbf{W}_j)$ spaces with different level of resolution.

A sequence $\{V_j\}_{j\in\mathbf{Z}}$ of the closed subspaces of Hilbert space $\mathbf{L}^2(\mathbf{R})$ is a multiresolution approximation if the following properties exist (Mallat, 1989):

1. $\forall (j,n)\in\mathbf{Z}^2 \quad f(t)\in V_j \leftrightarrow f(t-2^j n)\in V_j$
2. $\forall j\in\mathbf{Z} \quad f(t)\in V_j \leftrightarrow f(t/2)\in V_{j+1}$
3. $\forall j\in\mathbf{Z} \quad V_{j+1}\in V_j$
4. $\lim_{j\to+\infty} V_j = \bigcap_{j\in z} V_j = \{0\}$
5. $\lim_{j\to-\infty} V_j = \bigcup_{j\in z} V_j = \mathbf{L}^2(\mathbf{R})$
6. There exist $\phi(t)\in V_0$ such that $\phi(t-n)_{n\in z}$ is an orthonormal basis of V_0

For each integer j, the functions are an orthonormal basis for each V_j. The wavelet spaces W_j are introduced from the orthogonal complements of V_j in V_{j-1} $(V_{j-1} = V_j \oplus W_j, \forall j\in\mathbf{Z})$. One can construct wavelet ψ such that the dilated and translated family is an orthogonal basis of $\mathbf{L}^2(\mathbf{R})$.

In 2D wavelet transform, the scaling and wavelet function are two variable functions, denoted as $\phi(x,y)$ and $\psi(x,y)$.

The scaled and wavelet basis functions expressions are given as (Mallat, 1989):

$$\phi_{j_0,m,n}(x,y) = 2^{j/2}\phi\left(2^j x - m, 2^j y - n\right) \tag{A-1}$$

$$\psi^i_{j,m,n}(x,y) = 2^{j/2}\psi^i\left(2^j x - m, 2^j y - n\right) \qquad i=\{H,V,D\} \tag{A-2}$$

Where $(x,y)\in\mathbf{R}^2$ and $(m,n)\in\mathbf{Z}^2$

There are one scaling function and three wavelet functions for each level. If the wavelet function is separable, then, these functions can be rewritten as:

$$\phi(x,y) = \phi(x)\ \phi(y) \tag{A-3}$$

$$\psi^H(x,y) = \psi(x)\ \phi(y) \tag{A-4}$$

$$\psi^V(x,y) = \phi(x)\ \psi(y) \tag{A-5}$$

$$\psi^D(x,y) = \psi(x)\ \psi(y) \tag{A-6}$$

The wavelet family $\{\psi^H_{j,m,n}, \psi^V_{j,m,n}, \psi^D_{j,m,n}\}_{m,n\in\mathbf{Z}^2}$ is an orthonormal basis of $\mathbf{W}_j^2$ and $\{\psi^H_{j,m,n}, \psi^V_{j,m,n}, \psi^D_{j,m,n}\}_{(j,m,n)\in\mathbf{Z}^3}$ is an orthonormal basis of $\mathbf{L}^2(\mathbf{R}^2)$.

The wavelet approximation coefficients for function f(x, y) of size $M \times L$ can be given as (Mallat, 1989):

$$W_\phi(j_0,m,n) = \frac{1}{\sqrt{ML}}\sum_{x=0}^{M-1}\sum_{y=0}^{L-1} f(x,y)\phi_{j_0,m,n}(x,y) \tag{A-7}$$

where j_0 is the scale of the coefficients and (m, n) are the parameters about the position.

The horizontal (W_ψ^H), vertical (W_ψ^V) and diagonal (W_ψ^D) wavelet detail coefficients can be written as (Mallat, 1989):

$$W_\psi^H(j,m,n) = \frac{1}{\sqrt{ML}}\sum_{x=0}^{M-1}\sum_{y=0}^{L-1} f(x,y)\psi^H_{j,m,n}(x,y) \qquad j \geq j_0 \tag{A-8}$$

$$W_\psi^V(j,m,n) = \frac{1}{\sqrt{ML}}\sum_{x=0}^{M-1}\sum_{y=0}^{L-1} f(x,y)\psi^V_{j,m,n}(x,y) \qquad j \geq j_0 \tag{A-9}$$

$$W_\psi^D(j,m,n) = \frac{1}{\sqrt{ML}}\sum_{x=0}^{M-1}\sum_{y=0}^{L-1} f(x,y)\psi^D_{j,m,n}(x,y) \qquad j \geq j_0 \tag{A-10}$$

This is the general form of the 2D discrete wavelet transform. If the scaling and wavelet functions are separable, the summation can be decomposed into two stages. The calculation is first done for the x-axis and followed by the y-axis.

BIBLIOGRAPHY

[1]. Arısoy M.O. and Dikmen U. 2015. Edge enhancement of magnetic data using fractional-order-derivative filters. Geophysics, 80(1), J7-J17.

[2]. Arora B.R. and Mahashabde M.V. 1987. A transverse conductive structure in the northwest Himalaya. Physics of the Earth Planetary Interiors, 45(2), 119–127.

[3]. Arora B.R., Gahalaut V.K. and Kumar N. 2012. Structural control on along- strike variation in the seismicity of the northwest Himalaya. Journal of Asian Earth Sciences, 57, 15-24.

[4]. Arora B.R., Lilley F.E.M., Sloane M.N., Singh B.P., Srivastava B.J. and Prasad S.N. 1982. Geomagnetic induction and conductive structures in northwest India. Geophysical Journal of Royal Astronomical Society, 69, 459–475.

[5]. Bansal A.R. and Dimri V.P. 1999. Gravity evidence for mid crustal domal structure below Delhi fold belt and Bhilwara super group of western India. Geophysical Research Letter, 26(18), 2793-2795.

[6]. Barbosa V.C.F., Silvat J.B.C and Medeiros W.E. 1999. Gravity inversion of a discontinuous relief stabilized by weighted smoothness constraints on depth. Geophysics, 64(5), 1429-1437.

[7]. Behera L., Sain K., and Reddy P. 2004. Evidence of underplating from seismic and gravity studies in the Mahanadi delta of eastern India and its tectonic significance. Journal of Geophysical Research, 109, B12311.

[8]. Berrocal J., Marangoni Y., de Sa N.C., Fuck R., Soares Jose E.P., Dantas E., Perosi F. and Fernandes C. 2004. Deep seismic refraction and gravity crustal model and tectonic deformation in Tocantins Province, Central Brazil. Tectonophysics, 388(1-4), 187-199.

[9]. Bhaskara Rao D. and Rameshbabu N. 1991. A rapid method for three-dimensional modeling of magnetic anomalies. Geophysics 56 (11), 1729–1737.

[10]. Bhattacharjee J., Golani P.R. and Reddy A.B. 1988. Rift related bimodal volcanism and metallogeny in the Delhi fold belt, Rajasthan and Gujarat. Indian Journal of Geology, 60, 191-199.

[11]. Bhattacharyya B.K. 1966. Continuous spectrum of the total magnetic- field anomaly due to a rectangular prismatic body. Geophysics, 31(1), 97–121.

[12]. Blakely R.J. 1995. Potential theory in gravity and magnetic applications. Cambridge University Press, New York.

[13]. Borah K., Kanna N., Rai S.S. and Prakasam K. S. 2015. Sediment thickness beneath the Indo-Gangetic plain and Siwalik Himalaya inferred from receiver function modeling. Journal of Asian Earth Sciences, 99, 41-56.

[14]. Brocher T.M. 2005. Empirical relations between elastic wave speeds and density in the Earth's crust. Bulletin of the Seismological Society of America, 95(6), 2081-2092.

[15]. Butler P.G., Jr. Wanamaker A.D., Scourse J.D., Richardson C.A. and Reynolds D.J. 2013. Variability of marine climate on the north Icelandic Shelf in a 1357-year proxy archive based on growth increments in the bivalve Arctica islandica. Paleography, Palaeoclimatology, Palaeoecology, 373, 141-151.

[16]. Caldwell W.B., Klemperer S.L., Lawrence J.F., Rai S.S. and Ashish 2013. Characterizing the main Himalayan thrust in the Garhwal Himalaya, India with receiver function CCP stacking. Earth and Planetary Science Letter, 367, 15–27.

[17]. Chakraborty K. and Agarwal N.P. 1992. Mapping of the crustal discontinuities by wavelength filtering of the gravity field. Geophysical Prospecting, 40(7), 801-822.

[18]. Chamoli A., Pandey A.K., Dimri V.P. and Banerjee P. 2011. Crustal configuration of the northwest Himalaya based on modeling of gravity data. Pure and Applied Geophysics, 168(5), 827-844.

[19]. Chamoli A., Swaroopa Rani V., Srivastava K., Srinagesh D. and Dimri V.P. 2010. Wavelet analysis of the seismograms for Tsunami warning. Nonlinear Processes in Geophysics, 17, 569-574.

[20]. Cooper G.R.J. 2009. Balancing images of potential-field data. Geophysics, 74(3), L17–L20.

[21]. Cordell L. and Grauch V.J.S. 1985. Mapping basement magnetization zones from aeromagnetic data in the San Juan Basin, New Mexico. In: The Utility of Regional Gravity and Magnetic Anomaly Maps (ed. W.J. Hinze), pp.181-197. Society of Exploration Geophysicists.

[22]. Cordell L. and Henderson R.G. 1968. Iterative three-dimensional solution of gravity anomaly data using a digital computer. Geophysics 38 (4), 596–601.

[23]. Das R., Mukhopadhyay S., Singh R.K. and Baidya P.R. 2018. Lapse time and frequency-dependent coda wave attenuation for Delhi and its surrounding regions. Tectonophysics, 738–739, 51–63.

[24]. Daubechies I 1992. Ten Lectures on Wavelets. SIAM, Philadelphia.

[25]. Denosaquo K., Smith R.B. and Lowry A.R. 2009. Density and lithospheric strength models of the Yellowstone-Snake river plain volcanic system from gravity and heat flow data. Journal of Volcanology and Geothermal Research, 188, 108-127.

[26]. Dimri V.P. 1992. Deconvolution and inverse theory. Elsevier Science Publishers, Amsterdam.

[27]. Dubey C.P. and Tiwari V.M. 2016. Computation of the gravity field and its gradient: Some applications. Computer and Geosciences, 88, 83-96.

[28]. Dyrelius D. and Vogel A. 1972. Improvement of convergency in iterative gravity interpretation. Geophysical Journal of the Royal Astronomical Society, 27, 195–205.

[29]. Evjen H.M. 1936. The place of the vertical gradient in gravitational interpretations. Geophysics, 1, 127-136.

[30]. Fairhead J.D., Salem A., Cascone L., Hammill M., Masterton S. and Samson E. 2011. New developments of the magnetic tilt-depth method to improve structural mapping of sedimentary basins. Geophysical Prospecting, 59, 1072-1086.

[31]. Fedi M. 2007. DEXP: A fast method to determine the depth and the structural index of potential field sources. Geophysics, 72(1), 1-11.

[32]. Fedi M. and Florio G. 2001. Detection of potential fields sources boundaries by enhanced horizontal derivative method. Geophysical Prospecting, 49, 40–58.

[33]. Fedi M. and Quarta T. 1998. Wavelet analysis for the regional-residual and local separation of potential field anomalies. Geophysical Prospecting, 46, 507-525.

[34]. Fedi M. and Rapolla A. 1999. 3-D inversion of gravity and magnetic data with depth resolution. Geophysics, 64(2), 452-460.

[35]. Fedi M., Florio G. and Quarta T. 2009. Multiridge analysis of potential fields: Geometrical method and reduced Euler deconvolution. Geophysics 74, L53–L65.

[36]. Ferreira Francisco J.F., Souza J., Bongiolo Alessandra de B. e S. and Luís G. de Castro 2013. Enhancement of the total horizontal gradient of magnetic anomalies using the tilt angle. Geophysics, 78(3), J33-J41.

[37]. Florio G. and Fedi M. 2014. Multiridge Euler deconvolution. Geophysical Prospecting, 62(2), 333-351.

[38]. Gerovska D., Araúzo-Bravo M., Whaler K., Stavrev P. and Reid A. 2010. Three-dimensional interpretation of magnetic and gravity anomalies using the finite-difference similarity transform. Geophysics, 75(4), L79–L90.

[39]. Gilgen H. 2006. Univariate Time Series in Geosciences: Theory and Examples. Springer, Berlin.

[40]. Godin L. and Harris L.B. 2014. Tracking basement cross-strike discontinuities in the Indian crust beneath the Himalayan orogeny using gravity data-relationship to upper crustal faults. Geophysics Journal International, 198(1), 198-215.

[41]. Goyal P. and Tiwari V.M. 2013. Application of the continuous wavelet transform of gravity and magnetic data to estimate sub-basalt sediment thickness. Geophysical Prospecting, 1-10.

[42]. GSI 2000. Seismotectonic Atlas of India and its environs. Publisher: Geological Survey of India, Calcutta.

[43]. GSI-NGRI 2006. Gravity map series of India. Geological Society of India and National Geophysical Research Institute, Hyderabad, India.

[44]. Hidalgo-Gato M.C. and Barbosa V.C.F. 2015. Edge detection of potential-field sources using scale-space monogenic signal: Fundamental principles. Geophysics, 80(5), J27-J36.

[45]. Hsu S., Sibuet J.C. and Shyu C. 1996. High-resolution detection of geologic boundaries from potential field anomalies: an enhanced analytic signal technique. Geophysics, 61(2), 373-386.

[46]. International Seismological Centre, On-line Bulletin, http://www.isc.ac.uk, International Seismological Centre, Thatcham, United Kingdom, 2016.

[47]. Julia J., Jagadeesh S., Rai S.S. and Owens T. 2009. Deep crustal structure of the Indian shield from joint inversion of P wave receiver functions and Rayleigh wave Group velocities: Implications for Precambrian crustal evolution. Journal of Geophysical Research, 114, B10313.

[48]. Karunakaran C. and Ranga Rao A. 1976. Status of exploration for hydrocarbons in the Himalayan region – contribution to stratigraphy and structure. Geological Survey of India, 41, 1–66.

[49]. Krishna V.G. and Rao V. 2011. Velocity modeling of a complex deep crustal structure across the Mesoproterozoic south Delhi Fold Belt, NW India, from the joint interpretation of coincident seismic wide-angle and near-offset reflection data: An approach using unusual reflections in wide-angle records. Journal of Geophysical Research, 116, B01307.

[50]. Kumar A., Kumar N., Mukhopadhyay S. and Baidya P. 2017. Crustal and uppermost mantle structures in the frontal Himalaya and Indo-Gangetic basin using surface wave: tectonic implications. Quaternary International, 462, 34–49.

[51]. Kumar M.R., Mishra D.C. and Singh B. 2013. Lithosphere, crust and basement ridges across Ganga and Indus basins and seismicity along the Himalayan front, India and Western Fold Belt, Pakistan. Journal of Asian Earth Sciences, 75, 126-140.

[52]. Kumar S., Wesnousky S.G., Rockwell T.K., Briggs R.W., Thakur V.C. and Jayangondaperumal R. 2006. Paleoseismic evidence of great surface rupture earthquakes along the Indian Himalaya. Journal of Geophysical Research, 111, B03304.

[53]. Leblanc G.E. and Morris W.A. 2001. Denoising of aeromagnetic data via the wavelet transform. Geophysics, 66(6), 1793-1804.

[54]. Li X. 2016. Terracing gravity and magnetic data using edge-preserving smoothing filters. Geophysics, 81 (2), G41-G47.

[55]. Ludwig W.J., Nafe J.E. and Drake C. L. 1970. Seismic refraction, in The Sea, 4, edited by A. E. Maxwell, 53 – 84, Wiley-Interscience, New York.

[56]. Malamud B.D. and Turcotte D.L. 2001. Wavelet analyses of Mars polar topography. Journal of Geophysical Research, 106, 17497-17504.

[57]. Mallat S. 1999. A Wavelet Tour of Signal Processing, Academic Press.

[58]. Mandal B., Sen M.K., Vaidya V.R. and Mann J. 2013. Deep seismic image enhancement with the common reflection surface (CRS) stack method: evidence from the Aravalli–Delhi fold belt of northwestern India. Geophysical Journal International, 196(2), 902-917.

[59]. Martelet G., Sailhac P., Moreau F. and Diament M. 2001. Characterization of geological boundaries using 1-D wavelet transform on gravity data: Theory and application to the Himalayas. Geophysics, 66(4), 1116-1129.

[60]. Miller H. G. and Singh V. 1994. Potential field tilt — A new concept for the location of potential field sources. Journal of Applied Geophysics, 32, 213–217.

[61]. Mishra D.C. and Pedersen L.B. 1982. Statistical analysis of potential fields from sub-surface relief. Geoexploration, 19(4), 247-265.

[62]. Mishra D.C., Singh B., Tiwari V.M., Gupta S.B. and Rao M.B.S.V. 2000. Two cases of continental collisions and related tectonics during the Proterozoic period in India insights from gravity modeling constrained by seismic and magnetotelluric studies. Precambrian Research, 99(3-4), 149–169.

[63]. Mitra S., Kainkaryam S.M., Padhi A., Rai S.N. and Bhattacharya S.N. 2011. The Himalayan foreland basin crust and upper mantle. Physics of the Earth and Planetary Interiors, 184(1-2), 34–40.

[64]. Molnar P., Fitch T.J. and Francis T.Wu. 1973. Fault plain solutions of shallow earthquakes and contemporary tectonics in Asia. Earth and Planetary Science Letters, 19(2), 101-112.

[65]. Moreau F. and Gilbert D. 1999. Identification of sources of potential fields with the continuous wavelet transform: Basic theory. Journal of Geophysical Research, 104(B3), 5003-5013.

[66]. Moreau F., Gilbert D., Holschnaider M. and Saracco G. 1997. Wavelet analysis of potential fields: Inverse Problems, 13(1), 165–178.

[67]. Nabighian M.N. 1972. The analytic signal of two-dimensional magnetic bodies with polygonal cross-section: Its properties and use for automated anomaly interpretation. Geophysics, 37, 507- 517.

[68]. Oldenburg D.W. 1974. The inversion and interpretation of gravity anomalies. Geophysics 39 (4), 526–536.

[69]. Parker R. 1973. The rapid calculation of potential anomalies. Geophysical Journal of the Royal Astronomical Society, 31(4), 447–455.

[70]. Pedrera A., García-Senz J., Ayala C., Ruiz-Constán A., Rodríguez-Fernández L.R., Robador A. and González Menéndez L. 2017. Reconstruction of the exhumed mantle across the North Iberian Margin by crustal-scale 3-D gravity inversion and geological cross section. Tectonics, 36(12), 3155–3177.

[71]. Prasad B.R., Tewari H.C., Vijaya Rao V., Dixit M.M. and Reddy P.R. 1998. Structure and tectonics of the Proterozoic Aravali-Delhi Fold Belt in northwestern India from deep seismic reflection studies. Tectonophysics, 288, 31-41.

[72]. Rai S.S., Priestley K., Gaur V.K., Mitra S., Singh M.P. and Searle M.P. 2006. Configuration of the Indian Moho beneath the NW Himalaya and Ladakh. Geophysical Research Letters, 33, L15308.

[73]. Ramakrishnan M. and Vaidyanadhan R. 2010. Geology of India, volume 1. Geological Society of India, Bangalore.

[74]. Rao V., Prasad B.R., Reddy P.R. and Tewari H.C. 2000. Evolution of Proterozoic Aravalli Delhi Fold Belt in the northwestern Indian shield from seismic studies, Tectonophysics, 327, 109–130.

[75]. Reddy A.G.B. and Ramakrishna T.S. 1988. Subsurface structure of the shield area of Rajasthan-Gujarat area as inferred from gravity. In: Roy A.B. (Ed.) Precambrian of the Aravalli Mountain, Rajasthan, India. Geological Society of India, Memoir 7, 279-284.

[76]. Reid A. B., Allsop J. M., Granser H., Millett A. J. and Somerton I. W. 1990. Magnetic interpretation in three dimensions using Euler deconvolution. Geophysics 55, 80-91.

[77]. Ridsdill-Smith T.A. and Dentith M.C. 1999. The wavelet transform in aeromagnetic processing. Geophysics, 64(4), 1003-1013.

[78]. Roest W.R., Verhoef J. and Pilkington M. 1992. Magnetic interpretation using the 3-D analytic signal. Geophysics, 57(1), 116-125.

[79]. Roy A.B. 1988. Stratigraphic and tectonic framework of the Aravalli mountain range. Memoir Geological Society of India, 7, 3–31.

[80]. Roy A.B. and Jakhar S.R. 2002. Geology of Rajasthan, Northwest India: Precambrian to Recent. Scientific Publishers (India), Jodhpur.

[81]. Salem A., Green C., Campbell S., Fairhead J.D., Cascone L. and Moorhead L. 2013. Moho depth and sediment thickness estimation beneath the Red Sea derived from satellite and terrestrial gravity data. Geophysics, 78(5), G89-G101.

[82]. Salem A., Williams S., Fairhead D., Smith R. and Ravat D. 2008. Interpretation of magnetic data using tilt-angle derivatives. Geophysics, 73(1), L1–L10.

[83]. Santos D. F., Silva J. B. C., Barbosa V. C. F. and Braga L. F. S. 2012. Deep-pass - An aeromagnetic data filter to enhance deep features in marginal basins. Geophysics, 77(3), J15–J22.

[84]. Sastri V.V., Bhandari, L.L., Raju A.T.R. and Datta A.K. 1971. Tectonics framework and subsurface stratigraphy of the Ganga basin. Journal Geological Society of India, 12(3), 232–233.

[85]. Sharma R.S. 1988. Patterns of metamorphism in the Precambrian rocks of the Aravalli Mountain belt. In: Roy A.B. (Ed.), Precambrian of the Aravalli Mountain, Rajasthan, India. Geological Society of India, Memoir 7, 95-108.

[86]. Sharma R.S. 1995. An evolutionary model for the Precambrian crust of Rajasthan: some petrological and geochronological considerations. Memoir Geological Society of India, 31, 91–115.

[87]. Sharma R.S. 2009.Cratons and Fold Belts of India, Lecture Notes in Earth Sciences. Springer, Berlin.

[88]. Shukla A.K., Prakash R., Singh R.K., Mishra P.S. and Bhatnagar A.K. 2007. Seismotectonic implications of Delhi region through fault plane solutions of some recent earthquakes. Current Science, 93(12), 1848-1853.

[89]. Sinha-Roy S. 1984. Precambrian crustal interactions in Rajasthan, NW India. Indian Journal of Earth Sciences, CEISM Volume, 84–91.

[90]. Sinha-Roy S. 1988. Proterozoic Wilson cycle in Rajasthan. Memoir Geological Society of India, 7, 95-108.

[91]. Sinha-Roy S., Malhotra G. and Guha D.B. 1995. A transect across Rajasthan Precambrian terrain in relation to geology, tectonics and crustal evolution in south-central Rajasthan. Memoir Geological Society of India, 31, 63-89.

[92]. Sinha-Roy S., Malhotra G. and Guha D.B. 1998. Geology of Rajasthan. Geological Society of India, Bangalore.

[93]. Spector A. and Grant F.S, 1970. Statistical models for interpreting aeromagnetic data. Geophysics, 35(2), 293–302.

[94]. Srivastava S. and Agarwal B.N.P. 2010. Inversion of the amplitude of the two-dimensional analytic signal of the magnetic anomaly by the particle swarm optimization technique. Geophysical Journal International, 182, 652-662.

[95]. Srivastava S., Datta D., Agarwal B.N.P. and Mehta S. 2014. Applications of Ant Colony Optimization in the determination of source parameters from total gradient of potential fields. Near Surface Geophysics, 12(3), 373-389.

[96]. Sun Y., Yang W., Zeng X. and Zhang Z. 2016. Edge enhancement of potential field data using spectral moments. Geophysics, 81(1), G1-G11.

[97]. Sychanthavong S.P.H. and Desai S.D. 1977. Protoplate tectonics controlling the Precambrian deformations and metallogenic epochs of NW Peninsular India. Minerals Science and Engineering, 9, 218-236.

[98]. Telesca L., Chamoli A., Lovallo M. Stabile T.A. 2015. Investigating the tsunamigenic potential of earthquakes from analysis of the informational and multifractal properties of seismograms. Pure and Applied Geophysics, 172(7), 1933-1943.

[99]. Telesca L., Lapenna V. and Alexis N. 2004. Multiresolution wavelet analysis of earthquakes. Chaos, Solitons & Fractals, 23(2), 741-748.

[100]. Telesca L., Lovallo M., Chamoli A., Dimri V.P. and Srivastava K. 2013. Fisher–Shannon analysis of seismograms of tsunamigenic and non-tsunamigenic earthquakes. Physica A: Statistical Mechanics and its Applications, 392(16), 3424-3429.

[101]. Tewari H.C., Dixit M.M., Rao N.M., Venkateswarlu N. and Rao V. 1997a. Crustal thickening under the palaeo-meso-Proterozoic Delhi fold belt in northwestern India: evidence from deep reflection profiling. Geophysical Journal International, 129(3), 657-668.

[102]. Tewari H.C., Prasad B.R., Rao V., Reddy P.R., Dixit M.N. and Madhava Rao N. 1997b. Crustal reflectivity parameter for deciphering the evolution process across the

Proterozoic Aravalli-Delhi fold belt. Journal Geological Society of India, 50(6), 779-785.

[103]. Thomson D.T. 1982. EULDPTH: A new technique for making computer-assisted depth estimates from magnetic data. Geophysics, 47, 31–37.

[104]. Thybo H. and Artemieva I.M. 2013. Moho and magmatic underplating in continental lithosphere. Tectonophysics, 609, 605–619.

[105]. Thybo H. and Nielsen C.A. 2012. Seismic velocity structure of crustal intrusions in the Danish Basin. Tectonophysics, 572, 64-75.

[106]. Tiwari V.M., Mishra D.C. and Pandey A.K. 2015. The lithospheric density structure below the western Himalayan syntaxis: tectonic implications. Geological Society of London, Special Publications, 412, 55-65.

[107]. Valdiya K.S. 1976. Himalayan transverse faults and folds and their parallelism with the subsurface structures of the north Indian plains. Tectonophysics, 32, 353–386.

[108]. Verduzco B., Fairhead J.D., Green C.M. and Mackenzie C. 2004. New insights into magnetic derivatives for structural mapping. The Leading Edge, 23, 116–119.

[109]. Voo V.R., Spakman W. and Bijwaard H. 1999. Tethyan subducted slabs under India. Earth and Planetary Science Letters, 171(1), 7-20.

[110]. Walnut David F. 2002. An Introduction to Wavelet Analysis. Springer-Verlag New York, USA.

[111]. Wijns C., Perez C. and Kowalczyk P. 2005. Theta map: Edge detection in magnetic data. Geophysics, 70(4), L39–L43.

[112]. Williams S., Fairhead J.D. and Flanagan G. 2002. Realistic models of basement topography for depth to magnetic basement testing. 72nd SEG annual meeting, Salt Lake City, Utah, Expanded Abstracts, 814-817.

[113]. Yadav P.K., Adhikari P.K., Srivastava S., Maurya V.P., Tripathi A., Singh S., Singh R.K. and Bage A.K. 2018. Lithologic boundaries from gravity and magnetic anomalies over Proterozoic Dalma volcanic. Journal of Earth System Science, 127:17.

[114]. Yao. Y., Huang D., Yu X. and Chai B. 2016. Edge interpretation of potential field data with the normalized enhanced analytic signal. Acta Geodetica et Geophysica, 51, 125–136.

[115]. Zhang X., Yu P., Tang R., Xiang Y., Zhao C. 2014. Edge enhancement of potential field data using an enhanced tilt angle. Exploration Geophysics, 46, 276-283.